A Study on Three Dimensional Spatial Scattering Modulation Systems

Yan Jiang

Department of Electronic and Electrical Engineering
University of Sheffield

Supervisors: Prof. Jie Zhang, Prof. Timothy O'Farrell
This thesis is submitted for the approval of the
Doctor of Philosophy

January 2023

This dissertation is dedicated to my beloved parents. Without their unconditional love, encouragement and support, I would not be the person I am today.

Acknowledgements

I would like to express the deepest appreciation to my first supervisor, Prof. Jie Zhang, for his consistent guidances during my whole Ph.D. study. He can always provide insightful ideas for my research direction and valuable suggestions and comments for solving problems. He also inspired me to be an independent researcher, not only with hard working and good time management, but also with the positive attitude. I am also very grateful to my second supervisor, Prof. Timothy O'Farrell, for guiding me from the graduate level. He is a very talented researcher and is very kind to provide help on my research. His diligence and self-discipline made me always look up to him as my role model. A very special gratitude goes to Dr. Jiliang Zhang and Dr. Haonan Hu who have played a major part in transforming me from a beginner to an independent researcher. I could never accomplish my Ph.D studies without his guidance and persistent help.

I feel so fortunate to have the opportunity to work with them for four years, and without their guidance and persistent help, this dissertation would not have been possible.

Last but not the least, I want to thank my family and friends, who gave me many supports in the past four years. Specifically, I am very thankful to Mr. Jixuan Lin, Mr. Zeyang Li and Ms. Tian who gave me full support and went through thick and thin together with me throughout the Ph.D. study.

Abstract

With an explosive growth of data traffic demand, the researchers of the mobile communication era forecast that the traffic volume will have a 1000x increase in the forthcoming beyond fifth generation (B5G) network. To satisfy the growing traffic demand, the three-dimensional (3-D) multiple-input-and-multiple-output (MIMO) system is considered as a key technology to enhance spectrum efficiency (SE), which explores degrees of freedom in both the vertical and the horizontal dimensions. Combined with 3-D MIMO technology, index modulation (IM) is proposed to improve both energy efficiency (EE) and SE in the B5G era. Existing IM technologies can be categorized according to the domain in which the additional IM bits are modulated, e.g., the spatial-domain IM, the frequency-domain IM and the beamspace-domain IM etc.

As one of the mainstream IM techniques, spatial scattering modulation (SSM) is proposed, which works in the beamspace-domain. For SSM systems, the information bits are denoted by the distinguishable signal scattering paths and the modulated symbols. Therein, two information bit streams are transmitted simultaneously by selections of modulated symbols and scattering paths. However, the existing papers only discuss two-dimensional (2-D) SSM systems. The 2-D SSM system applies linear antenna arrays, which only take the azimuth angles to recognise the direction of scattering paths. Therefore, to take the full advantage of the beamspace-domain resources, this thesis mainly focuses on the 3-D SSM system design and the performance evaluation.

Firstly, a novel 3-D SSM system is designed. For the 3-D SSM system, besides the azimuth angles of arrival (AoA) and angles of departure (AoD), the elevation AoA and AoD are considered. Then the optimum detection algorithm is obtained, and the closed-form

union upper bound expression on average bit error probability (ABEP) is derived. Moreover, the system performance is evaluated under a typical indoor environment. Numerical results indicate that the novel 3-D SSM system outperforms the conventional 2-D SSM system, which reduces the ABEP by 10 times with the same signal-to-noise ratio (SNR) level under the typical indoor environment.

Secondly, for the system equipped with large-scale antenna arrays, hybrid beamforming schemes with several RF-chains have attracted more attention. To further explore the throughput of the 3-D SSM system, a generalised 3-D SSM system is proposed, which generates several RF-chains in a transmission time slot to convey modulated symbols. A system model of generalised 3-D SSM is proposed at first. Then an optimum detection algorithm is designed. Meanwhile, a closed-form expression of the ABEP is also derived and validated by Monte-Carlo simulation. For the performance evaluation, three stochastic propagation environments with randomly distributed scatterers are adopted. The results reveal that the generalised 3-D SSM system has better ABEP performance compared with the system with a single RF-chain. Considering different propagation environments, the SSM system has better ABEP performance under the statical propagation environments than the stochastic propagation environments.

Thirdly, to reduce the hardware and computational complexities, two optimisation schemes are proposed for the generalised 3-D SSM systems. The 2-D fast Fourier transform (FFT) based transceivers are designed to improve the hardware friendliness, which replace the analogue phase shift networks by the multi-bit phase shifter networks. To reduce the computational complexity of the optimum detection algorithm, a low-complexity detection scheme is designed based on the linear minimum mean square error (MMSE) algorithm. Meanwhile, to quickly evaluate, the asymptotic ABEP performance and the diversity gain of the generalised 3-D SSM system are obtained.

All the numerical results have been validated by Monte-Carlo simulation, and the conclusions revealed from the results can provide guidelines for future applications of the SSM modulation schemes.

List of Publications

[1]. **Y. Jiang**, H. Hu, S. Yang, J. Zhang and J. Zhang, "Generalized 3-D Spatial Scattering Modulation," in *IEEE Transactions on Wireless Communications*, Mar. 2022.

[2]. **Y. Jiang**, H. Hu, J. Zhang, Q. Chen and J. Zhang, "The Performance Analysis of the Mobile Edge Computing in Fog Radio Access Networks," in *IEEE Communications Letters*. (Submitted)

[3]. **Y. Jiang**, H. Hu, J. Zhang and J. Zhang, "On the Performance of Intelligent Reflecting Surface Aided Communication with Dynamic Blockages," in *IEEE Transactions on Vehicular Technology*. (Submitted)

[4]. H. Hu, **Y. Jiang**, J. Zhang, Q. Chen and J. Zhang, "On the Performance of Data Compression in Clustered Fog Radio Access Networks," in *IEEE Transactions on Communications*. (CA, Major Revision)

[5]. H. Hu, Y. Dong, **Y. Jiang**, Q. Chen and J. Zhang, "On the Age of Information and Energy Efficiency in Cellular IoT Networks with Data Compression," in *IEEE Internet of Things Journal*, Nov. 2022.

[6]. H. Hu, J. Zhang, **Y. Jiang**, Z. Li, Q. Chen and J. Zhang, "Computation Offloading Analysis in Clustered Fog Radio Access Networks with Repulsion," in *IEEE Transactions on Vehicular Technology*, Oct. 2021.

[7]. C. Chen, **Y. Jiang**, J. Zhang, X. Chu and J. Zhang, "Parameter Optimization for Energy Efficient Indoor Massive MIMO Small Cell Networks," in *Proc. IEEE 91st Vehicular Technology Conference (VTC2020-Spring)*, 2020.

[8]. **Y. Jiang**, J. Zhang and J. Zhang, "The 3-D Spatial Scattering Modulation with Planar Array," in *Proc. IEEE 3rd International Conference on Electronic Technology, Communication and Information (ICETCI)*, 2023. (Submitted)

Table of contents

List of figures

List of tables

Abbreviations

ABEP Average Bit Error Probability

AoA Angles of Arrival

AoD Angles of Departure

APEP Average Pairwise Error Probability

AR Augmented Reality

BEP Bit Error Probability

BER Bit Error Rate

B5G Beyond Fifth Generation

BS Base Station

CAGR Compound Annual Growth Rate

CCMC Continuous-input Continuous-output Memoryledd Channel

CIR Channel Impulse Response

CPEP Conditional Pairwise Error Probability

CSI Channel State Information

DCMC Discrete-input Continuous-output Memoryledd Channel

DM-OFDM Dual-mode Orthogonal Frequency Division Multiplexing

DM-SCIM Dual-mode Single-carrier Index Modulation

DoF Degree of Freedom

DSTSK Differentially Encoded Space-time Shift Keying

DSM Differential Spatial Modulation

D2D Device-to-Device

EB Exabytes

EMF Exhaustive-search based Matched Filter

FDE Frequency-domain Equalization

FFT Fast Fourier Transform

5G Fifth Generation

FTN Faster-than-Nyquist

ICI Inter-cell Interference

GBM Generalized Beamspace Modulation

GDM-OFDM Generalized Dual-mode Orthogonal Frequency Division Multiplexing

GMM-OFDM-IM Generalized Multiple-mode Orthogonal Frequency Division Multiplexing with Index Modulation

GSM Generalized Spatial Modulation

GSSK Generalized Space Shift Keying

GSTSK Generalized Space-time Shift Keying

IM Index Modulation

LoS Line-of-Sight

LSCE Least Square Channel Estimation

LTE Long Term Evolution

MF Matched Filter

MIMO Multiple-input-multiple-output

MISO Multiple-input-single-output

ML Maximum Likelihood

mm-wave Millimter Wave

MMSE Minimum Mean Square Error

MRC Maximal Ratio Combining

MRT Maximal Ratio Transmission

MU-MIMO Multiple-user Multiple-input-multiple-output

NMF Near-optmal Matched Filter

NLoS Non Line-of-Sight

OFDM-GIM Orthogonal Frequency Division Multiplexing with Generalized Index Modulation

OFDM-IM Orthogonal Frequency Division Multiplexing Index Modulation

OSDM Orthogonal Spatial-division Multiplexing

PDF Probability Density Function

PEP Pairwise Error Probability

PSK Phase Shift Key

QAM Quadrature Amplitude Modulation

QSM Quadrature Spatial Modulation

RF-chains Radio-frequency Chains

SCIM Single-carrier Index Modulation

SD Sphere Decoding

6G Sixth Generation

SINR Signal-to-interference-plus-noise Ratio

SLNR Signal-to-leakage-and-noise Ratio

SISO Single-input-single-output

SM Spatial Modulation

SSK Space Shift Keying

SSM Spatial Scattering Modulation

STBC-SM Space Time Block Coding-Spatial Modulation

STIM Space-time Index Modulation

STSK Space-time Shift Keying

3GPP Third Generation Partnership Project

2-D Two-dimensional

3-D Three-dimensional

UE User Equipments

UPA Uniform Planar Array

V-BLAST Vertical-Bell Lab Layered Space-Time

VR Virtual Reality

V2V Vehicle-to-Vehicle

ZTM-OFDM Zero-padded Tri-mode Index Modulation aided Orthogonal Frequency Division Multiplexing

Chapter 1

Introduction

1.1 Background

1.1.1 Requirements of Beyond 5G Communication Systems

As observed by Cisco [2], the total number of internet users will reach 5.3 billion by 2023 with a 6 percent compound annual growth rate (CAGR). The number of connected devices and connections will reach 29.3 billion by 2023, of which 12.3 billion will consist of mobile devices [2]. With an exponential traffic growth of mobile devices, wireless communication researchers and industry have tried to satisfy an estimated 1000x increase requirement in traffic capacity [3]. From this point of view, researchers have begun research on beyond fifth-generation (B5G) and even sixth-generation (6G) technologies. In the B5G/6G area, more diverse network services, i.e. the virtual reality (VR) and the augmented reality (AR), not only place new demands on network traffic capacity, but also pursue higher spectrum efficiency (SE) and energy efficiency (EE). The various application scenarios have put forward three main requirements for the B5G/6G network, enhanced mobile broadband, ultra-reliable and low-latency communications [4]. Therefore, a new paradigm at the physical layer of the wireless communication system needs to be established.

1.1.2 The 3-D MIMO System

To meet the 1000x increase traffic demand, massive multiple-input multiple-output (MIMO) and millimeter wave (mm-wave) are two key technologies enabling to improve the SE and pursue high data rate in the B5G networks. In the real world, the channel features three-dimensional (3-D) characteristics, which can be described in vertical and horizontal planes. Accordingly, 3-D MIMO technology with two-dimensional (2-D) grid is emerged. Since the physical size of the antenna operating in the mm-wave frequency band has been greatly reduced, it is possible to arrange a very large number of antenna elements on a smaller plane at the base station, which is believed to improve the SE greatly through high-order spatial multiuser multiplexing. Several signal processing technologies, e.g. beamforming, maximal ratio combining (MRC), zero-forcing, are applied to generate the directional beams to enhance the received signal strength [5]. For the 3-D MIMO system, equipped large-scale planar antenna arrays is a feasible method to exploit both vertical and horizontal domain beamforming for signal transmission. Such improvement of spatial resolution in 3-D space benefits to enhance the desired signal power in expected directions. Meanwhile, the inter-cell interference can be reduce from other directions [6].

Many exciting efforts of 3-D MIMO have been achieved from performance analysis to implementations, which related to channel model, channel estimation, signal processing schemes, and detection algorithm [7–10]. Some papers indicate that the 3-D MIMO design can satisfy the SE requirement of the 5G/B5G network [6]. Compared with the traditional 2-D MIMO system, the 3-D MIMO can enhance the cell throughput by nearly 6 times [11].

Combined with the mm-wave technology, the 3-D MIMO has been widely investigated for full exploitation of the resources in the spatial-domain and beamspace-domain, and an easier implementation due to the smaller physical size of antenna arrays. It enables the realization of a large-scale MIMO antenna array, which can be leveraged to achieve narrow and directional beams. The 3-D MIMO system utilises spatial-domain resources to improve the channel diversity gain and system throughput without increasing the bandwidth and transmit power. Meanwhile, the signal reliability is increased by the multiple antennas at the transceivers. Besides, the extra degree of freedom (DoF) created by 3-D MIMO benefits to reduce the inter-cell interference, especially in the complicated transmission environment. Compared with conventional 2-D uniformly liner array, 3-D MIMO with planar array has better resolution in the elevation domain. Recently, the 3-D MIMO channel model is released by third generation partnership project (3GPP), which considers the planar antenna arrays and the full dimension beamforming scheme [12]. In general, the MIMO system can achieve a capacity and diversity gain with the antenna arrays at the transceivers [13].

The development of the MIMO technology allows the multiple transmit antennas generated at a time slot, where the indices of transmission antennas can be applied as an extra source of the input information in the spatial dimension in addition to the conventional modulation constellations. Meanwhile, the utilisation of large-scale antenna arrays can generate the directional beams in beamspace-domain to convey the extra information bits. The above methods utilise the different domain resources of MIMO system to enhance the conventional modulation scheme, which is collectively called index modulation (IM). In the next subsection, the IM schemes will be introduced in detail.

1.1.3 The Index Modulation

For the conventional modulation systems, the information is modulated by adjusting the amplitude or phase of the sinusoidal signal. However, the conventional modulation schemes cannot meet the throughput and EE requirements of the 5G/B5G networks. Based on MIMO systems, a novel modulation scheme has been promoted to gratify above requirements, which named spatial modulation (SM). The SM technology applied the index of transmission antennas to convey the information bits. For the detector, the optimum detection algorithm is designed to decide the transmitted symbols on the constellation map and the index of activated antennas [14]. After the SM scheme proposed, its idea was expanded in different domains to improve communication capacity without additionally occupying spectrum resources. Consequently, the modulation systems are no longer limited to modulating a sinusoidal carrier signal with amplitude, phase, and frequency, which also utilises various indices resources, e.g., subcarriers, antenna elements or transmission paths, to convey additional information bits. These novel modulation schemes become a research hot-spot over the past few years, which are collectively known as IM [15].

Existing IM technologies can be categorized according to the domain in which the additional IM bits are modulated, which mainly includes the spatial-domain IM, the frequency-domain IM, the beamspace-domain IM and the polarization-domain IM, etc. For IM schemes, a part of information bits are conveyed through the traditional amplitude and phase modulation, while the other part of information bits represented by the indices are received directly without additional energy consumption. Therefore, with the same energy consumption as the conventional modulation schemes, IM schemes can significantly increase system throughput and improve EE. Moreover, with the flexible structure of the IM frame, the diversity gain can be significantly enhanced by the type of constellation map, diverse indices entities or the selection of transmission path. The diversity gain of IM schemes contributes to the considerable performance improvement over the transitional modulation scheme. Due to its outstanding performance, IM has been discussed in various communication scenarios with different formats, such as OFDM precoding, massive MIMO, and mm-wave transmission [15].

As a mainstream IM scheme, the spatial scattering modulation (SSM) system is proposed in [16], which extends the IM technology into the beamspace-domain with the large-scale MIMO. In the SSM system, the input information bits are modulated not only by the conventional modulation symbols, but also by the positions index of the different signal scattering paths. Thus, the throughput of the SSM system is determined by the modulation order and the number of scattering paths in different directions. In this way, the SE can be improved, even the conventional modulation order is low and the number of radio-frequency chains (RF-chains) is limited. Meanwhile, compared with traditional SM systems, due to the smaller constellation maps, the SSM has better bit error performance under the propagation environment with abundant scattering paths.

1.2 Motivations and Contributions

1.2.1 Motivations

As presented above, the SSM technology explores the beamsapce-domain resource to improve the SE. Inspired by the concept of full-dimensional MIMO systems, the SE and bit error performance of SSM systems can be further improved. With the iterative deepening of 3-D channel modelling research, the 3GPP Release has introduced the 3-D MIMO system, which utilises beams in both elevation and azimuth angles. Compared with the 2-D MIMO, the 3-D MIMO can achieve higher resolution beams in the 3-D space. Based on the 3-D MIMO technologies, the SSM system can adopt the DoF with elevation angles in the beamspace-domain with planar arrays. Most state-of-the-art works discuss the SSM system with the linear antenna arrays, which only take the azimuth angles to recognise the direction of scattering paths. To take the full advantage of the beamspace-domain resources, besides the azimuth angles of arrival (AoA) and angles of departure (AoD), the elevation AoA and AoD should be considered for the SSM system.

Meanwhile, for the 3-D MIMO system applying beamforming technologies, the mutual interference generated by side beams, and the correlated noises at the receiver seriously affect the system performance. However, existing works have assumed that the received array vectors are orthogonal with each other, and the noises at received RF-chains are supposed to be independently distributed, which do not match the reality. Above mentioned issues have not been considered and resolved in the existing papers about SSM technologies.

For the 3-D SSM system, the SE can be further improved by applying hybrid beamforming technologies with several RF-chains. The combinations of scattering paths in each transmission time slot can be used to convey the extra information bits. With multiple RF-chains, the 3-D SSM may obtain better diversity gain due to the increased number of scattering path combinations, and a generalised bit mapping scheme should be designed. Nevertheless, the system error performance may be degraded due to the utilisation of the more complex constellation map. A performance analytical framework needs to be established to evaluate the 3-D SSM system with multiple RF-chains.

In practical deployment, as a modulation system based on large-scale antenna arrays, the complexity and cost of the 3-D SSM system should be considered. Therefore, in addition to the system design and the performance evaluation, optimisation schemes should be designed to reduce the complexity and deployment cost of 3-D systems. Firstly, due to the implementation of large-scale antenna arrays, the number of antenna elements on the transceivers usually reaches 64, 128 or even 256. Since each antenna element demands to be configured with a corresponding RF-link, the system requires a large analogue phase shifter network to support the beamforming process, which significantly increases the deployment cost of the base station. Therefore, the hardware friendliness design for the 3-D SSM system with a planar array needs to be considered. Secondly, for 3-D SSM systems, the computational complexity of the optimum detection algorithm will increase geometrically with the number of scattering paths and the modulation order, especially when the system generates multiple RF-chains. To reduce the computational complexity of the detection algorithm, a low-complexity detection algorithm should be designed. Thirdly, the simulation process is time-consuming for the 3-D SSM system with large-scale antenna arrays. Therefore, a fast and accurate evaluation approach needs to be designed.

In this thesis, we aim to extend the SSM system to 3-D space, which can enhance SE and improve the resolution of scattering paths. Combining with hybrid beamforming technologies, the 3-D SSM system with multiple RF-chains can be designed, which may further improve the SE and system throughput. To evaluate the performance of the 3-D SSM system, an analytical framework needs to be established. For practical deployments, several optimisation schemes should be provided.

1.2.2 Contributions

The main contributions of this thesis are briefly summarised as follows.

- A novel 3-D SSM system is proposed, which takes both azimuth and elevation angles into account to recognise the direction of scattering paths. Therein, two streams of bits can be conveyed by the selected scattering path and the transmitted symbol.

- Due to the linear combination operated by phase shifters at the receiver, noises of the receiving RF-chains are correlated. In other words, side beams lead to mutual interference and correlation of noises among receiving RF-chains, and slightly generate additional received power. Accordingly, a whitening filter based maximum likelihood (ML) detection algorithm is proposed for the 3-D SSM system.

- For efficient evaluation and comparison of 3-D SSM systems, a closed-form expression of the union upper bound on the average bit error probability (ABEP) is derived. Numerical results show that the generalised 3-D SSM system outperforms the conventional 2-D SSM system, which reduces the ABEP by 10 times with the same SNR level under the typical indoor environment.

- The generalised 3-D SSM system with multiple RF-chains is modelled and analysed in this thesis, which can further improve the system throughput compared with a single RF-chain. Meanwhile, an optimum detection algorithm is designed for the generalised 3-D SSM system.

- Based on the ABEP union upper bound expression of the generalised 3-D SSM, the system performance is evaluated under the statical and stochastic propagation environments. The results reveal that the system bit error performance can be further enhanced, when the multiple RF-chains are activated.

- When large-scale planer arrays are applied to the generalised 3-D SSM system, the computational complexity of the optimum detection algorithm will exponentially rise. Therefore, a low-complexity linear detection algorithm based on the minimum mean square error (MMSE) scheme is designed.

- For the generalised 3-D SSM system with an analogue phase shifter network, a hardware friendliness design for transceivers is investigated. The implementation of multi-bit phase shifter networks is obtained to reduce the hardware deployment cost.

- For the quick evaluation, the asymptotic performance and the diversity gain of the generalised 3-D SSM system are derived.

1.3 Structure of the Thesis

The content of this thesis is organised as follows.

Chapter 2: Literature Review

This chapter comprehensively reviews the basic concepts and modelling scheme of 3-D MIMO system in the literature, and introduces several mainstream IM strategies. Then the performance evaluation and optimisation methods of related IM systems are also reviewed. Meanwhile, the basic system structure of the 2-D SSM system is presented.

Chapter 3: The System Design and Performance Analysis of 3-D SSM System

The system model of 3-D SSM is designed in this chapter, which considers the correlated noise at the receiver and the non-orthogonality between receiver array vectors. Then the optimal detection algorithm is derived. Moreover, the closed-form expressions of union upper bound on the ABEP is derived. Finally, combining the numerical and simulation results, the ABEP performance is analysed under the typical indoor environments.

Chapter 4: The Generalised 3-D SSM System

The system model of generalised 3-D SSM with multiple RF-chains is designed in this chapter. The optimal detection algorithm is also derived for the generalised 3-D SSM system. The closed-form expression of union upper bound on the ABEP is derived and validated under the typical indoor environments. Finally, the ABEP performance is analysed under several stochastic propagation environments with randomly distributed scatterers.

Chapter 5: Optimisation Schemes of Generalised 3-D SSM Systems

In this chapter, the 2-D fast Fourier transform (FFT) based transceivers are designed at first, which aim to reduce the hardware complexity of phase shifter networks. Then, the performance of the generalised 3-D SSM system with a 2-D FFT transceiving approach is evaluated. Furthermore, to reduce the computational complexity of the optimum detection algorithm, the linear MMSE detection algorithm is introduced. Finally, the asymptotic performance and the diversity gain of the generalised 3-D SSM system are derived.

Chapter 6: Conclusions and Future work

This chapter summarises the works of this thesis and presents the future works.

Chapter 2

Literature Review

Overview

In this chapter, the basic concept and system structure related to 3-D MIMO system is firstly introduced. Then the state-of-the-art IM systems are presented, which include spatial-domain IM, frequency-domain IM, spatial-domain IM and beamspace-domain IM. Finally, performance evaluation and system optimisation schemes of IM systems are also summarized.

2.1 The MIMO Technologies

2.1.1 The 2-D MIMO systems

In the mid-1990s, the spatial multiplexing via antenna arrays was proposed by Foschini, which gives a new route to boost the system throughput with limited bandwidth [17]. The BS equipped with amount of antennas can supply simultaneously service for multiple UEs with the same time-frequency resource. The existing works indicated that the MIMO system can provide the considerable performance improvement in terms of SE, EE and channel reliability [18]. The single-user MIMO (SU-MIMO) is one of the mainstream of MIMO technologies, which applied multiple antennas to serve a single UE. The SU-MIMO significantly improve the transmit diversity with the spatial multiplexing, which is an efficient method to enhance the robust of the wireless communication system. In long term evolution (LTE) standard, the BS transmits the pilot for estimating the channel information, which is used for control channel and data channel. Meanwhile, the spatial multiplexing in the LTE is mainly targeted at cell centre users.

For the multiple user scenario, multiple-user MIMO (MU-MIMO) was widely studied as the key technology in the wireless network. In MU-MIMO systems, the spatial multiplexing gain is no longer concentrated on a single user. The UEs with same time-frequency resources shared the multiplexing gain. On the other hand, the multiplexing gain of MIMO systems is constrained by the design and array size of UE's antennas. In general, the MU-MIMO system is more feasible to support a lager number of users in a cellular network [19].

In the early design of antenna array, linear arrays were generally considered. The linear array can only identify the angle of arrival (AoA) of beams in the horizontal dimension. For the cellular system with traditional 2-D MIMO, the BS equipped with passive antenna array, and only adjust the beam in a single dimension with fixed downtilt direction. However, in the real world, the spatial multiplexing can be achieved in both horizontal and vertical dimensions. To explore the potential of spatial multiplexing, the electromagnetic wave propagation needs to be considered in the 3-D real world.

2.1.2 The 3-D MIMO Systems

The 3-D MIMO, as a type of MIMO technologies, has been widely investigated for fully exploitation of the resources in the beamspace-domain, and an easier implementation due to a smaller physical size of planar antenna arrays [6]. The main technical issues and fundamentals of 3-D MIMO have been deeply studied and determined, which mainly include channel measurement, channel modelling and interference coordination.

For the 3-D MIMO channel measurement, thanks to the measurement equipment deployment, many published papers obtained the results in several typical transmission scenario. In [20], the authors applied a low-cost channel sounder and the post-processing algorithm to obtain spatial-domain characteristics in an outdoor-to-indoor environment. With a hybrid cylindrical array equipped effectively 480 antenna elements, the angular spreads of elevation and azimuth dimensions were provided under the urban macro-cellular and the urban micro-cellular scenarios. Meanwhile, the feasibility of splitting UEs in the elevation dimension and the phase drift error estimation were also studied in [20]. The authors in [21] reported the measurement results in a typical urban macro environment, which obtained the stochastic channel model parameters based on the high-resolution multiple paths parameter estimates. In [22], a 56×32 antenna array at 3.5 GHz with 100 MHz bandwidth was utilised to measure three typical application scenarios, i.e., outdoor-to-indoor, urban microcell and urban macrocell. The stochastic behaviours of elevation and azimuth angles were observed. The results in [22] indicated that the outdoor-to-indoor is the most beneficial among the three typical scenarios.

With the development of 3-D MIMO technologies, the 3-D fading channel model is attracting more and more attention. In [1], a state of the art results related to elevation angle characteristics for 3-D fading channel model was summarized. Combining with the some field measurement results, the propagation characteristics of the elevation angle were also obtained. In [23], a generalised 3-D scattering channel model was introduced. With the uniformly distributed scatterers in the hemispheres around the antenna array, the model delineated the AoA in the azimuth and elevation planes for the multipath signals. Meanwhile, the authors in [23] first derived the probability density function (PDF) of the AoA under the scattering channel with a closed-form expression, and the Doppler spectral distribution with the dynamic UE was also obtained. According to the measurement and numerical results, the 3-D scattering channel model proposed in [23] has the better performance compared with the 2-D model.

According to [1], the frameworks of 2-D and 3-D fading channel are shown in Fig. 2.1(a) and (b), respectively. For the 2-D framework, AoAs and AoDs of the multipath components are defined as $\phi_{TX,I}$ and $\phi_{TX,I}$. The 2-D framework reflects the situation when the antenna array is a linear array, and the elevation planar has been ignored in the model. Considering the scatterers in the 3-D space, the AoAs, AoDs, the positions of devices and the mobility direction are defined in the global coordinate system. In the azimuth planar, the AoAs and

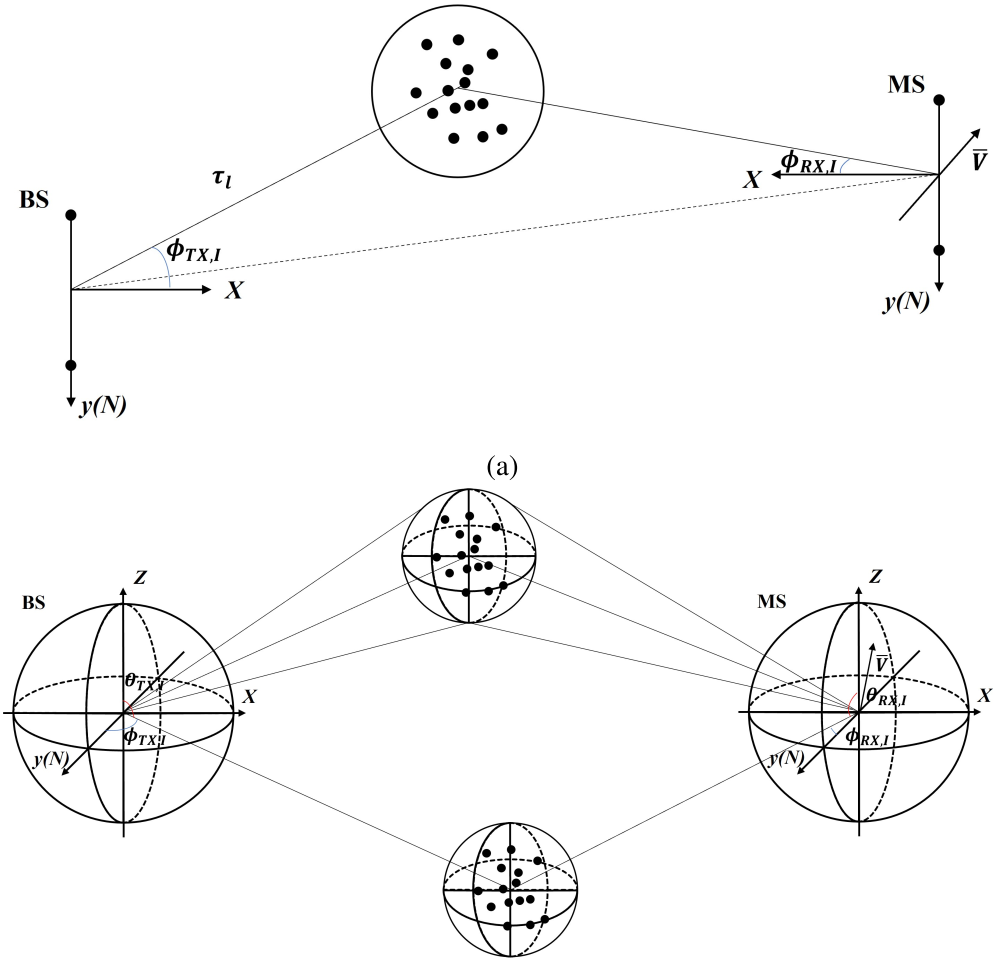

(a)

(b)

Fig. 2.1 The framework of 2-D and 3-D fading channel models [1].

AoDs are represented by $\phi_{TX,I}$ and $\phi_{RX,I}$, respectively. Consequently, the AoAs and AoDs in the elevation planar are represented by $\theta_{TX,I}$ and $\theta_{RX,I}$, respectively. Thus, the beam angle information at the sender side is determined by $\{\phi_{TX,I}, \theta_{TX,I}\}$, and the beam angle information at the receiver side is determined by $\{\phi_{RX,I}, \theta_{RX,I}\}$.

For the 3-D MIMO system, the inter-cell interference (ICI) is regarded as one of the main problems resulting in SE degradation. To limit the negative impact of ICI, the cooperative 3-D beamforming technology is widely discussed. The existing beamforming schemes can be divided into two categories based on the channel state information (CSI) type, i.e. the instantaneous CSI and the statistical CSI [24]. With the instantaneous CSI, in [25, 26], the cooperative beamforming strategies were proposed to improve the SE of 3-D MIMO systems.

With the statistical CSI, the authors in [27] designed the beamforming strategy based on the spatial channel correlation matrices. Moreover, a beamforming strategy, which considered both the beamforming vectors and the user association factors, was proposed in [28] to maximizing the lower bound of the signal-to-leakage-and-noise ratio (SLNR). The results indicated that the algorithm in [28] can significantly improve the achievable sum rate of the BS. With the statistical CSI, in [29], a novel interference coordination algorithm was proposed to balance the data rate between macro-cells and small cells. Furthermore, the lower bound of the UE expected SLNR was also obtained in [29] based on the property of Wishart matrix. In [30], the fractional-frequency-reuse scheme was proposed for the 3-D MIMO system. For the fractional-frequency-reuse scheme, all cell-center UEs were served by the same frequency band, and the remaining frequency bands were applied by mobile-edge devices. Based on the fractional-frequency-reuse scheme, the full-cooperative strategy and energy-efficient partial-cooperative strategy were investigated to reduce the ICI [30]. For the multiple-input-single-output (MISO) system, the optiaml downtilt was obtained based on the three dimensional user distribution in [31], and the average rates of the MISO system was also derived. For the network level beamforming strategy with multiple tiers of UEs, the authors in [32] proposed a region-partition 3-D beamforming strategy, which provided a specific downtilt for each UE.

2.2 The IM Technologies

For the IM technologies, the system no longer limited to modulating a sinusoidal carrier signal with phase, frequency and amplitude, which applies other indices resources, e.g. subcarriers, transmission path or antenna elements. In this subsection, several mainstream IM technologies will be introduced, including the spatial-domain IM, the frequency-domain IM, the time-domain IM and the beamspace-domain IM.

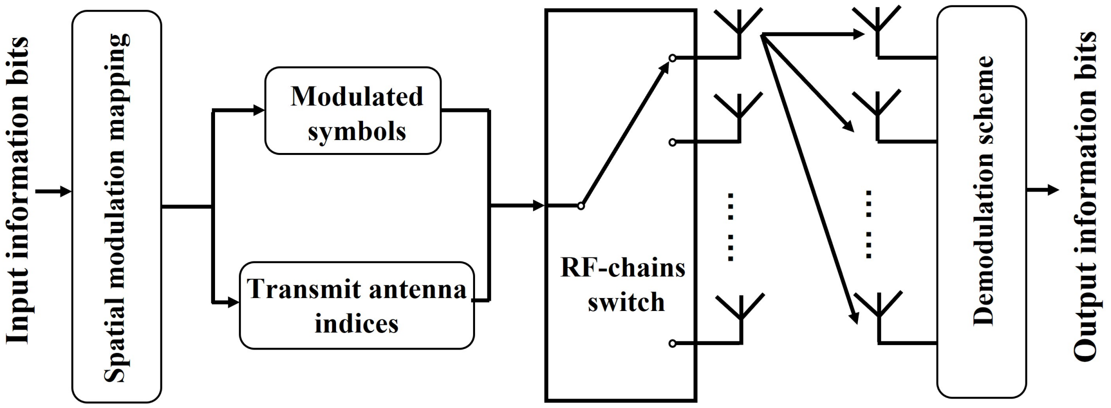

Fig. 2.2 The system model of SM.

2.2.1 The Spatial-Domain Index Modulation

As a well-known IM technology, SM exploits the DoF in the spatial domain with MIMO system to improve the SE [14, 33–37]. The SM employs well-known amplitude/phase modulation schemes and antenna indices to convey information bits. The bit-to-symbol mapping rule of SM system can be divided into three steps. Firstly, the input information bits need to be separated into several vectors, which includes $m = \log_2(AN_{\mathrm{t}})$ bits, where N_{t} is the total number of the transmitted antennas, and A is the modulation order of the conventional modulation scheme. Secondly, each vector is split into two group, where $\log_2(N_{\mathrm{t}})$ bits are conveyed by the unique activating transmission antenna, and $\log_2(A)$ bits are mapped to an amplitude/phase modulation symbol. Thirdly, the modulated SM signal, which contains of the conventional mapping symbol, is emitted from the selected transmission antenna. The basic structure of the SM system is shown in Fig. 2.2.

After Chau *et al.* firstly proposed the conventional SM scheme [33], the modulator design of SM has been expanded in different ways. In [38], the orthogonal spatial-division multiplexing (OSDM) scheme was proposed, which first applied the index of the transmission antennas as an additional information carrier. In [14], the framework of the bit-to-symbol mapping was designed for SM, and the beneficial of SM system on the bit error performance was compared with the other MIMO schemes, such as the Vertical-bell lab layered space-time (V-BLAST). Except for the phase shift keying (PSK) and quadrature amplitude modulation (QAM) schemes, the space shift keying (SSK) was proposed in [39], which exclusively utilise the indices of transmitted antenna to convey information bits. Above mentioned SM schemes only active a single antenna element at each transmission time slot to reduce the system complexity and power consumption.

For the classic SM system [33], only one of the antennas is activated during the transmission time slot, which avoids the inter-channel interference and the inter-antenna synchronisation problems. In [34], the generalised space shift keying (GSSK) was first proposed, which allowed several antenna elements to transmit different modulated symbols at the same time interval. Specifically, the generalised SM (GSM) transceiver designed in [40] sends the same modulated symbol by all transmitting antennas to increase the diversity gain. Meanwhile, in [36] and [41], the active transmitting antennas emitted different modulated symbols during a transmission time slot to increase multiplexing gain for the SM system. The authors in [37] proposed the space-time block coding-spatial modulation (STBC-SM) scheme, which applied space-time block code to improve the SE for SM systems. The space-time block encoder first process the mapping symbol at the transmitter, and the modulated symbols are emitted from several selected antennas. Above mentioned SM schemes utilised multiple transmitting antennas and allowed several bit-to-symbol mapping at a transmission time slot.

For the SM detector, the antenna index and the transmitted amplitude/phase modulation symbol need to be estimated. The detection algorithm can be classified into four categories, i.e., ML detection, matched filter (MF) based detection, hybrid detection and sphere decoding (SD) detection. For the optimum ML detector, the authors in [42] proposed the detection algorithm to search the entire signal space. In [43], a soft-output ML detection algorithm was designed, which retrieved the desired signals based on the soft decision schemes. In [44], a semi-blind joint channel estimation and detection algorithm was proposed. It applied the inherent ML detection to reduce the training overhead required based on a rough initial least square channel estimation (LSCE). Nevertheless, if the ML detection algorithm is applied, all possible transmission vectors need to be traversed, which will lead to the exponential growth of the computational complexity with the increase in transmission rate. Consequently, several ML-based detectors were proposed to reduce the computational complexity of detection algorithms, which separately detects the index of the transmitting antenna and the modulated symbols [45–47].

The authors in [5] proposed the classic MF detection algorithm, which was named MRC. The MRC algorithm requires the perfect CSI, otherwise the performance will significantly reduce. Moreover, the MRC detector was optimised in [48] for the SM system with the unconstrained channel, which had the less complexity compared with the optimal ML detector. Without the optimum global searching, the MF algorithm will sacrifice a part of throughput in exchange for lower complexity. In order to maintain the throughput of the system as much as possible, the hybrid detection algorithm was proposed.

The hybrid detection algorithms combine the MF schemes and the searching mechanism of ML. The exhaustive-search-based MF (EMF) detector and near-optimal MF (NMF) detector were designed in [49]. For the EMF detector, the received signal is first demodulated by the MF detection algorithm for a part of the information bits. Then the output of MF detection is produced by the exhaustive search following the ML mechanism, which achieves the reduction of computational complexity and maintains the ML's performance. To further reduce the computational complexity of the EMF detection algorithm, the NMF detector was designed [49]. Moreover, the improved NMF detectors were proposed in [50, 51].

Additionally, the SD schemes were widely studied for the SM systems, which replaced the exhaustive search of constellation maps by the selection of several candidate results based on the SNR-dependent decoding sphere. Nevertheless, the application of the conventional SD scheme has some limitations, e.g., only a signal transmitted antenna is active for each time instant [52]. Therefore, a specific design for SD schemes is required to accommodate SM-MIMO systems. In [53], the SD-SM algorithm was proposed. It modified the mapping scheme of SM systems, and adjusted the sphere radius based on the noise level at the receiver. Meanwhile, the authors in [54] designed a generalised version of the SD-SM algorithm. However, the shortcoming of the SD-SM algorithm is that the selection of the initial sphere radius will seriously affect the system performance.

2.2.2 The Frequency-domain Index Modulation

Based on the OFDM technologies, frequency-domain IM has attracted considerable attention recently[55]. Frequency-domain IM is also called orthogonal frequency division multiplexing IM (OFDM-IM) [56], which applies the indices of orthogonal subcarriers to convey extra information bits rather than only utilises the M-ary signal constellations. The OFDM-IM system has multiple variants, such as dual-mode OFDM-IM and MIMO-OFDM-IM systems. The OFDM-IM systems have also been extended for different application scenarios, i.e., the vehicle-to-vehicle (V2V), device-to-device (D2D) and optical OFDM etc.

The authors in [57] first proposed the OFDM-IM system, which was evaluated based on the frequency-selective and time-varying fading channel. In [55], generalised multiple-mode orthogonal frequency division multiplexing with index modulation (GMM-OFDM-IM) was proposed, which applied the indices of subcarriers and the permutation of distinguishable constellations to convey the additional information. With different subcarriers to carry constellations of various sizes, the results indicated that the GMM-OFDM-IM enhanced the SE and EE, compared with the OFDM-IM system [55]. Moreover, the authors in [58] proposed a layered OFDM-IM scheme, where the indices of active subcarriers from all layers were utilised to convey the extra IM bits. In additional, the zero-padded tri-mode IM aided OFDM (ZTM-OFDM) was proposed in [59], which modulated two distinguishable constellation alphabets in each active OFDM subblock. The additional IM information bits were conveyed by indices of subcarriers, which related to the selected constellation maps.

In [60], the author proposed OFDM with generalised index modulation (OFDM-GIM) to further improve SE at the cost of increasing system complexities. Two generalisation schemes of OFDM-GIM were designed. In the first scheme, the number of active subcarriers for each OFDM subblock was not fixed, which was determined by the input binary string. The active subcarriers were utilised to carry constellation symbols. In the second scheme, each subcarrier applied independent IM on the in-phase and quadrature component. Moreover, the combination of the above two schemes was also investigated in [60].

To enhance the throughput of the OFDM-IM, the dual-mode OFDM (DM-OFDM) technique was proposed in [61], where subcarriers were separated into several groups of subblocks, and all subcarriers were partitioned into two groups for the modulation. A pair of distinguishable constellations were applied on active subcarriers. The ML detector and the low-complexity near-optimal log-likelihood detection algorithm were also designed in [61]. And the authors in [61] derived the pairwise error probability (PEP) for evaluating the bit error rate (BER) of DM-OFDM. Furthermore, the Generalised DM-OFDM (GDM-OFDM) proposed in [62] modulated the alterable number of subcarriers with the same constellation scheme. When the SNR was low, an interleaving technique was also employed to solve this problem. By applying such enhancements, the SE could be further improved by the GDM-OFDM technique. The simulation results indicated that the SE of GDM-OFDM outperformed the DM-OFDM, and the interleaved GDM-OFDM could achieve extra performance gain over GDM-OFDM.

Combining with the MIMO technique, the MIMO-OFDM-IM system was proposed in [63]. The transmitter utilised the V-BLAST scheme for each antenna element, and each antenna element modulated its OFDM-IM frame. After the OFDM-IM frames separated at the receiver, a low-complexity MMSE detection algorithm was designed for the demodulation. The results indicated that the MIMO-OFDM-IM scheme could achieve better BER performance than the conventional MIMO-OFDM system with several antenna configurations. With the different application scenarios and system complexity constraints, the ML, near-ML, simple MMSE and ordered successive interference cancellation-based detection algorithms for the MIMO-OFDM-IM system were proposed in [64]. With different detection algorithms introduced in [63, 64], they provided a trade-off between bit error performance and SE, and achieved a significant performance improvement compared with conventional MIMO-OFDM systems with different types of detection algorithms.

2.2.3 The Time-domain Index Modulation

IM schemes can also be arranged in the time-domain, which activates a fraction of the signalling time slot to convey information [65]. The classic single-carrier IM (SCIM) was proposed in [66], which applied the indices of the activated time slot to convey information bits. Meanwhile, the authors in [66] also designed the low-complexity frequency-domain equalisation (FDE) algorithm to reduce the computational complexity. A novel dual-mode SCIM (DM-SCIM) scheme was proposed in [67], where two different constellation alphabets were applied for conveying extra information bits. Hence the further index could be utilised to modulate symbols, which increase the system throughput. The error-rate bound of the DM-SCIM was also derived. The simulation results demonstrated that the performance of the DM-SCIM scheme was better than the classic SC scheme [67]. The transmission rate of time-domain IM schemes mentioned above applied the conventional time-orthogonal Nyquist-criterion-based transmitter, which requires a minimum symbol interval to avoid inter-symbol interference [66].

Combining with the multi-antenna modulation scheme, the space-time IM (STIM) was proposed in [68]. The information bits in STIM were conveyed by the active antennas, the time slots, and the constellation symbols. For the STIM, the constellation symbols were sent on the different active antennas, and the antenna indices were determined by selecting one among the available antennas in a time slot. To further improve the SE, the authors in [69] proposed the Space-time shift keying (STSK) scheme with the MIMO system, which extended the SM scheme to the time dimensions. Specifically, the STSK scheme activated one out of Q dispersion matrices during the transmission block to convey the extra information bits [69]. The STSK scheme optimised the space-time block duration, and the number of the dispersion matrices in addition to the number of transceiver antennas. Moreover, the enhanced STSK scheme was also proposed in [69], which neglected the requirement of inter-antenna synchronisation by applying a specific constraint on the dispersion matrix design.

A novel generalised STSK (GSTSK) architecture was proposed in [70]. Compared with the STSK scheme mentioned above, the G-STSK utilised p out of Q dispersion matrices to modulate the extra information bits based on conventional PSK/QAM modulations. The simulation result indicated that the STSK/G-STSK outperformed the conventional SM/SSK schemes. Moreover, with differentially encoded STSK (DSTSK), the differential SM (DSM) was proposed in [69], which enables non-coherent detection and maintains the information bit stuck in each channel [56]. Furthermore, in [71], the IM scheme with multiple transmission entities was proposed, which integrated time slots, antennas and RF mirrors. Multiple transmission entities were indexed simultaneously, namely multidimensional IM. Due to the sparsity of the signal vector, a compressive sensing based reconstruction algorithm was designed for the multidimensional IM detector. However, the limitation of the symbol interval constrained the capacity of the time-domain IM systems. Therefore, the faster-than-Nyquist (FTN) [72] transmission scheme relying on the time-domain SC-IM was designed in [73]. Combining the FTN-IM and the time-domain IM scheme, the SC-IM indices conveyed additional information bits, and the FTN reduce the inter-symbol interference. Simulation results indicated that the FTM-IM scheme outperforms the classic FTN system under the additional white Gaussian noise and the frequency-selective fading channel.

2.2.4 The Beamspace-domain Index Modulation

Recently, the SSM has been proposed to achieve a higher SE, which applied the beamspace-domain resource[16]. For SSM systems, the extra information bits were expressed by the recognisable signal scattering paths, which were accomplished by beamforming technology. Therein, two information bit streams were transmitted simultaneously by selections of modulated symbols and scattering paths. In [16], the author employed a large linear array at the UE and the BS, which could provide a narrow and directional beam to transmit signals for the uplink transmission. With the linear array antennas, directions of scattering paths were recognised in the angular domain. In [74], the diversity order of the 2-D SSM system was obtained for the quick performance evaluation. Considering the polarisation-domain resources, a polarised SSM system was proposed in [75]. The authors also derived the closed-form ABEP expression for the polarised SSM system [75]. The IRS-aided SSM system was proposed in [76], which aimed to provide an enhanced transmission environment with diverse scattering paths. The results reveal that the proposed IRS-aided SSM has a considerable lower BER than the classic SSM.

The basic structure of the SSM system with the linear array is shown in Fig. 2.3. Following the system model in [16], the BS is equipped with multiple RF-chains, and the phase shifters of each RF-chain are connected with every antenna element. Due to the

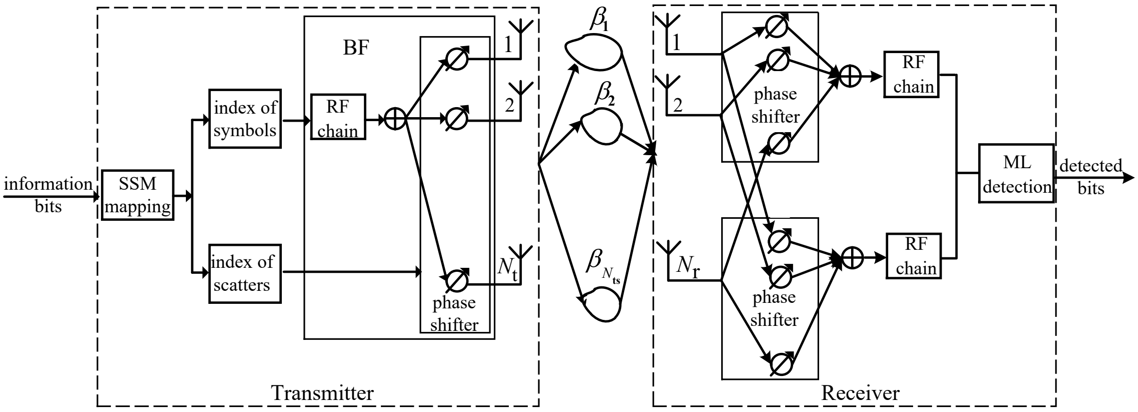

Fig. 2.3 The basic structure of the SSM system with a linear array.

limitation of the available RF-chain, only a single stream can be generated to transmit the modulated symbol. With the narrowband physical channel model, the channel matrix $\mathbf{H}$ is derived as follows.

$$\mathbf{H}=\sum_{l=1}^{N_\mathrm{ts}}\beta_l\mathbf{a}_\mathrm{r}\left(\theta_l^r\right)\mathbf{a}_\mathrm{t}^H\left(\theta_l^t\right), \tag{2.1}$$

where N_ts is the total number of scattering paths, β_l is the complex gain of the l-th path, the AoA and AoD are represented by θ_l^r and θ_l^t, respectively. The array vectors $\mathbf{a}_\mathrm{r}\left(\theta_l^r\right)$ and $\mathbf{a}_\mathrm{t}\left(\theta_l^t\right)$ can be represented as follows.

$$\mathbf{a}_\mathrm{r}\left(\theta_l^r\right)=\frac{1}{\sqrt{N_r}}[1,e^{j2\pi\phi_l^r},e^{j4\pi\phi_l^r},...,e^{j2(N_\mathrm{t,v}-1)\pi\phi_l^r}]^T, \tag{2.2}$$

$$\mathbf{a}_\mathrm{t}\left(\theta_l^t\right)=\frac{1}{\sqrt{N_t}}[1,e^{j2\pi\phi_l^t},e^{j4\pi\phi_l^t},...,e^{j2(N_\mathrm{t,h}-1)\pi\phi_l^t}]^T, \tag{2.3}$$

where N_r is the total number of antenna elements at the receiver, N_t is the total number of antenna elements at the transmitter, $\phi_l^r=\frac{d_r}{\lambda}\sin\left(\theta_l^r\right)$, $\phi_l^t=\frac{d_t}{\lambda}\sin\left(\theta_l^t\right)$, d_r and d_t are the distance between the antenna elements for the receiver and transmitter, respectively, λ is the wavelength [77].

The authors in [16] assumed the narrow directional beams, which meant an approximate orthogonality. Therefore, if $l\neq k$, we have $\mathbf{a}_\mathrm{t}\left(\theta_l^t\right)^H\mathbf{a}_\mathrm{t}\left(\theta_k^t\right)\approx 0$ and $\mathbf{a}_\mathrm{r}\left(\theta_l^r\right)^H\mathbf{a}_\mathrm{r}\left(\theta_k^r\right)\approx 0$. With the orthogonality beam vectors, the interference among scattering clusters was also

Table 2.1 The example of SSM bits mapping scheme

$[s_0, s_1]$	00	01	10	11
	$a_t\left(\theta_1^t\right)$	$a_t\left(\theta_2^t\right)$	$a_t\left(\theta_3^t\right)$	$a_t\left(\theta_4^t\right)$
$[s_2, s_3]$	00	01	10	11
	$\frac{1+1j}{\sqrt{2}}$	$\frac{1-1j}{\sqrt{2}}$	$\frac{-1+1j}{\sqrt{2}}$	$\frac{-1-1j}{\sqrt{2}}$

limited. Therefore, the relationship between $\mathbf{a}_{\mathrm{r}}\left(\theta_l^r\right)$ and $\mathbf{a}_{\mathrm{t}}\left(\theta_l^t\right)$ can be represented as

$$\mathbf{a}_{\mathrm{t}}\left(\theta_l^t\right)^H \mathbf{a}_{\mathrm{t}}\left(\theta_k^t\right) = \delta(l-k), \quad \mathbf{a}_{\mathrm{r}}\left(\theta_l^r\right)^H \mathbf{a}_{\mathrm{r}}\left(\theta_k^r\right) = \delta(l-k), \tag{2.4}$$

where $\delta(\cdot)$ denotes the Dirac delta function.

The basic form of modulated SSM symbols and the detection scheme are is described below. At the transmitter, the direction of the signal beam is determined by the information bits. The SSM system selects $N_s \leq N_{\mathrm{ts}}$ scattering paths as the candidate transmission directions. After the precoding, the information conveyed by a modulation symbol consists of two parts. The first part is the information bits modulated by the conventional modulation scheme, and the number of bits carried by this part of symbols can be calculated by $\log_2(M)$, where M is the modulation order. Another part of the information is carried by the scattering path. With N_s candidate scattering paths, the maximum number of bits can be sent in this part is $\log_2(N_s)$. Therefore, the total number of information bits conveyed by a modulated symbol can be calculated by $\log_2(M) + \log_2(N_s)$. Taking QPSK with 4 scattering paths as an example, there are four bits $[s_0, s_1, s_2, s_3]$ that can be modulated as a symbol. According to Table 2.1, the first two bits $[s_0, s_1]$ are represented by the scattering paths with four specific transmission directions θ_1^t, θ_2^t, θ_3^t and θ_4^t. The remaining bits $[s_2, s_3]$ are represented by the conventional modulation scheme, i.e., QPSK.

Therefore, with the channel matrix $\mathbf{H}$, if the information [0, 0, 0, 0] is transmitted, the received signal y for the SSM system can be derived as

$$y = \sqrt{E}\mathbf{H}s + n = \sqrt{E}\left(\sum_{l=1}^{N_{\mathrm{ts}}} \beta_l \mathbf{a}_{\mathrm{r}}\left(\theta_l^r\right) \mathbf{a}_{\mathrm{t}}^H\left(\theta_l^t\right)\right) \mathbf{a}_{\mathrm{t}}\left(\theta_1^t\right) \frac{1+1j}{\sqrt{2}} + n = \sqrt{E}\beta_l \mathbf{a}_{\mathrm{r}}\left(\theta_1^r\right) \frac{1+1j}{\sqrt{2}} + n, \tag{2.5}$$

where E is the transmission power, and n is the noise at the receiver antenna elements. Then the receiver can apply the ML detection algorithm to decide which information bits are transmitted.

However, in the existing papers [16, 74–76], the channel model and system are designed for the 2-D linear array, which is not taking full advantages of the spatial domain resource in 3-D space. Meanwhile, the 2-D linear antenna array is not convenient for implementations because of its large physical size. Moreover, they assume that the beam of transmission signals in SSM systems is narrow enough and does not interfere with each other, which is different from the actual situation.

2.3 The Performance Analysis of IM Systems

The capacity and bit error performance are considered as two benchmarks to evaluate a modulation system. In this section, the channel capacity evaluation approaches for IM systems are first introduced. Afterwards, the analysis of the error performance is summarized.

2.3.1 The Channel Capacity of IM systems

Many published paper [42, 78–82] studied the IM system capacity with several types of fading channel, e.g. Rayleigh fading, Rice fading and Nakagami-m fading. For the IM systems working in different domains, such as the frequency-domain, and beamspace-domain, the calculation and analysis methods of channel capacities are mainly based on the Q function. The difference between analysis methods mainly lies in the different types of fading channels.

For the Rayleigh fading channel, the capacity of SM system was analysed in [83], which assumed the continuous-amplitude transmission signals following Gaussian distribution. The results indicated that the capacity of classic SM can achieve 6 bits/sec/Hz with 8 antenna elements. As the number of antennas at transceivers increases, the channel capacity was also increases [83]. The capacity of STBC under the Rayleigh fading channel was introduced in [81], which assumed the continuous-amplitude transmission signals following Gaussian distribution. The channel capacity reached nearly 6.5 bits/sec/Hz with 8×1 antenna arrays.

For the Rice and Nakagami-m fading channel, the channel capacities were analysed in [80] based on the same assumptions as [81]. In [84], the several types of channel capacities are classified, namely the continuous-input continuous-output memoryless channel (CCMC) capacity, which provided a generalised analytical framework for the IM modulation systems.

Unfortunately, in a real application scenario, the assumptions of CCMC are not strict. Therefore, the discrete-input continuous-output memoryless channel (DCMC) capacity of the SM systems was derived in [82], which specified the transmission symbols to select from finite discrete constellations. With the DCMC, the mutual information and channel capacity were analysed in [85], and the closed-form expressions for SM system based MISO channels were also derived. Meanwhile, with the frequency-selective fading channels, the authors in [86] and [87] analysed the channel capacity and the EE of the SM system for the uplink transmission.

2.3.2 The Error Performance of IM Systems

For IM schemes, the bit error performance is an important indicator for system evaluation. Many papers have been discussed the bit error probability (BEP) of IM systems over fading channels through analytical results and time-consuming Monte-Carlo simulations. Moreover, the union bound strategy is also a common tool for the BEP performance analysis.

Although the system structures of different IM schemes are diverse, there are similarities in the analysis approaches of BEP. An analytical framework to derive the BEP union upper bound was introduced in [88], which is designed for the SM MIMO wireless systems. For the generalised fading channels, the BEP analysis method of SM systems mentioned in [88] can be extended to the BEP analysis of most IM systems. The author separated the BEP of the MIMO based modulation system into three terms. The first part P_{sp} was the error probability that was only affected by the signal carried extra IM bits. The second part P_{sig} was the error probability that only related to the phase/amplitude modulation signals. The third part P_{joint} was the error probability that was jointly affected by the IM signals and the phase/amplitude modulation signals. Therefore, the union upper bound of the BEP P_{IM} can be represented as

$$P_{\text{IM}} \leq P_{\text{sp}} + P_{\text{sig}} + P_{\text{joint}}. \tag{2.6}$$

For a generic modulation scheme, P_{sig} is determined by the minimum Euclidean distance of amplitude/phase modulation constellation points. The P_{sp} depend on the modulus values of IM constellation points. However, it is challenging to obtain the BEP union upper bound with a closed-form expression under the specific channel model. Therefore, some approximation methods were proposed to derive the BEP or the PEP [89].

For the IM systems operating in spatial-domain, the bit error performance of the SM system with multiple active antennas was provided in [36], which analysed the BER performance with the optimal detection algorithm and low-complexity detection algorithm. Meanwhile, the closed-form expression of the BER for the GSM system was also derived in [41]. The authors in [34] exploited the DoF of the GSSK to improve the system performance, and derived the upper bound on GSSK's BER. The results indicated that the GSSK system outperformed the conventional V-BLAST MIMO system. For the fading channel with imperfect CSI, the authors in [35] proposed a novel performance analysis approach for the SM and SSK, which derived from the PEP expressions. With the linear space timer block decoder [37], the closed-form expression for union bound on the BER was derived. It can be seen from the simulation results that the STBC-SM outperforms the simple SM. Nevertheless, with the high modulation orders, the spatial multiplexing MIMO scheme may achieve a higher data rate than the SM scheme. This is because some transmitted antennas will be vacant when the extra bits are conveyed by the activated antennas, resulting in a loss of throughput, especially for a system with high SE [15]. The enhanced SM [90] was proposed to mitigate the loss of throughput in STBC-SM, which utilised different combinations of modulation orders and antenna activation patterns to improve the throughput. With the high modulation order, the results in [90, 91] indicated that the enhanced SM achieved better BER performance and higher throughput compared with the conventional SM system. For the quadrature SM (QSM) proposed in [92], the authors in [93] analysed the BEP with several modulation orders. The results indicated that the QSM always had better BER performance than SM. To analyse the QSM system performance with in-phase and quadrature imbalance, the analytical results in [94] indicated that BER performance was significantly reduced with the imbalance in-phase and quadrature. For the DSM system, the BER performance and the upper bound were derived in [69] with imperfect CSI. Meanwhile, the power allocation scheme [95], transmit-diversity [96] and channel correlation [97] are also important factors affecting the BER performance of SM systems.

For the frequency-domain IM schemes, the result in [55] first illustrated that the throughput and the bit error performance of OFDM-IM systems outperformed the conventional OFDM systems. The performance difference between OFDM-IM and classical OFDM is mainly caused by the frequency selectivity of the channel providing a higher diversity gain. For the GMM-OFDM-IM system, the BER analysis was obtained in [55]. Compared with the OFDM-IM scheme, the GMM-OFDM-IM can reduce the BER by a factor of 2 at the same SNR level. In [60], the closed-form ABEP expression of the OFDM-GIM system was derived. Compared with the conventional OFDM-IM scheme, the numerical results show that the proposed OFDM-GIM schemes exceed in the SE and BER performance, regardless of applying the QAM or PSK mapping scheme. With the GIM-OFDM schemes proposed in [60], the authors also compared the BER performance with the works in [98]. Two generalisation schemes can achieve better BER performance with the reduced overhead of sub-carriers. The performance analysis of the DM-OFDM system was introduced in [61, 62]. The BER results were analysed under the AWGN and frequency selective fading channels. For the AWGN channel, when the BER reached 10^{-4}, the SNR differential between the DM-OFDM system and the OFDM-IM system was around 6dB with the SE of 4 bits/s/Hz. For the frequency selective channel, when the BER reached 10^{-4} and the SE was set to 4 bits/s/Hz, the DM-OFDM can provide nearly 5 dB SNR gain compared with the OFDM-IM system. Furthermore, the BER performance of DM-OFDM and GDM-OFDM systems were compared in [62]. The GDM-OFDM brought 1-2 dB SNR gain, when the BER was equal to 10^{-4} and the SE was set to 3.33 bits/s/Hz.

For the time-domain IM schemes, the error performance of the SC-IM system was evaluated with different lengths of channel impulse response (CIR) [66, 65]. When the length of CIR was equal to 1, the SC-IM scheme had no benefit to the BER improvement of the conventional SC scheme. With the length of CIR increase, the advantages of the SC-IM scheme over the traditional SC scheme can be observed, which can achieve nearly 4 dB SNR gain [65]. With the novel constellation design, the error performance of the DM-SCIM scheme was analysed based on three constellation models with different Euclidean distance[67]. When the length of CIS was not equal to 1, the BER was inversely proportional to the minimum Euclidean distance of the constellation points. Meanwhile, the DM-SCIM scheme was prone to outperform the SC-IM scheme [67]. For the STIM scheme, the authors in [68] compared the BER performance between STIM and OFDM systems with the simulation results, where the STIM system achieved the better bit error performance. Applying the union upper bound technique, the BER performance of STSK and G-STSK schemes was introduced in [69]. And the error performance of multidimensional IM was provided in [71]. It is worth noting that the BER analysis in [67, 68, 70, 71] were based on the simulation results. Since time-domain IM schemes are usually modulated by combining the indices of multiple dimensions, the mapping schemes of information bits are complicated. In this case, it is difficult to derive the BER expressions by the common method as mentioned in [88].

For the beamspace-domain IM schemes, the authors in [16] introduced the BER performance with linear array antennas. The conditional PEP (CPEP) expressions were derived in [16]. Based on CPEP, the BER expression was analysed with the 32 elements linear array. The results indicated that the SSM scheme outperformed the maximum beamforming scheme with 12 scattering paths. When BER reached 10^{-6}, the SNR differential between SSM and maximum beamforming scheme was nearly 3 dB. Recently, combining the IRS and the SSM scheme, the IRS-aided SSM system performance was provided in [76]. The BER union bound expressions were derived, and validated by the simulation results. Applying the polarization domain resources, the BER of the polarized SSM system was presented in

[75]. Comparing the polarized SSM scheme with the maximum beamforming scheme, the polarized SSM can achieve 5 dB SNR gain when the BER reaches 10^{-6}.

2.4 Conclusion

In this chapter, the existing IM systems have been classified. The principles of various IM systems have been introduced. Meanwhile, the analysis approaches of the bit error performance and the channel capacity are summarized for the IM systems. It can be seen from the existing works that beamspace-domain IM systems are discussed based on the 2-D MIMO, and have not been extended to 3-D space.

With the development of the 3-D MIMO technology, the IM schemes should be considered in the 3-D space with large-scale antenna arrays, especially the beamspace-domain IM schemes. For the 3-D MIMO system, the extra DoF enables the AoA and AoD of the beam to be identified from both horizontal and vertical dimensions. At the receiver, compared with the linear array, the beam can be distinguished by two-dimensional characteristics. Specifically, if the 2-D linear array is applied, the beamspace-domain SSM scheme can only recognize the received beams in horizontal dimensional. Therein, if two beams have the same horizontal directions and different vertical directions, their scattering paths cannot be distinguished. In general, utilising the 3-D SSM can reduce the probability that beams cannot be distinguished in a single dimension to improve the system bit error performance. In existing works, the modelling of a 3-D MIMO based SSM system is not investigated. The planar array should be considered for the SSM to provide a DoF with elevation angles. Meanwhile, a generalised performance analysis framework of the 3-D SSM is missing in the literature.

Chapter 3

The System Design and Performance Analysis of 3-D SSM System

Overview

As a state-of-the-art mm-wave massive MIMO system, the SSM system is expanded to a 3-D SSM system by using large-scale planar antenna arrays, which makes full use of beamspace-domain resources to improve SE. In this chapter, the system model of 3-D SSM is introduced at first. Secondly, a whitening filter based optimum detection algorithm is proposed to detect the received symbols with correlated noises. Thirdly, for efficient evaluations, the closed-form expressions of union upper bound on the ABEP are derived for the 3-D SSM system and verified by Monte-Carlo simulations. Finally, the performance of the proposed 3-D SSM system is analysed under a typical indoor transmission environment.

3.1 Introduction

With the explosive growth of mobile data services and the continuously increasing popularisation of smart devices, SSM can improve both SE and EE in the B5G/6G era. In SSM systems, a part of information bits is conveyed through the traditional amplitude and phase modulation, while the other part of information bits is represented by the beam directions without additional energy consumption [16]. Therein, when IM utilises the same energy as the traditional modulation method, it can greatly increase the system throughput and improve the EE.

The authors in [16] introduced the SSM system. Therein, two information bit streams were transmitted simultaneously by selections of modulated symbol and scattering path. For the fast system performance evaluation and comparison, the diversity order of the SSM system was derived in [74]. To further exploit the polarisation domain resources in the SSM system, a polarized SSM system was proposed with a closed-form expression of its ABEP [75]. Using lens antenna arrays, Gao *et al.* designed a novel generalised beamspace modulation (GBM) system with limited RF-chains [99]. Recently, the digital transceivers for IM system were designed, and the corresponding performance bound has been discussed in [100]. The system performance of the GBM system under the circumstance was analysed and optimised in [101] by using a full digital precoder or hybrid precoder. The gradient ascent algorithm was proposed in [101] to optimise the full digital precoder for the GBM system to find the optimal hybrid precoding scheme. Numerical results indicated that the IM systems working in the beamspace-domain outperform those working in the spatial domain in terms of bit error performance [16, 102].

Most state-of-the-art works apply the linear antenna array for the SSM system, which only takes the azimuth angles to distinguish the direction of scattering paths. In order to take the full advantage of the beamspace-domain resources, besides the azimuth AoA and AoD, the elevation angles of AoA and AoD should be considered for the SSM system. Published works in the SSM system, e.g., [16, 74, 75] have assumed that receiver array vectors are orthogonal with each other. As a result, noises at the receiving RF-chains are assumed to be independently distributed. However, in a practical 3-D SSM system, due to the linear combination operated by phase shifters at the receiver, noises are correlated at the receiving RF-chains, which seriously affect the performance evaluation of 3-D SSM system.

In this chapter, a novel 3-D SSM system is proposed, which consider both vertical and horizontal dimension for the transmitted beams. Meanwhile, an optimal whitening filter based ML detection algorithm is designed for the 3-D SSM system. To evaluate the system performance, closed-form expressions of the ABEP union upper bound is derived and verified by Monte-Carlo simulations.

3.2 The System Design

Throughout this chapter, we use notations as follows.

Table 3.1 Notations and Variables

Notations	Definitions
N_{t}	Total number of antenna elements in the transmitting antenna array
N_{r}	Total number of antenna elements in the receiving antenna array
n_{t}	Indices of transmitting antenna elements in the uniform planar array (UPA)
n_{r}	Indices of receiving antenna elements in the UPA
$\mathbf{H}$	The MIMO channel matrix
N_{ts}	Total number of scattering path
n_{s}	The n_{s}-th scattering path
$\tilde{\mathbf{H}}_{n_{\mathrm{s}}}$	The channel matrix of the n_{s}-th scattering path
$\beta_{n_{\mathrm{s}}}$	The channel gain of the n_{s}-th scattering path
$\mathbf{x}$	The vector of transmitted signal
$\mathbf{n}_{\mathrm{a}}$	The vector of thermal noise at the receiving antenna array
$\mathbf{a}_{\mathrm{t,v},n_{\mathrm{s}}}$	Array vectors for the transmitting antenna array in each column
$\mathbf{a}_{\mathrm{t,h},n_{\mathrm{s}}}$	Array vectors for the transmitting antenna array in each row
$\mathbf{a}_{\mathrm{r,v},n_{\mathrm{s}}}$	Array vectors for the receiving antenna array in each column
$\mathbf{a}_{\mathrm{r,h},n_{\mathrm{s}}}$	Array vectors for the receiving antenna array in each row
K	Total number of the candidate scattering paths for selection
M	Modulation order
s_m	The transmitted symbol with the modulation index m
k	The order of candidate scattering path using at transmitter
k'	The order of selected scattering path using at receiver

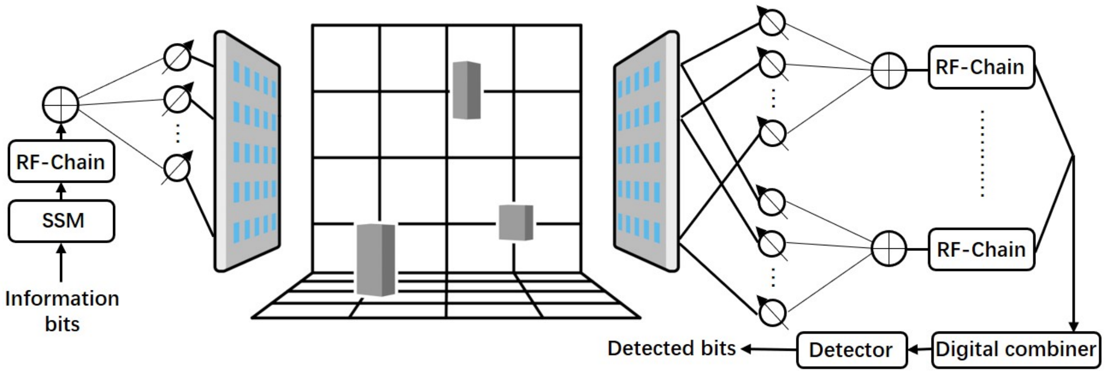

Fig. 3.1 The system model of 3-D SSM with a single RF-chain.

$\boldsymbol{\tau}_{\mathrm{t},k}$	Beam-steering vector at the transmitter for the k-th scattering path
$\boldsymbol{\tau}_{\mathrm{r},k'}$	Beam-steering vector at the receiver for the k'-th scattering path
$\tilde{\mathbf{n}}$	Effective additive Gaussian noise at each received RF-chain
$\mathbf{y}$	The receiving signal at received antenna array
$\mathbf{C}_{\text{noise}}$	Covariance matrix of the effective noise on each received RF-chain
$(\cdot)^{\mathrm{H}}$	Complex conjugate transpose operator
$\mathrm{conj}(\cdot)$	Complex conjugate operator
$(\cdot)^{-1}$	Square matrix inverse operator
$\otimes$	Kronecker product operator
$\|\cdot\|$	Absolute-value norm
$\mathrm{E}[\cdot]$	Expectation operator
$Q(\cdot)$	The Q-function

In a multipath propagation environment, the transmitted signal arrives at the receiver via multiple scattering paths. Equipped with the large-scale antenna array, the SSM system is capable of steering wireless signal to a specific selected scattering path. At the transmitter, information bits are divided into two streams, the first of which is conveyed by the selection of the scattering path, and the second is conveyed by the selection of transmitted symbol. The system model of the proposed 3-D SSM system is illustrated in Fig. 3.1.

3.2.1 The Modulation Scheme of 3-D SSM

The modulator of the 3-D SSM system is introduced first. We assume that a block of R bits are transmitted in each time slot. Following the system model of SSM in [16], the bit block is divided into two streams that are transmitted simultaneously, i.e., $R = R_K + R_M$, where R_K denotes the bits conveyed by selected scattering path, and R_M denotes the bits conveyed by selecting transmitted symbol.

We assume that the transmitter has only one RF-chain. For generating a single beam on the beamspace-domain, an array of phase shifters is applied to adjust the phase of each transmit antenna element in the planar array. With the unit power, the symbol s_m transmitted through the k-th scattering path, we obtain the transmitted symbol as

$$\mathbf{x} = s_m \boldsymbol{\tau}_{\mathrm{t},k}, \tag{3.1}$$

where $m \in 1,...,M$ is the index of the baseband modulation scheme with the modulation order M, $k \in \{1,2,...,K\}$ is the index of selected scattering path from K candidates, K is the total number of the candidate scattering paths for selection, $\boldsymbol{\tau}_{\mathrm{t},k}$ is the beam-steering vector at the transmitter for the k-th selected scattering path and can be computed by $\boldsymbol{\tau}_{\mathrm{t},k} = \left(\mathbf{a}_{\mathrm{t,v},k} \otimes \mathbf{a}_{\mathrm{t,h},k}\right)^{\mathrm{H}}$ [25]. $\mathbf{a}_{\mathrm{t,h},k}$ and $\mathbf{a}_{\mathrm{t,v},k}$ are array vectors in each row and column for the k-th scattering path at the transmitter, respectively. Additionally, $\boldsymbol{\tau}_{\mathrm{t},k}$ is assumed to be known at the transmitter. With an M-order signal constellation, we have $R_M = \log_2(M)$ bits. Then, the data rate of the proposed 3-D SSM system is given by $R = \log_2(KM)$. The constellation map of the 3-D SSM system is shown in Fig. 3.2. To clearly illustrate the modulation scheme in 3-D SSM, we give an example as follows.

Example 1. *The system with $K = 4$ scattering paths are considered, and PSK with $M = 4$ is used for the baseband modulation. When a random sequence needs to be sent, every $\log_2(KM) = 4$ bits $[i_0, i_1, i_2, i_3]$ are divided into a group. For the bits i_0, i_1, the information is determined by the selection of beam direction, and the information bits are conveyed by beam vectors $\boldsymbol{\tau}_{\mathrm{t},k}$. The other bits are modulated by amplitude and phase modulation scheme, i.e., 4PSK. Consequently, the mapping scheme of the 3-D SSM system with single RF-chain*

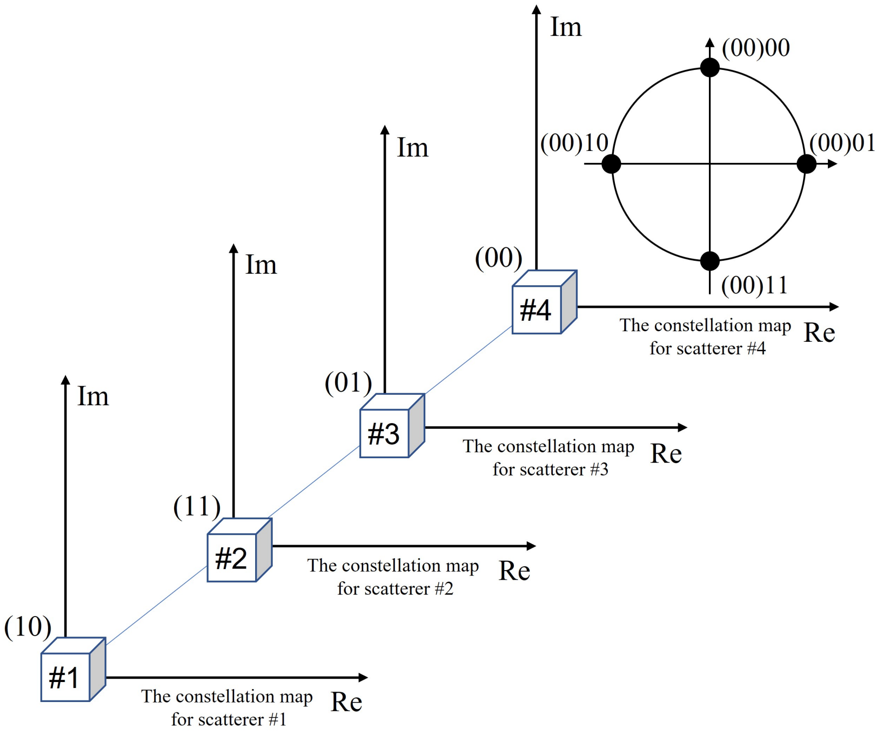

Fig. 3.2 The constellation mapping scheme of the 3-D SSM system.

is shown in Table. 3.2. Therefore, for the sequence $[1,0,1,1]$, *the transmitted signal* $\mathbf{x}$ *can be expressed as* $\mathbf{x} = \frac{-1+1j}{\sqrt{2}} \left(\mathbf{a}_{\mathrm{t,v},4} \otimes \mathbf{a}_{\mathrm{t,h},4}\right)^{\mathrm{H}}$.

3.2.2 3-D MIMO Scheme and Channel Model

The 3-D MIMO scheme and the channel model are introduced in this subsection. In the 3-D MIMO system, a $N_{\mathrm{t,v}} \times N_{\mathrm{t,h}}$ rectangular planar antenna array at the transmitter is applied to achieve the beamforming, where $N_{\mathrm{t,h}}$ and $N_{\mathrm{t,v}}$ denote the number of transmitting antenna elements in each row and column, respectively. Thus, the total number of transmitting antennas is $N_{\mathrm{t}} \triangleq N_{\mathrm{t,h}}N_{\mathrm{t,v}}$. At the receiver, a $N_{\mathrm{r,v}} \times N_{\mathrm{r,h}}$ planar antenna array is equipped, where $N_{\mathrm{r,h}}$ and $N_{\mathrm{r,v}}$ denote the number of receiving antenna elements in each row and column, respectively. The total number of receiving antennas is $N_{\mathrm{r}} \triangleq N_{\mathrm{r,h}}N_{\mathrm{r,v}}$. The 3-D narrowband discrete physical channel is adopted in the 3-D SSM system [6]. With this assumption, the

Table 3.2 The example of bits mapping scheme for the 3-D SSM system

Input information bits	The index of scatterers	Transmitted symbol
0000	♯1	$\frac{1+1j}{\sqrt{2}}$
0001	♯1	$\frac{1-1j}{\sqrt{2}}$
0011	♯1	$\frac{-1+1j}{\sqrt{2}}$
0010	♯1	$\frac{-1-1j}{\sqrt{2}}$
0100	♯2	$\frac{1+1j}{\sqrt{2}}$
0101	♯2	$\frac{1-1j}{\sqrt{2}}$
0111	♯2	$\frac{-1+1j}{\sqrt{2}}$
0110	♯2	$\frac{-1-1j}{\sqrt{2}}$
1100	♯3	$\frac{1+1j}{\sqrt{2}}$
1101	♯3	$\frac{1-1j}{\sqrt{2}}$
1111	♯3	$\frac{-1+1j}{\sqrt{2}}$
1110	♯3	$\frac{-1-1j}{\sqrt{2}}$
1000	♯4	$\frac{1+1j}{\sqrt{2}}$
1001	♯4	$\frac{1-1j}{\sqrt{2}}$
1011	♯4	$\frac{-1+1j}{\sqrt{2}}$
1010	♯4	$\frac{-1-1j}{\sqrt{2}}$

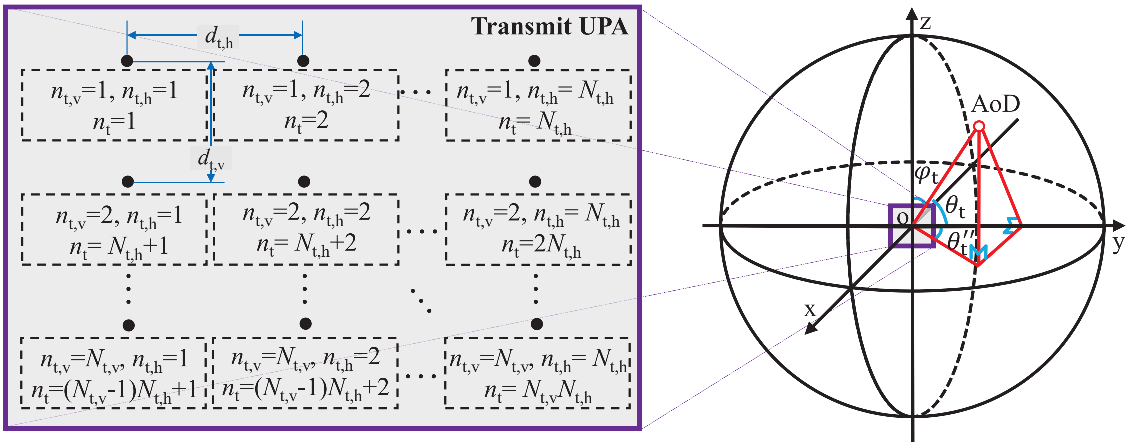

Fig. 3.3 The transmitting antenna indexes of the planar array.

3-D MIMO scheme can be expressed as

$$\mathbf{y} = \sqrt{\rho}\mathbf{H}\mathbf{x} + \mathbf{n}_{\mathrm{a}}, \tag{3.2}$$

where ρ denotes the SNR at the receiver, $\mathbf{H}$ is a N_{r} by N_{t} channel matrix, the transmitted signal $\mathbf{x}$ is a column vector with N_{t} elements, the received signal $\mathbf{y}$ is a vector with N_{r} elements, and the thermal noises $\mathbf{n}_{\mathrm{a}}$ is a vector with N_{r} elements.

By defining

$$n_{\mathrm{t}} = (n_{\mathrm{t,v}} - 1)N_{\mathrm{t,h}} + n_{\mathrm{t,h}}, \tag{3.3}$$

where $n_{\mathrm{t,v}} \in \{1,2,...,N_{\mathrm{t,v}}\}$, $n_{\mathrm{t,h}} \in \{1,2,...,N_{\mathrm{t,h}}\}$, indices of transmitting antenna in the transmitting UPA is defined, as shown in Fig. 3.3. Consequently, n_{r} can be defined as follows.

$$n_{\mathrm{r}} = (n_{\mathrm{r,v}} - 1)N_{\mathrm{r,h}} + n_{\mathrm{r,h}}, \tag{3.4}$$

where $n_{\mathrm{r,v}} \in \{1,2,...,N_{\mathrm{r,v}}\}$, $n_{\mathrm{r,h}} \in \{1,2,...,N_{\mathrm{r,h}}\}$. $\mathbf{H}(n_{\mathrm{r}}, n_{\mathrm{t}})$ is the channel coefficient from the transmitting antenna in the $n_{\mathrm{t,v}}$-th row and $n_{\mathrm{t,h}}$-th column of the rectangular array to the receiving antenna in the $n_{\mathrm{r,v}}$-th row and $n_{\mathrm{r,h}}$-th column of the rectangular array, $\mathbf{x}(n_{\mathrm{t}})$ denotes the signal transmitted from the transmit antenna at the $n_{\mathrm{t,v}}$-th row and the $n_{\mathrm{t,h}}$-th column of the rectangular transmitting array, $\mathbf{y}(n_{\mathrm{r}})$ denotes the received signal of the receiving antenna element at the $n_{\mathrm{r,v}}$-th row and $n_{\mathrm{r,h}}$-th column, and $\mathbf{n}_{\mathrm{a}}(n_{\mathrm{r}}) \sim \mathcal{CN}(0,1)$ is the thermal noise of the antenna element at the $n_{\mathrm{r,v}}$-th row and $n_{\mathrm{r,h}}$-th column. $\mathbf{n}_{\mathrm{a}}$ is assumed to be independent and identically distributed (i.i.d.).

In a multipath 3-D MIMO channel, the channel matrix $\mathbf{H}$, with N_{ts} multipath components, can be written as [103]

$$\mathbf{H} = \frac{1}{\sqrt{N_{\mathrm{t}}}} \sum_{n_{\mathrm{s}}=1}^{N_{\mathrm{ts}}} \beta_{n_{\mathrm{s}}} \tilde{\mathbf{H}}_{n_{\mathrm{s}}}, \tag{3.5}$$

where $\beta_{n_{\mathrm{s}}}$ is the channel gain of the n_{s}-th scattering path, N_{ts} is the total number of multi-path component, and $\tilde{\mathbf{H}}_{n_{\mathrm{s}}}$ denotes the channel matrix assuming that only the n_{s}-th scattering path exists in the environment,

$$\tilde{\mathbf{H}}_{n_{\mathrm{s}}}(n_{\mathrm{r}}, n_{\mathrm{t}}) = \mathbf{a}_{\mathrm{t,v},n_{\mathrm{s}}}(n_{\mathrm{t,v}}) \mathbf{a}_{\mathrm{t,h},n_{\mathrm{s}}}(n_{\mathrm{t,h}}) \mathbf{a}_{\mathrm{r,v},n_{\mathrm{s}}}(n_{\mathrm{r,v}}) \mathbf{a}_{\mathrm{r,h},n_{\mathrm{s}}}(n_{\mathrm{r,h}}), \tag{3.6}$$

and $\mathbf{a}_{\mathrm{t,v},n_{\mathrm{s}}}$, $\mathbf{a}_{\mathrm{t,h},n_{\mathrm{s}}}$, $\mathbf{a}_{\mathrm{r,v},n_{\mathrm{s}}}$ and $\mathbf{a}_{\mathrm{r,h},n_{\mathrm{s}}}$ are the array vectors for the transmitter array and receiver array.

As illustrated in Fig. 3.3, we assume that the planar receiving (or transmitting) antenna array is deployed in the yoz plane in the 3-D Cartesian coordinate system. The horizontal angle θ_{t} (or θ_{r}) is defined as the angle between AoA (or AoD) and the y-axis, and the vertical angle φ_{t} (or φ_{r}) is defined as the angle between AoA (or AoD) and the z-axis. Therein, the relationship between θ_{t} and θ_{t}'' is

$$\theta_{\mathrm{t}} = \arccos\left(\sin\left(\theta_{\mathrm{t}}''\right)\cos\left(\varphi_{\mathrm{t}}\right)\right). \tag{3.7}$$

Similarly, θ_{r} and θ_{r}'' follow the same relationship as θ_{t} and θ_{t}''.

Consequently, array vectors $\mathbf{a}_{\mathrm{t,v,}}, \mathbf{a}_{\mathrm{t,h,}}, \mathbf{a}_{\mathrm{r,v,}}, \mathbf{a}_{\mathrm{r,h,}}$ can be represented as [16]

$$\mathbf{a}_{\mathrm{t,v},n_{\mathrm{s}}} = \left[1, e^{j2\pi d_{\mathrm{t,v}} \cos\varphi_{\mathrm{t},n_{\mathrm{s}}}}, e^{j4\pi d_{\mathrm{t,v}} \cos\varphi_{\mathrm{t},n_{\mathrm{s}}}}, \ldots, e^{j2(N_{\mathrm{t,v}}-1)\pi d_{\mathrm{t,v}} \cos\varphi_{\mathrm{t},n_{\mathrm{s}}}}\right], \tag{3.8}$$

$$\mathbf{a}_{\mathrm{t,h},n_{\mathrm{s}}} = \left[1, e^{j2\pi d_{\mathrm{t,h}} \cos\theta_{\mathrm{t},n_{\mathrm{s}}}}, e^{j4\pi d_{\mathrm{t,h}} \cos\theta_{\mathrm{t},n_{\mathrm{s}}}}, \ldots, e^{j2(N_{\mathrm{t,h}}-1)\pi d_{\mathrm{t,h}} \cos\theta_{\mathrm{t},n_{\mathrm{s}}}}\right], \tag{3.9}$$

$$\mathbf{a}_{\mathrm{r,v},n_{\mathrm{s}}} = \left[1, e^{j2\pi d_{\mathrm{r,v}} \cos\varphi_{\mathrm{r},n_{\mathrm{s}}}}, e^{j4\pi d_{\mathrm{r,v}} \cos\varphi_{\mathrm{r},n_{\mathrm{s}}}}, \ldots, e^{j2(N_{\mathrm{r,v}}-1)\pi d_{\mathrm{r,v}} \cos\varphi_{\mathrm{r},n_{\mathrm{s}}}}\right], \tag{3.10}$$

$$\mathbf{a}_{\mathrm{r,h},n_{\mathrm{s}}} = \left[1, e^{j2\pi d_{\mathrm{r,h}} \cos\theta_{\mathrm{r},n_{\mathrm{s}}}}, e^{j4\pi d_{\mathrm{r,h}} \cos\theta_{\mathrm{r},n_{\mathrm{s}}}}, \ldots, e^{j2(N_{\mathrm{r,h}}-1)\pi d_{\mathrm{r,h}} \cos\theta_{\mathrm{r},n_{\mathrm{s}}}}\right], \tag{3.11}$$

and $d_{\mathrm{t,v}}$, $d_{\mathrm{t,h}}$, $d_{\mathrm{r,v}}$, $d_{\mathrm{r,h}}$ denote antenna interval distance in respect to the wavelength.

3.2.3 The Optimum Detector of 3-D SSM

By combining (3.1), (3.2), (3.5) and (3.6), the received signal can be obtained as

$$\mathbf{y} = \sqrt{\rho}\mathbf{H}\boldsymbol{\tau}_{\mathrm{t},k}s_m + \mathbf{n}_{\mathrm{a}}, \tag{3.12}$$

Assuming that the perfect CSI is obtained by receiver, the received signals are processed by the phase shifter network and are combined in K RF-chains. Every RF-chain is associated with a candidate scattering path. Therefore, the output of k'-th RF-chain can be represented by

$$\mathbf{z}(k') = \boldsymbol{\tau}_{\mathrm{r},k'}\mathbf{y} = \sqrt{\rho}s_m\boldsymbol{\tau}_{\mathrm{r},k'}\mathbf{H}\boldsymbol{\tau}_{\mathrm{t},k} + \boldsymbol{\tau}_{\mathrm{r},k'}\mathbf{n}_{\mathrm{a}}, \tag{3.13}$$

where $\boldsymbol{\tau}_{\mathrm{r},k'}$ is the beam-steering vector for the k'-th scattering path. $\boldsymbol{\tau}_{\mathrm{r},k'}$ can be derived as [104]

$$\boldsymbol{\tau}_{\mathrm{r},k'} = \mathrm{conj}\left(\mathbf{a}_{\mathrm{r,v},k'} \otimes \mathbf{a}_{\mathrm{r,h},k'}\right). \tag{3.14}$$

To simplify the derivation, we define

$$\ddot{\mathbf{H}}_{n_s}(k',k) = \boldsymbol{\tau}_{\mathrm{r},k'}\tilde{\mathbf{H}}_{n_{\mathrm{s}}}\boldsymbol{\tau}_{\mathrm{t},k}, \tag{3.15}$$

$$\widetilde{\mathbf{n}}(k') = \boldsymbol{\tau}_{\mathrm{r},k'}\mathbf{n}_{\mathrm{a}}, \tag{3.16}$$

then by substituting them into (3.5) and (3.13), we have

$$\mathbf{z} = \sqrt{\rho}s_m\frac{1}{\sqrt{N_{\mathrm{t}}}}\sum_{n_{\mathrm{s}}=1}^{N_{\mathrm{ts}}}\beta_{n_{\mathrm{s}}}\ddot{\mathbf{H}}_{n_s}(:,k) + \widetilde{\mathbf{n}}. \tag{3.17}$$

The equation (3.17) can be regarded as an effective $K \times K$ MIMO received signal for the SM system, where $\sum_{n_{\mathrm{s}}=1}^{N_{\mathrm{ts}}}\beta_{n_{\mathrm{s}}}\ddot{\mathbf{H}}_{n_s}$ is the effective MIMO transmission matrix, $\frac{s_m}{\sqrt{N_{\mathrm{t}}}}$ is the effective transmitted signal, the effective received signal from the k'-th scattering path is represented by $\mathbf{z}(k')$. The joint interference between mutual paths and channel noise leads to the fact that signals are not completely orthogonal. According to (3.16), $\widetilde{\mathbf{n}}$ is the effective additive Guassian noise but no longer white, even though $\mathbf{n}_{\mathrm{a}}$ is white.

With the effective additive noise $\widetilde{\mathbf{n}}$, before designing the optimum detection algorithm, the covariance matrix of $\widetilde{\mathbf{n}}$ needs to be quantified at first. The covariance matrix of the effective noise is denoted by a $K \times K$ matrix, i.e, $\mathbf{C}_{\text{noise}} = \mathrm{E}\left[\widetilde{\mathbf{n}}\widetilde{\mathbf{n}}^{\mathrm{H}}\right]$, and is calculated by the result given in Lemma 1.

Lemma 1 (General formula for solving elements in $\mathbf{C}_{\text{noise}}$)**.** *The covariance between noises at the $k^{(\mathrm{r})}$-th and the $k^{(\mathrm{r})'}$-th receiving RF-chains is computed by*

$$\begin{aligned}\mathbf{C}_{\text{noise}}(k',k'') = & \frac{1-\exp\left(jN_{\mathrm{r,v}}2\pi d_{\mathrm{r,v}}\left(\cos\varphi_{\mathrm{r},k'}-\cos\varphi_{\mathrm{r},k''}\right)\right)}{1-\exp\left(j2\pi d_{\mathrm{r,v}}\left(\cos\varphi_{\mathrm{r},k'}-\cos\varphi_{\mathrm{r},k''}\right)\right)} \\ & \times \frac{1-\exp\left(jN_{\mathrm{r,h}}2\pi d_{\mathrm{r,h}}\left(\cos\theta_{\mathrm{r},k'}-\cos\theta_{\mathrm{r},k''}\right)\right)}{1-\exp\left(j2\pi d_{\mathrm{r,h}}\left(\cos\theta_{\mathrm{r},k'}-\cos\theta_{\mathrm{r},k''}\right)\right)},\end{aligned} \tag{3.18}$$

where $k',k'' \in (1,2,...,K)$. So far, we have obtained $\mathbf{C}_{\text{noise}}$ of the 3-D SSM system.

Proof: Following the definition of $\mathbf{C}_{\text{noise}}$, we derive

$$\mathbf{C}_{\text{noise}} = \mathrm{E}\left[\widetilde{\mathbf{n}}\widetilde{\mathbf{n}}^{\mathrm{H}}\right]. \tag{3.19}$$

By substituting (3.16) into (3.19), we have

$$\mathbf{C}_{\text{noise}}(k',k'') = \mathrm{E}\left[\ \boldsymbol{\tau}_{\mathrm{r},k'}\mathbf{n}_{\mathrm{a}}\left(\boldsymbol{\tau}_{\mathrm{r},k''}\mathbf{n}_{\mathrm{a}}\right)^{\mathrm{H}}\ \right]. \tag{3.20}$$

Since the elements of $\mathbf{n}_{\mathrm{a}}$ are i.i.d. distributed, we can obtain

$$\mathrm{E}\left[\mathbf{n}_{\mathrm{a}}\mathbf{n}_{\mathrm{a}}^{\mathrm{H}}\right] = \mathbf{I}, \tag{3.21}$$

where $\mathbf{I}$ is the unit matrix. By substituting (3.21) into (3.20), we derive

$$\begin{aligned}\mathbf{C}_{\text{noise}}(k',k'') &= \mathrm{E}\left[\ \boldsymbol{\tau}_{\mathrm{r},k'}\left(\boldsymbol{\tau}_{\mathrm{r},k''}\right)^{\mathrm{H}}\ \right] \\ &= \mathrm{E}\left[\mathrm{conj}\left(\mathbf{a}_{\mathrm{r,v},k'}\otimes\mathbf{a}_{\mathrm{r,h},k'}\right)\left(\mathrm{conj}\left(\mathbf{a}_{\mathrm{r,v},k''}\otimes\mathbf{a}_{\mathrm{r,h},k''}\right)\right)^{\mathrm{H}}\right].\end{aligned} \tag{3.22}$$

Finally, we obtain (3.18) by substituting (3.10) and (3.11) into (3.22). ■

With the expression of $\mathbf{C}_{\text{noise}}$, the optimum detector of the 3-D SSM system can be obtained as shown in Theorem 3.1.

Theorem 3.1 (Optimum detection algorithm for 3-D SSM system)**.** *The optimum detection algorithm for the proposed 3-D SSM is given by*

$$[\hat{m},\hat{k}] = \arg\min_{m,k} \left\| \left(\mathbf{B}^{\mathrm{H}}\right)^{-1}\mathbf{z} - \frac{\sqrt{\rho}s_m}{\sqrt{N_{\mathrm{t}}}} \sum_{n_{\mathrm{s}}=1}^{N_{\mathrm{ts}}} \beta_{n_{\mathrm{s}}} \left(\mathbf{B}^{\mathrm{H}}\right)^{-1} \ddot{\mathbf{H}}_{n_s}(:,k) \right\|, \tag{3.23}$$

where matrix $\mathbf{B}$ *satisfies that* $\mathbf{C}_{\text{noise}} = \mathbf{B}\mathbf{B}^{\mathrm{H}}$*, and can be computed by Cholesky factorisation.*

Proof: Following equation (3.17), when (m,k) is transmitted, the distribution of $\mathbf{z}$ can be represented as

$$\mathscr{C}\mathscr{N}\left(\sqrt{\rho}s_m \frac{1}{\sqrt{N_{\mathrm{t}}}} \sum_{n_{\mathrm{s}}=1}^{N_{\mathrm{ts}}} \beta_{n_{\mathrm{s}}} \ddot{\mathbf{H}}_{n_s}(:,k), \mathbf{C}_{\text{noise}} \right). \tag{3.24}$$

For (k,m), the ML detection algorithm can be designed as

$$[\hat{k},\hat{m}] = \arg\min_{k,m}\{J(k,m)\}, \tag{3.25}$$

where $J(k,m)$ is defined by

$$J(k,m) = \left[\mathbf{z} - \frac{\sqrt{\rho}s_m}{\sqrt{N_{\mathrm{t}}}} \sum_{n_{\mathrm{s}}=1}^{N_{\mathrm{ts}}} \beta_{n_{\mathrm{s}}} \ddot{\mathbf{H}}_{n_s}(:,k) \right]^{\mathrm{H}} \mathbf{C}_{\text{noise}}^{-1} \left[\mathbf{z} - \frac{\sqrt{\rho}s_m}{\sqrt{N_{\mathrm{t}}}} \sum_{n_{\mathrm{s}}=1}^{N_{\mathrm{ts}}} \beta_{n_{\mathrm{s}}} \ddot{\mathbf{H}}_{n_s}(:,k) \right]. \tag{3.26}$$

Substituting $\mathbf{C}_{\text{noise}} = \mathbf{B}\mathbf{B}^{\mathrm{H}}$ into (3.26), we derive

$$J(k,m) = \left\| (\mathbf{B}^{\mathrm{H}})^{-1}\mathbf{z} - \frac{\sqrt{\rho}s_m}{\sqrt{N_{\mathrm{t}}}} \sum_{n_{\mathrm{s}}=1}^{N_{\mathrm{ts}}} \beta_{n_{\mathrm{s}}} (\mathbf{B}^{\mathrm{H}})^{-1} \ddot{\mathbf{H}}_{n_s}(:,k) \right\|. \tag{3.27}$$

By substituting (3.27) into (3.25), the equation (3.23) can be obtained. ■

Equation (3.23) can be considered as a whitening filter based on the detection algorithm, since $\left(\mathbf{B}^{\mathrm{H}}\right)^{-1}\widetilde{\mathbf{n}}$ is AWGN. To detect the received signal, ML detection can be applied to decide which scattering path is selected and what symbol is transmitted.

3.3 ABEP Performance Analysis

To analyse the bit error performance of 3-D SSM system, ABEP is required as the metric to evaluate the system. The closed-form union upper bound expression of ABEP is derived in this section. The APEP expressions is obtained at first. [105]. Based on the APEP expressions, the ABEP closed-form expression can be derived with the union upper bound technique.

The ABEP union bound expression can be calculated by [105]

$$\mathrm{ABEP} \leq \sum_{k=1}^{K}\sum_{m=1}^{M}\sum_{\hat{k}=1}^{K}\sum_{\hat{m}=1}^{M}\frac{1}{MK}\frac{N(k,m\rightarrow\hat{k},\hat{m})}{\log_2(MK)}\mathrm{P}\left(k,m\rightarrow\hat{k},\hat{m}\right), \tag{3.28}$$

where $N(k,m\rightarrow\hat{k},\hat{m}) = N_{\mathrm{k}}(k\rightarrow\hat{k})+N_{\mathrm{m}}(m\rightarrow\hat{m})$ denotes the number of erroneous bits when k, s_m are transmitted but $\hat{k}, s_{\hat{m}}$ are received. $N_{\mathrm{k}}(k\rightarrow\hat{k})$ is the number of wrong bits caused by $k\neq\hat{k}$, and $N_{\mathrm{m}}(m\rightarrow\hat{m})$ is the number of wrong bits caused by $m\neq\hat{m}$. $\mathrm{P}(k,m\rightarrow\hat{k},\hat{m})$ is the APEP of the proposed 3-D SSM system, and is computed by

$$\begin{aligned}\mathrm{P}\left(k,m\rightarrow\hat{k},\hat{m}|\beta_1,\beta_2,\cdots,\beta_{N_{\mathrm{ts}}}\right) = \mathrm{P}\Bigg(&\left\|\left(\mathbf{B}^{\mathrm{H}}\right)^{-1}\mathbf{z}-\sqrt{\rho}s_m\frac{1}{\sqrt{N_{\mathrm{t}}}}\sum_{n_{\mathrm{s}}=1}^{N_{\mathrm{ts}}}\beta_{n_{\mathrm{s}}}\left(\mathbf{B}^{\mathrm{H}}\right)^{-1}\ddot{\mathbf{H}}_{n_s}(:,k)\right\| \\ &\geq\left\|\left(\mathbf{B}^{\mathrm{H}}\right)^{-1}\mathbf{z}-\sqrt{\rho}s_{\hat{m}}\frac{1}{\sqrt{N_{\mathrm{t}}}}\sum_{n_{\mathrm{s}}=1}^{N_{\mathrm{ts}}}\beta_{n_{\mathrm{s}}}\left(\mathbf{B}^{\mathrm{H}}\right)^{-1}\ddot{\mathbf{H}}_{n_s}(:,\hat{k})\right\|\Bigg),\end{aligned} \tag{3.29}$$

when the symbol s_m is transmitted by the k-th scattering path. In order to explain how to get $N(k,m\rightarrow\hat{k},\hat{m})$, we give an example as follows.

Example 2. *With index of scattering path* $K = 4$, *and QPSK is used for baseband modulation, the system can provide a total of 16 possible combinations of* k *and* s_m. *If the transmitted symbol with the index of the transmit scattering path* $k = 1$ *and the index of the transmitted* *symbol* $m=3$*, the receiver detects the index of scattering path as* $\hat{k}=2$ *and the index of the transmitted symbol as* $\hat{m}=3$*. According to the Table 3.1, the transmitted bits are* 0010*, and the received bits are* 0110*. It means that the received bits have 1 bit error after demodulation. Therefore, the* $N(k,m\rightarrow\hat{k},\hat{m})$ *is equal to 1 in this case.*

If PSK signal constellation is used in the proposed 3-D SSM system, the computation of union upper bound on the ABEP can be further simplified as in Theorem 2.

Theorem 3.2 (Simplified union upper bound on the ABEP for PSK signal constellation)**.** *When the K candidate scattering paths are randomly chosen from all* N_{ts} *existing scattering paths, and the indices of scattering path is randomly allocated, the ABEP is upper bounded by*

$$ABEP \leq \mathrm{ABEP}_{k=\hat{k}} + \mathrm{ABEP}_{k\neq\hat{k}}, \tag{3.30}$$

where

$$\mathrm{ABEP}_{k=\hat{k}} = \frac{1}{\log_2(MK)} \sum_{\hat{m}=2:2:M} N_{\mathrm{m}}(1\rightarrow\hat{m})\mathrm{P}(1,1\rightarrow 1,\hat{m}), \tag{3.31}$$

$$\begin{aligned}\mathrm{ABEP}_{k\neq\hat{k}} =& \frac{1}{M\log_2(MK)} \sum_{\hat{m}=1}^{M}\sum_{m=1}^{M} \mathrm{P}(1,m\rightarrow 2,\hat{m}) \\ &\times \left((K-1)N_{\mathrm{m}}(m\rightarrow\hat{m}) + \frac{\log_2(K)K}{2}\right).\end{aligned} \tag{3.32}$$

Proof: Following equation (3.28), we can divide ABEP into two different parts, which associate to $k=\hat{k}$ and $k\neq\hat{k}$, respectively. Then the equation (3.28) can be rewritten as

$$\begin{aligned} ABEP \leq & \underbrace{\frac{1}{MK\log_2(MK)} \sum_{m=1}^{M}\sum_{\hat{m}=1}^{M}\sum_{k=1}^{K} N_{\mathrm{m}}(m\rightarrow\hat{m})\mathrm{P}\left(k,m\rightarrow\hat{k},\hat{m}\right)}_{ABEP_{k=\hat{k}}} \\ & + \underbrace{\frac{1}{MK\log_2(MK)} \sum_{\hat{m}=1}^{M}\sum_{m=1}^{M}\sum_{k=1}^{K}\sum_{\hat{k}\neq k=1}^{K} N\left(k,m\rightarrow\hat{k},\hat{m}\right)\mathrm{P}\left(k,m\rightarrow\hat{k},\hat{m}\right)}_{ABEP_{k\neq\hat{k}}}. \end{aligned} \tag{3.33}$$

Firstly, we prove (3.31) as follows. If $k=\hat{k}$, the detection of beam vector directions is correct. On this premise, the error of demodulation bits is only caused by $m\neq\hat{m}$. Because the probability of selecting each scattering path is equal and the β_{N_s} follows i.i.d. complex Gaussian distribution, $\mathrm{P}(k,m \to k,\hat{m})$ for any value of $k = 2,3,...,K$ is equal to $\mathrm{P}(1,m \to 1,\hat{m})$. By substituting $\mathrm{P}(k,m \to k,\hat{m}) = \mathrm{P}(1,m \to 1,\hat{m})$ into (3.33), we obtain

$$ABEP_{k=\hat{k}} = \frac{1}{M\log_2(MK)} \sum_{m=1}^{M} \sum_{\hat{m}=1}^{M} N_{\mathrm{m}}(m \to \hat{m})\mathrm{P}(1,m \to 1,\hat{m}). \tag{3.34}$$

Since the symmetrical properties of PSK constellation, the ABEP for $m = 1$ is equal to that for $m = 2,3,...,M$. Therefore, we can derive

$$ABEP_{k=\hat{k}} = \frac{1}{\log_2(MK)} \sum_{\hat{m}=2}^{M} N_{\mathrm{m}}(1 \to \hat{m})\mathrm{P}(1,1 \to 1,\hat{m}). \tag{3.35}$$

According to [106, Eq. (10)], a tighter upper bound on $\mathrm{ABEP}_{k=\hat{k}}$ is then given by (3.31).

Then, the equation (3.32) is proved as follows. If $k \neq \hat{k}$, the detected beam vector directions is incorrect. Because the probability of selecting each scattering path is equal, it can be assumed that the signal transmits to the receiver through the scattering path with index $k = 1$. Therefore, from (3.33), we derive

$$\mathrm{ABEP}_{k\neq\hat{k}} = \frac{1}{M\log_2(MK)} \sum_{\hat{m}=1}^{M} \sum_{m=1}^{M} \sum_{\hat{k}=2}^{K} N\left(1,m \to \hat{k},\hat{m}\right) \mathrm{P}\left(1,m \to \hat{k},\hat{m}\right). \tag{3.36}$$

Moreover, due to the same reason, $\mathrm{P}\left(1,m \to \hat{k},\hat{m}\right) = \mathrm{P}\big(1,m \to 2,\hat{m}\big)$ for $k \neq \hat{k}$, and thus

$$\mathrm{ABEP}_{k\neq\hat{k}} = \frac{1}{M\log_2(MK)} \sum_{\hat{m}=1}^{M} \sum_{m=1}^{M} \mathrm{P}\big(1,m \to 2,\hat{m}\big) \sum_{\hat{k}=2}^{K} N\left(1,m \to \hat{k},\hat{m}\right). \tag{3.37}$$

By substituting $\sum_{\hat{k}=2}^{K} N_{\mathrm{k}}\left(1 \to \hat{k}\right) = \frac{\log_2(K)K}{2}$ [97, Eq.(10)] and $\sum_{\hat{k}=2}^{K} N_{\mathrm{m}}(m \to \hat{m}) = (K-1)N_{\mathrm{m}}(m \to \hat{m})$ into (3.37), we obtain (3.32). ■

Following (3.31) and (3.32), if the closed-form expressions of $\mathrm{P}\big(k,m \to k,\hat{m}\big)$ and $\mathrm{P}\big(k,m \to \hat{k},\hat{m}\big)$ are obtained, the closed-form expression of ABEP can be derived. The calculation methods of $\mathrm{P}\big(k,m \to k,\hat{m}\big)$ and $\mathrm{P}\big(k,m \to \hat{k},\hat{m}\big)$ are derived as (3.38) and (3.42) in the following Lemma 2, respectively.

Lemma 2 (Closed-form expressions of APEP)**.** *With N_{ts} scattering paths, the closed-form expression of the APEP is calculated as follows.*

For $k = \hat{k}$,

$$\mathrm{P}\big(k,m \to k,\hat{m}\big) \approx \frac{\prod_{n_s=1}^{N_{\mathrm{ts}}} \mathrm{L}_{n_{\mathrm{s}}}}{12} + \frac{\prod_{n_s=1}^{N_{\mathrm{ts}}} \mathrm{M}_{n_{\mathrm{s}}}}{4}, \tag{3.38}$$

where

$$\mathrm{L}_{n_{\mathrm{s}}} = \left(1 + \frac{\rho}{4N_{\mathrm{ts}}N_{\mathrm{t}}}\lambda_{n_{\mathrm{s}}}\right)^{-1}, \tag{3.39}$$

$$\mathrm{M}_{n_{\mathrm{s}}} = \left(1 + \frac{\rho}{3N_{\mathrm{ts}}N_{\mathrm{t}}}\lambda_{n_{\mathrm{s}}}\right)^{-1}, \tag{3.40}$$

$\lambda_{n_{\mathrm{s}}}$ is the n_{s}-th eigenvalue of $\mathbf{A}^{\mathrm{H}}\mathbf{C}_{\mathrm{noise}}^{-1}\mathbf{A}$,

$$\mathbf{A}(:,n_{\mathrm{s}}) = \ddot{\mathbf{H}}_{n_s}(:,k)\left(s_m - s_{\hat{m}}\right). \tag{3.41}$$

For $k \neq \hat{k}$,

$$\mathrm{P}\left(k,m \to \hat{k},\hat{m}\right) \approx \frac{\prod_{n_s=1}^{N_{\mathrm{ts}}} \mathrm{L}'_{n_{\mathrm{s}}}}{12} + \frac{\prod_{n_s=1}^{N_{\mathrm{ts}}} \mathrm{M}'_{n_{\mathrm{s}}}}{4}, \tag{3.42}$$

where

$$\mathrm{L}'_{n_{\mathrm{s}}} = \left(1 + \frac{\rho}{4N_{\mathrm{ts}}N_{\mathrm{t}}}\lambda'_{n_{\mathrm{s}}}\right)^{-1}, \tag{3.43}$$

$$\mathrm{M}'_{n_{\mathrm{s}}} = \left(1 + \frac{\rho}{3N_{\mathrm{ts}}N_{\mathrm{t}}}\lambda'_{n_{\mathrm{s}}}\right)^{-1}, \tag{3.44}$$

and $\lambda'_{n_{\mathrm{s}}}$ is the n_{s}-th eigenvalue of $\mathbf{A}'^{\mathrm{H}}\mathbf{C}_{\mathrm{noise}}^{-1}\mathbf{A}'$,

$$\mathbf{A}'(:,k) = s_m\ddot{\mathbf{H}}_{n_{\mathrm{s}}}(:,k) - s_{\hat{m}}\ddot{\mathbf{H}}_{n_{\mathrm{s}}}(:,\hat{k}). \tag{3.45}$$

Proof: From (3.29), when $k = \hat{k}$, $\mathrm{P}(k,m \to k,\hat{m})$ can be calculated based on the Q function.

$$\begin{aligned}\mathrm{P}(k,m \to k,\hat{m}) &= \mathrm{E}_{\beta_{n_\mathrm{s}}}\left[Q\left(\sqrt{\frac{\rho}{2N_\mathrm{t}}\sum_{n_s=1}^{N_\mathrm{ts}}\left\|\begin{array}{c}\beta_{n_\mathrm{s}}s_m\left(\mathbf{B}^\mathrm{H}\right)^{-1}\ddot{\mathbf{H}}_{n_s}(:,k)\\ -\beta_{n_\mathrm{s}}s_{\hat{m}}\left(\mathbf{B}^\mathrm{H}\right)^{-1}\ddot{\mathbf{H}}_{n_s}(:,k)\end{array}\right\|}\right)\right]\\ &= \mathrm{E}_{\beta_{n_\mathrm{s}}}\left[Q\left(\sqrt{\frac{\rho}{2N_\mathrm{t}}\sum_{n_s=1}^{N_\mathrm{ts}}\left\|\beta_{n_\mathrm{s}}(\mathbf{B}^\mathrm{H})^{-1}\ddot{\mathbf{H}}_{n_s}(:,k)\left(s_m - s_{\hat{m}}\right)\right\|}\right)\right].\end{aligned} \tag{3.46}$$

The variable in Q function can be simplified as

$$\left(\mathbf{B}^\mathrm{H}\right)^{-1}\ddot{\mathbf{H}}_{n_\mathrm{s}}(:,k)\left(s_m - s_{\hat{m}}\right) = \left(\mathbf{B}^\mathrm{H}\right)^{-1}\mathbf{A}(:,k), \tag{3.47}$$

where $\mathbf{A}$ is defined in (3.41). With the specific $k = n_s$, then we derive

$$\sum_{n_s=1}^{N_\mathrm{ts}}\left\|\beta_{n_\mathrm{s}}\left(\mathbf{B}^\mathrm{H}\right)^{-1}\mathbf{A}\left(:,n_\mathrm{s}\right)\right\| = \boldsymbol{\beta}^\mathrm{H}\mathbf{A}^\mathrm{H}\mathbf{B}^{-1}\left(\mathbf{B}^\mathrm{H}\right)^{-1}\mathbf{A}\boldsymbol{\beta} = \boldsymbol{\beta}^\mathrm{H}\mathbf{A}^\mathrm{H}\mathbf{C}_\mathrm{noise}^{-1}\mathbf{A}\boldsymbol{\beta}, \tag{3.48}$$

where

$$\boldsymbol{\beta} = [\beta_1, \beta_2, ..., \beta_{N_\mathrm{ts}}]^\mathrm{H}. \tag{3.49}$$

By utilising the eigenvalue decomposition on $\mathbf{A}^\mathrm{H}\mathbf{C}_\mathrm{noise}^{-1}\mathbf{A}$, (3.48) can be further simplified as

$$\boldsymbol{\beta}^\mathrm{H}\mathbf{A}^\mathrm{H}\mathbf{C}_\mathrm{noise}^{-1}\mathbf{A}\boldsymbol{\beta} = \boldsymbol{\beta}^\mathrm{H}\mathbf{U}\boldsymbol{\Lambda}\mathbf{U}^\mathrm{H}\boldsymbol{\beta}. \tag{3.50}$$

Since $\boldsymbol{\beta}$ follows i.i.d. complex Gaussian distribution, and $\mathbf{U}$ is the unitary matrix. Let $\boldsymbol{\xi}^\mathrm{H}$=$\boldsymbol{\beta}^\mathrm{H}\mathbf{U}$ and $\boldsymbol{\xi}$=$\boldsymbol{\beta}\mathbf{U}^\mathrm{H}$, which still follows i.i.d. complex Gaussian distribution. The singular value matrix $\boldsymbol{\Lambda}$ is expressed as

$$\boldsymbol{\Lambda} = \begin{bmatrix}\lambda_1 & 0 & 0\\ 0 & \ddots & 0\\ 0 & 0 & \lambda_{N_\mathrm{ts}}\end{bmatrix}. \tag{3.51}$$

By substituting (3.50) into (3.46), we derive

$$\mathrm{P}\left(k,m \to k,\hat{m}\right) = \mathrm{E}_{\beta_{n_\mathrm{s}}}\left[Q\left(\sqrt{\frac{\rho}{2N_\mathrm{t}}\sum_{n_s=1}^{N_\mathrm{ts}} \|\xi_{n_s}\|\,\lambda_{n_s}}\right)\right], \tag{3.52}$$

where ξ_{n_s} are elements of matrix $\boldsymbol{\xi}$. To get a concise numerical result, the pure exponential approximation [107] of Q function is applied to obtain the closed-form APEP expression. The pure exponential approximation of Q function is

$$Q\left(x\right) \approx \frac{1}{12}e^{-\frac{x^2}{2}} + \frac{1}{4}e^{-\frac{2}{3}x^2}. \tag{3.53}$$

Since ξ_{n_s} follows complex Gaussian distribution, we have

$$\begin{aligned}\mathrm{E}_\xi\left[\frac{1}{12}e^{-\frac{\rho}{4N_\mathrm{t}}\sum\limits_{n_s=1}^{N_\mathrm{ts}}\|\xi_{n_s}\|\lambda_{n_s}}\right] =& \frac{1}{12}\int\limits_0^{+\infty}\int\limits_0^{\|\xi_1\|}\cdots\int\limits_0^{\|\xi_{N_\mathrm{ts}-1}\|} \\ &\times e^{-\frac{\frac{\rho}{N_\mathrm{t}}\sum\limits_{n_s=1}^{N_\mathrm{ts}}\|\xi_{n_s}\|\lambda_{n_s}}{4}} e^{-\sum\limits_{n_s=1}^{N_\mathrm{ts}}\|\xi_{n_s}\|}\mathrm{d}\|\xi_{N_\mathrm{ts}}\|\cdots\mathrm{d}\|\xi_2\|\,\mathrm{d}\|\xi_1\| \\ =& \frac{\prod\limits_{n_s=1}^{N_\mathrm{ts}}\left(1+\frac{\rho}{4N_\mathrm{ts}N_\mathrm{t}}\lambda_{n_\mathrm{s}}\right)^{-1}}{12}.\end{aligned} \tag{3.54}$$

Following the similar approach, we have

$$\mathrm{E}_\xi\left[\frac{1}{4}e^{-\frac{\rho}{3N_\mathrm{t}}\sum\limits_{n_s=1}^{N_\mathrm{ts}}\|\xi_{n_s}\|\lambda_{n_s}}\right] = \frac{\prod\limits_{n_s=1}^{N_\mathrm{ts}}\left(1+\frac{\rho}{3N_\mathrm{ts}N_\mathrm{t}}\lambda_{n_\mathrm{s}}\right)^{-1}}{4}. \tag{3.55}$$

Combining (3.53), (3.54) and (3.55), then substituting them into (3.52), we obtain the closed-form expression of $\mathrm{P}\left(k,m \to k,\hat{m}\right)$ as (3.38). By defining $\mathbf{A}'$ in (3.45), and following the similar procedure of deriving (3.38), $\mathrm{P}(k,m \to \hat{k},\hat{m})$ can be computed by Q function as (3.42).

■

Therefore, the closed-form expression of ABEP is obtained by substituting (3.38) and (3.42) into (3.30). When the K candidate scattering paths are not randomly chosen, the ABEP can be obtained by substituting (3.38) and (3.42) into (3.28).

3.4 Numerical Results and Discussions

In this section, we validate numerical results of ABEP in 3-D SSM system under a typical indoor propagation environment. According to the results in [108], a generalised transmission environment usually has 5-12 relatively clear propagation paths in the massive MIMO system, which is sufficient for the application of 3-D SSM system. The ray-tracing algorithm is applied to obtain the channel impulse response [109]. Firstly, the ABEP analytical results are verified by the Monte-Carlo simulations. Secondly, the ABEP performance is compared between the 3-D SSM system and the 2-D SSM system. Then, the effects of the number of total scattering path N_{ts} and the candidate scattering path K on the ABEP performance are analysed.

The typical indoor scattering environment under consideration is illustrated in Fig. 3.4, where W_{i}, L_{i}, H_{i} are used to represent the width, length and height of the room. The positions of BS and UE are plotted as gray rectangles in Fig. 3.4. Two planar arrays are applied for the BS and UE. We design three typical indoor propagation environments, the parameters of which are shown in Table I as case 1, case 2 and case 3 to analysis the ABEP performance. x, y, z are the coordinate axes along W_{i}, L_{i}, H_{i}, respectively, and the unit is meter.

In the typical indoor scattering environment, signals are mainly transmitted from five different scattering paths, which have one non-line-of-sight (NLOS) paths and four first order reflection paths as red lines shown in Fig. 3.4. The candidate scattering paths, randomly chosen from above-mentioned five scattering paths, will be used to convey information bits, i.e., $N_{\mathrm{ts}} = 5$ and $K = 2$.

The planar arrays with 4×4, 6×6, and 8×8 antennas are considered at both transmitter and receiver. M-PSK signal constellation is applied as a benchmark in the analysis. The distance between each antenna element is half wavelength. For the 2-D SSM system, the

Table 3.3 Channel parameters

	Case 1	Case 2	Case 3
W_i	5 m	10 m	10 m
L_i	5 m	10 m	10 m
H_i	3 m	3 m	3 m
BS $(x_\mathrm{B}, y_\mathrm{B}, h_\mathrm{B})$	(4, 4, 1.2)	(5, 6, 1.2)	(9, 9, 1.2)
UE $(x_\mathrm{U}, y_\mathrm{U}, h_\mathrm{U})$	(2, 2, 1.2)	(2, 2, 1.2)	(2, 2, 1.2)

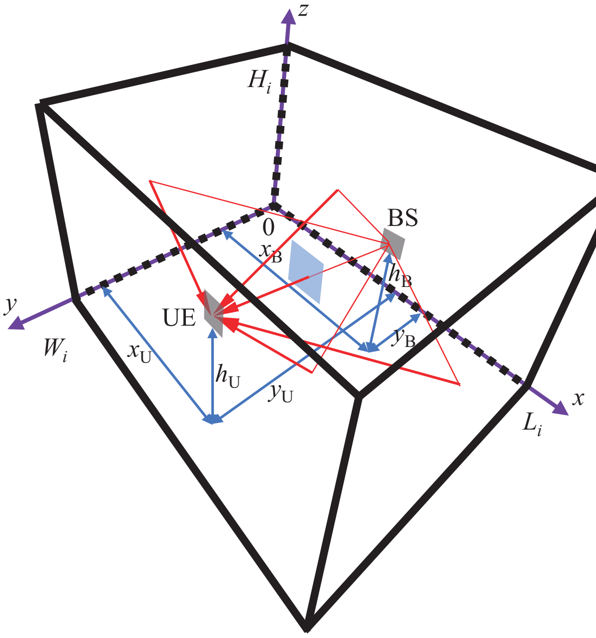

Fig. 3.4 A typical indoor propagation environment. The scattering paths are shown as the red lines.

linear array distinguishes the incoming scattering path according to a single dimension in the beamspace-domain, i.e., φ_t and φ_r.

3.4.1 The ABEP Performance under Indoor Environments

With the different modulation order M, the ABEP union upper bound is verified under the given indoor environment with $N_\mathrm{ts} = 5$ deterministic scattering paths at first. $K = 2$ scattering paths are selected to transmit the information bits. The 4×4 planar arrays are utilised at the transceivers under the typical indoor propagation environment case 2. As shown in

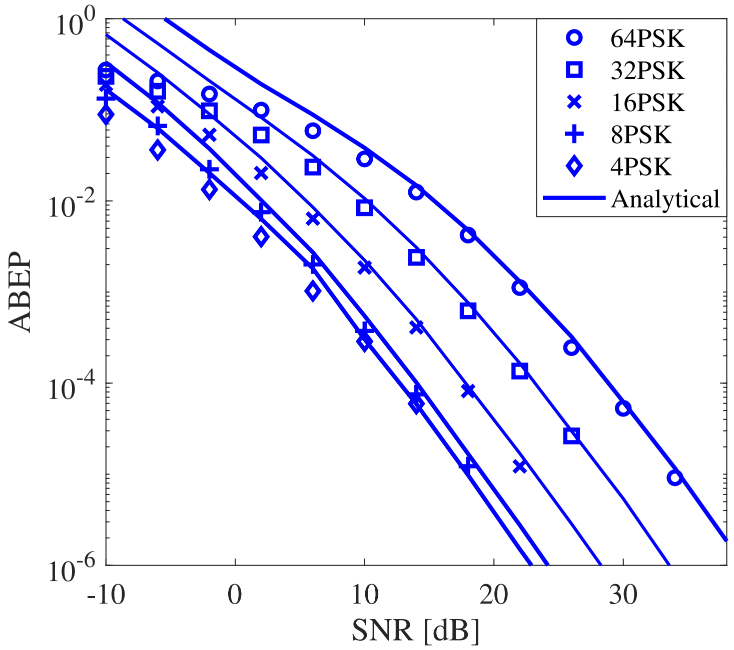

Fig. 3.5 The ABEP of 3-D SSM systems under the indoor environment case 2 with 4 × 4 antenna arrays. The analytical and simulation results are represented by solid lines and markers, respectively.

Fig. 3.5, the simulation results are matched with the closed-form ABEP union upper bound. Meanwhile, the ABEP performance of 3-D SSM systems reduce with the modulation order M decrease. When the modulation order M equal to 4 and 8, the ABEP performance are similar. Since a lower modulation order is applied, the main reason of generating detection error is no longer the identification error of the conventional modulation symbol, but the undistinguishable scattering paths.

In Fig. 3.6 and Fig. 3.7, it can be observed that the ABEP performance are significantly enhanced with a large size of antenna array. Comparing 4 × 4 and 8 × 8 planar arrays in Fig. 3.6, SNR difference is about 12 dB, when the ABEP reaches 10^{-5}. Due to the lack of DoF in the 2-D SSM system, it can only identify different beams in the horizontal direction. Beams with the same horizontal direction cannot be resolved even though their vertical directions are different, which leads to a decline in 2-D system performance. Additionally, it can be seen that the SNR gap between ABEPs of the 2-D with 16 × 1 and 3-D SSM with 4 × 4 is nearly 4.2 dB in case 2 and above more than 20 dB in case 3. The results indicate that

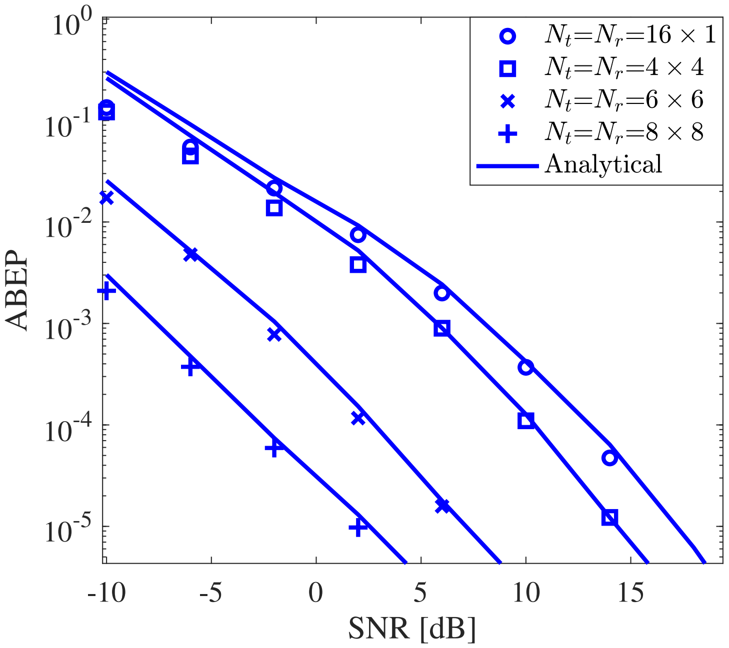

Fig. 3.6 The ABEP of 3-D SSM systems under the indoor environment case 2. The analytical and simulation results are represented by solid lines and markers, respectively.

the ABEP performance of 2-D SSM system is significantly degraded by the indiscernible scattering paths.

3.4.2 Impacts of N_{ts} and K on ABEP

For the 3-D SSM systems, the performance of ABEP is not only affected by the modulation order M, but also the total number of candidate scattering paths N_{ts}. In this subsection, the effect of K and N_{ts} on the ABEP will be discussed.

Firstly, the ABEP performance with different value of N_{ts} is analysed. For the typical indoor environment case 3, the 8-PSK modulation scheme and 6 × 6 antenna array are applied. As shown in Fig. 3.8, when the number of candidate scattering paths is decrease, the ABEP performance of the 3-D SSM system is also degraded. The improvement of ABEP performance with a large value of N_{ts} is caused by more RF-chains applied at the receiver. Since there are more candidate RF-chains, it is beneficial to reduce the influence of channel

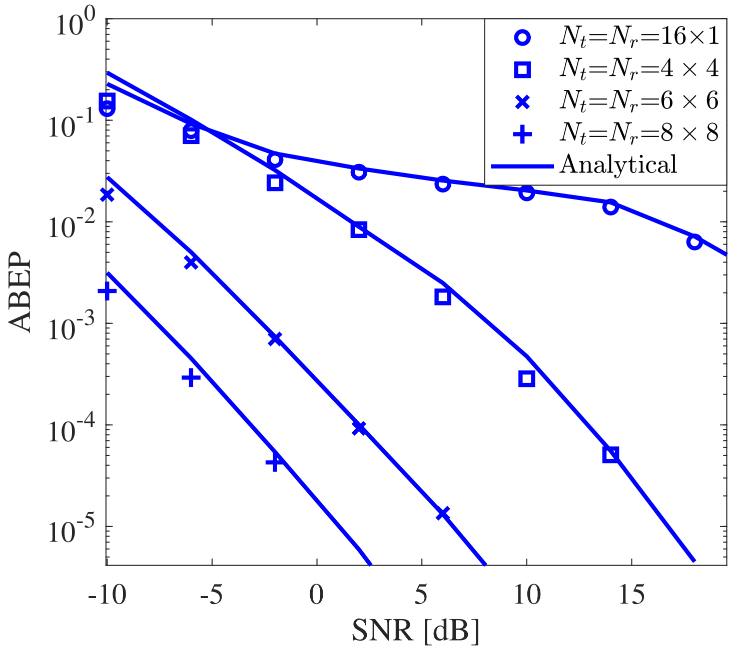

Fig. 3.7 The ABEP of 3-D SSM systems under the indoor environment case 3. The analytical and simulation results are represented by solid lines and markers, respectively.

instability on the bit error performance, resulting in the lower ABEP. Therefore, an enriched scattering environment can benefit the ABEP performance of 3-D SSM systems.

Furthermore, the decrease in N_{ts} may directly lead to a decrease in the system throughput, because the number of scattering paths that can be selected for conveying information bits may reduce. Specifically, if the 3-D SSM system has $N_{\text{ts}} = 5$ scattering paths, the system can select $K = 4$ candidate scattering paths to convey the information, where the selection of scattering paths can convey $\log_2(K) = 2$ bits for the single RF-chain system. If N_{ts} is reduced to 2 in the single RF-chain 3-D SSM system, the system only has $K = 2$ candidate scattering paths, where the selection of scattering paths just can convey $\log_2(K) = 1$ bit. Thus, the reduction in the number of scattering paths may result in the system throughput decrease.

Secondly, the system ABEP performance with different K and M combinations is compared. The 6×6 antenna arrays are applied, and five candidate paths are considered for 3-D SSM systems. With the typical indoor environment case 1, the results in Fig. 3.9 indicate that increasing the number of selected scattering paths can improve the bit error performance. Compared the system performance with $K = 2$ and $K = 4$, when the modulation order $M = 8$

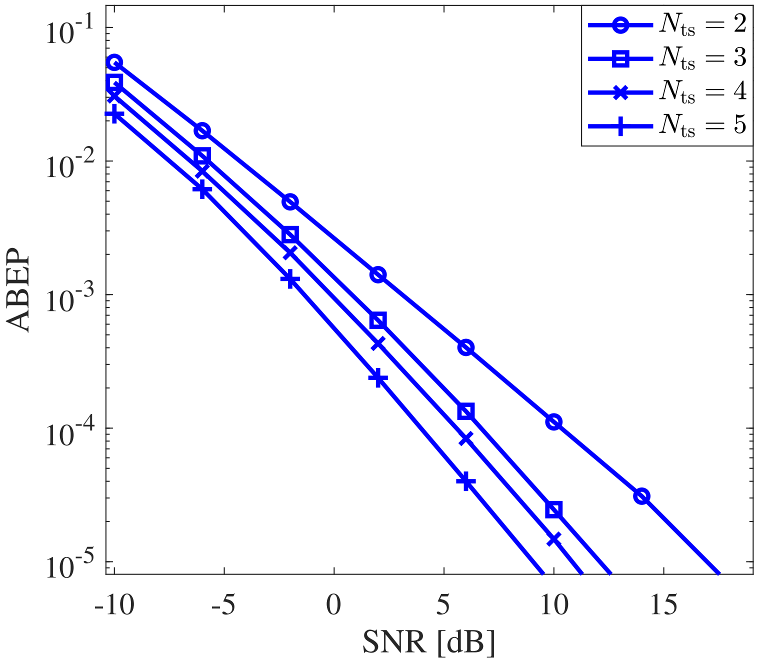

Fig. 3.8 The ABEP performance with different value of N_{ts}.

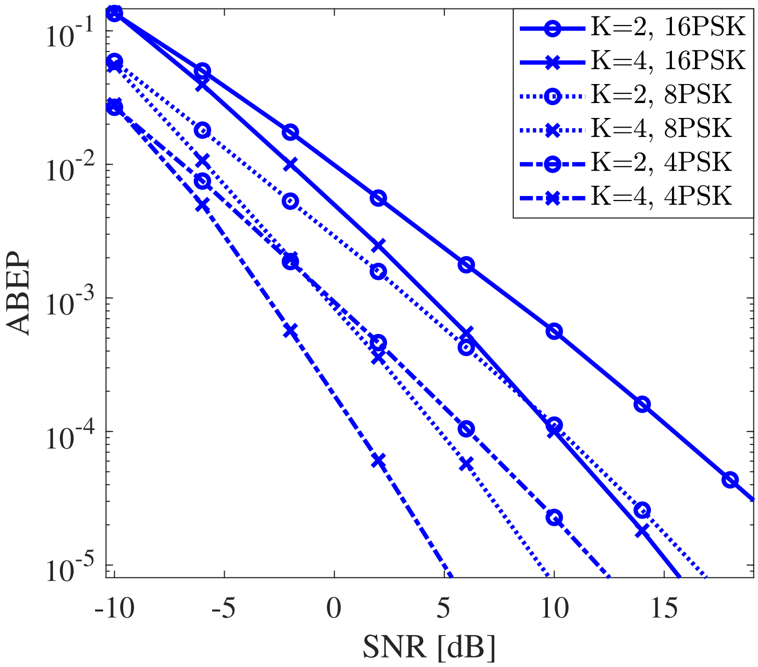

Fig. 3.9 The ABEP performance with different value of K and M.

and ABEP reaches 10^{-5}, the difference between the SNR is nearly 8 dB. Meanwhile, to compare the ABEP performance under the same data rate, we designed two sets of parameters $K = 2$, $M = 8$ and $K = 4$, $M = 4$, where the data rate is 4 bit per channel used. It can be seen that the system with $K = 4$, $M = 4$ has a better performance, when the ABEP reaches 10^{-5}. Due to the variability of channel gains, whether to choose a higher modulation order or select more scattering paths to improve the data rate needs to be determined according to the channel conditions.

3.5 Conclusion

In this chapter, a novel 3-D SSM system for mm-wave transmission has been proposed. The 3-D SSM system has combined beamforming technology to further utilise beamspace-domain resources, which has applied phase shifters to allocate the beam in the specified direction. The closed-form expression of the union upper bound on the ABEP has been derived and verified via comparison with simulations. In order to facilitate the implementation of 3-D SSM systems, the optimum detection algorithm has been designed to demodulate the directional beams in 3-D space. The results have shown that the proposed 3-D SSM system outperforms the 2-D SSM system in terms of ABEP, and the propagation environment impacts the performance of 3-D SSM systems significantly.

Chapter 4

The Generalised 3-D SSM System

Overview

In this chapter, the generalised 3-D SSM system is designed, which applies the hybrid beamforming scheme with multiple RF-chains. The generalised bit mapping scheme is also introduced for the transmitter with multiple RF-chains. Meanwhile, the optimum detection algorithm and the closed-form expression of the union upper bound on ABEP are derived. The ABEP performance of the generalised 3-D SSM system is evaluated under the statical and stochastic propagation environments.

4.1 Introduction

To meet the increasing wireless traffic demand, massive MIMO and mm-wave are two key technologies enabling to improve the SE and pursuing high data rate [4]. On account of the shorter wavelength of mm-wave, it enables the realization of a large-scale MIMO antenna array, which can be leveraged to achieve narrow and directional beams in the spatial-domain [110]. With the development of massive MIMO systems, the beamforming architecture with multiple RF-chains has attracted a lot of attention. The gain brought by beamforming technology and large-scale MIMO system can compensate for the attenuation of the mm-wave signal, ensuring the strength and stability of beams [111]. Combined with the beamforming technology, the IM schemes can extend the spatial-domain resource to the beamspace-domain, which generates the directional beams to convey the information bits.

Recently, IM systems working in the beamspace domain, e.g., the SSM has been proposed [16]. In the previous chapter, the SSM equipped with a full-dimensional MIMO system is proposed and analysed, where the beam directions have been described in both horizontal and vertical dimensions. However, the SSM system is limited to using a single RF-chain for signal transmission, and the SSM system performance with several RF-chains has not been investigated.

For the SSM system with a single RF-chain, the extra information bits are represented by a selected scattering path. Therefore, the data rate of the single RF-chain SSM system is limited by the number of scattering paths. Meanwhile, the receiver can only refer to the transmission direction from a single beam during the demodulation. The hybrid beamforming allows the transmitter to generate several RF-chains in a time slot. With multiple RF-chains, the combinations of scattering paths can be utilised to convey the extra information bits. Since the number of combinations is greater than the number of scattering paths, the symbol rate can be effectively improved under a specific transmission environment with multiple RF-chains. Furthermore, due to the combination of several scattering paths being used to convey extra information bits, when the received SNR is high, the more pronounced difference between the combinations can benefit the system bit error performance.

In this chapter, the generalised 3-D SSM system with multiple RF-chains is proposed. The system structure is introduced at first. Then the optimum detection algorithm is designed. To evaluate the performance of the generalised 3-D SSM system, the ABEP union upper bounds are derived under the statical and stochastic propagation environments, respectively. Finally, the ABEP performance of the generalised 3-D SSM system is analysed under different propagation environments. Without otherwise declarations, the notations in this chapter follow the instructions in Table. 3.1.

4.2 The System Design

In this section, the generalised 3-D SSM modulator with multiple RF-chains is introduced at first. Then the demodulation scheme is designed based on the whitening filter. The transmitter and receiver models of the proposed generalised 3-D SSM system are illustrated in Fig. 4.1 and Fig. 4.2, respectively.

4.2.1 The Generalised 3-D SSM Modulator

Following the modulation scheme in chapter 3.1.2, the bit block of the generalised 3-D SSM can be divided into two streams that are transmitted simultaneously, which can be represented by R_K and R_M. R_K represents the bits conveyed by selected scattering paths, and R_M represents the bits conveyed by selecting transmitted symbols.

For the generalised 3-D SSM system, it assumes that the transmitter adopts $K_\mathrm{c} \leq K$ RF-chains by hybrid beamforming. For generating K_c beams on the beamspace domain, an array of phase shifters is applied to adjust the phase of each transmit antenna element in the planar array. With the unit power, the transmitted symbol $\mathbf{x}$ can be represented as

$$\mathbf{x} = \sum_{k_\mathrm{c}=1}^{K_\mathrm{c}} s_{m_{k_\mathrm{c}}} \boldsymbol{\tau}_{\mathrm{t},k(k_\mathrm{c})}. \tag{4.1}$$

where k is the index of candidate scattering paths combinations, $k_\mathrm{c} \in \{1,2,...,K_\mathrm{c}\}$ is the order of the k_c-th selected scattering path, $k(k_\mathrm{c})$ is the index of the selected scattering path, which is determined by the order of k_c-th selected scattering path in K candidate scattering paths, $s_{m_{k_\mathrm{c}}}$ is the signal beamformed to the $k(k_\mathrm{c})$-th scattering path, $m_{k_\mathrm{c}} \in \{1,...,M\}$ is the index of the baseband modulation scheme on k_c-th scattering path, and $\boldsymbol{\tau}_{\mathrm{t},k(k_\mathrm{c})}$ is the beam-steering vector at the transmitter for the $k(k_\mathrm{c})$-th selected scattering path and can be computed by [25]

$$\boldsymbol{\tau}_{\mathrm{t},k(k_\mathrm{c})} = \left(\mathbf{a}_{\mathrm{t,v},k(k_\mathrm{c})} \otimes \mathbf{a}_{\mathrm{t,h},k(k_\mathrm{c})}\right)^{\mathrm{H}}. \tag{4.2}$$

where, $\mathbf{a}_{\mathrm{t,v},k(k_\mathrm{c})}$ is the transmitting array vectors for the planar array in each column and $\mathbf{a}_{\mathrm{t,h},k(k_\mathrm{c})}$ is transmitting array vectors for the planar array in each row. And $\boldsymbol{\tau}_{\mathrm{t},k(k_\mathrm{c})}$ is assumed

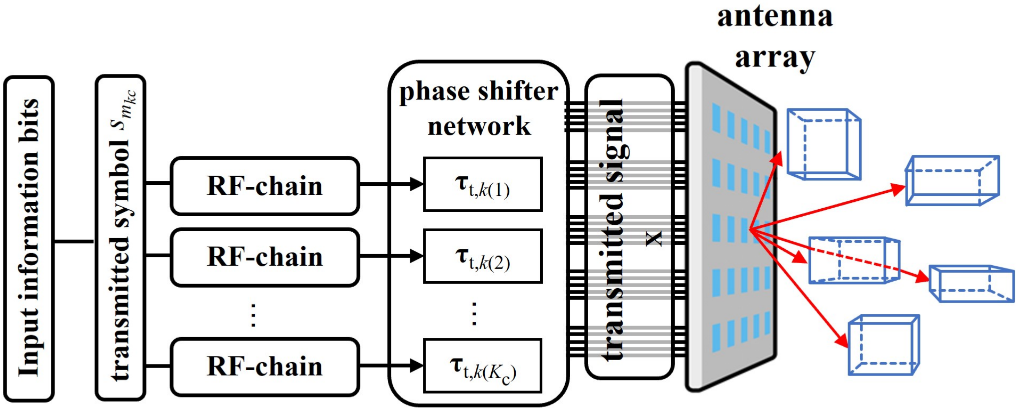

Fig. 4.1 The transmitter structure of generalised 3-D SSM system.

to be known at the transmitter. According to the 3-D channel model introduced in chapter 3.1.3, the array vectors $\mathbf{a}_{t,v,k(k_c)}$ and $\mathbf{a}_{t,h,k(k_c)}$ can be calculated by (3.8) and (3.9).

The SSM system uses scattering paths to relay information bits, with K_c RF-chains, there are $\binom{K}{K_c}$ possible combinations of scattering paths to represent different information bits. We define that all scattering paths combinations used for transmission belong to set $\Phi_{c,l}$, where $l = 1,2,...,L$ and L is the total number of the subsets in set $\Phi_{c,l}$. To demonstrate the generalised 3-D SSM bits mapping scheme, we give an example as follows.

Example 3. *The system with $K = 5$ scattering paths with $K_c = 2$ RF-chains are considered at the transmitter, which can provide $\binom{K}{K_c} = 10$ different scattering path combinations. Since we require a constellation point size in multiples of 2, we only use 8 of the possible 10 combinations. Then $\Phi_{c,l}$ can be represented as*

$$\Phi_{c,l} \in \{\{k|1,2\},\{k|1,3\},\{k|1,4\},\{k|1,5\},\{k|2,3\},\{k|2,4\},\{k|2,5\},\{k|3,4\}\} \tag{4.3}$$

where $l \in 1,2,3,...,8$ is the order of the elements in set $\Phi_{c,l}$. If $\Phi_{c,6} = \{k|2,4\}$ is selected, which means the 2nd and 4th candidate scattering paths are selected to transmit [34]. Then $k(k_c)$ has two components, which are $k(1) = 2$ and $k(2) = 4$. According to (4.2)*, the*

Table 4.1 The example of bits mapping scheme for the generalised 3-D SSM system

$[s_0, s_1, s_2]$	000	001	010	011
l	1	2	3	4
	$\boldsymbol{\tau}_{\mathrm{t},1}, \boldsymbol{\tau}_{\mathrm{t},2}$	$\boldsymbol{\tau}_{\mathrm{t},1}, \boldsymbol{\tau}_{\mathrm{t},3}$	$\boldsymbol{\tau}_{\mathrm{t},1}, \boldsymbol{\tau}_{\mathrm{t},4}$	$\boldsymbol{\tau}_{\mathrm{t},1}, \boldsymbol{\tau}_{\mathrm{t},5}$
$[s_0, s_1, s_2]$	100	101	110	111
l	5	6	7	8
	$\boldsymbol{\tau}_{\mathrm{t},2}, \boldsymbol{\tau}_{\mathrm{t},3}$	$\boldsymbol{\tau}_{\mathrm{t},2}, \boldsymbol{\tau}_{\mathrm{t},4}$	$\boldsymbol{\tau}_{\mathrm{t},2}, \boldsymbol{\tau}_{\mathrm{t},5}$	$\boldsymbol{\tau}_{\mathrm{t},3}, \boldsymbol{\tau}_{\mathrm{t},4}$
$[s_3, s_4]$	00	01	10	11
m_1	1	2	3	4
	$\frac{1+1j}{\sqrt{2}}$	$\frac{1-1j}{\sqrt{2}}$	$\frac{-1+1j}{\sqrt{2}}$	$\frac{-1-1j}{\sqrt{2}}$
$[s_5, s_6]$	00	01	10	11
m_2	1	2	3	4
	$\frac{1+1j}{\sqrt{2}}$	$\frac{1-1j}{\sqrt{2}}$	$\frac{-1+1j}{\sqrt{2}}$	$\frac{-1-1j}{\sqrt{2}}$

beam-steering vectors can be computed by

$$\boldsymbol{\tau}_{\mathrm{t},2} = \left(\mathbf{a}_{\mathrm{t,v},2} \otimes \mathbf{a}_{\mathrm{t,h},2}\right)^{\mathrm{H}}, \boldsymbol{\tau}_{\mathrm{t},4} = \left(\mathbf{a}_{\mathrm{t,v},4} \otimes \mathbf{a}_{\mathrm{t,h},4}\right)^{\mathrm{H}}. \tag{4.4}$$

As $\Phi_{\mathrm{c},l}$ *shown in* (4.3)*, the 8 combinations of candidate scattering paths can represents* $\log_2(8) = 3$ *bits. We assume that the phase-shift keying (PSK) with* $M = 4$ *is applied for baseband modulation, thus each selected scattering path can conveyed* $\log_2 M = 2$ *information bits. Generally, the bits mapping scheme is summarize in Table. 4.1.*

If the data bits

$$I = \left[\underbrace{1,0,1,}_{\boldsymbol{\tau}_{\mathrm{t},2},\boldsymbol{\tau}_{\mathrm{t},4}} \underbrace{0,0}_{s_{m_1}}, \underbrace{1,0}_{s_{m_2}}\right] \tag{4.5}$$

are transmitted, the first 3 bits $[1,0,1]$ *are conveyed by the scattering paths combination* $\Phi_{\mathrm{c},6}$*. The 4th-5th information bits* $s_{m_1} = [0,0]$ *is transmitted through the candidate scattering path selected by* $\boldsymbol{\tau}_{\mathrm{t},2}$*, which is represented by the 4PSK modulation symbol. Similarly, the 6th-7th information bits* $s_{m_2} = [1,0]$ *is transmitted through the candidate scattering path selected by* $\boldsymbol{\tau}_{\mathrm{t},4}$*.*

In general, with K_{c} active RF-chains at the transmitter, $R_K = \lfloor \log_2 \binom{K}{K_{\mathrm{c}}} \rfloor = \log_2(L)$ bits are conveyed by scattering paths selection, among K candidate scattering paths. K_{c} selected

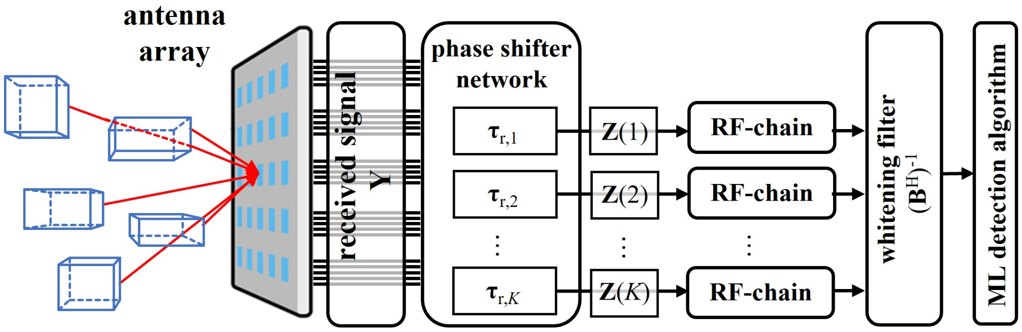

Fig. 4.2 The receiver structure of generalised 3-D SSM system.

paths can convey $R_M = \log_2(M^{K_\mathrm{C}})$ bits by conventional modulation scheme. Therefore, a block of $R = R_K + R_M = \lfloor \log_2 \binom{K}{K_\mathrm{c}} \rfloor + \log_2(M^{K_\mathrm{C}})$ bits can be transmitted in each time slot.

4.2.2 The Optimum Detector for 3-D SSM System

Following the 3-D channel model described in Chapter 3.1.3, the channel matrix **H** can be calculated by

$$\mathbf{H} = \frac{1}{\sqrt{N_\mathrm{t}}} \sum_{n_\mathrm{s}=1}^{N_\mathrm{ts}} \beta_{n_\mathrm{s}} \tilde{\mathbf{H}}_{n_\mathrm{s}}. \tag{4.6}$$

Assuming that the receiver has perfect CSI, the received signal can be derived as follows.

$$\mathbf{y} = \sqrt{\frac{\rho}{K_\mathrm{c}}} \mathbf{H} \sum_{k_\mathrm{c}=1}^{K_\mathrm{c}} s_{m_{k_\mathrm{c}}} \boldsymbol{\tau}_{\mathrm{t},k(k_\mathrm{c})} + \mathbf{n}_\mathrm{a}. \tag{4.7}$$

All received signals are collected by the receiver, where the directional beam with specific AoD is associated with a selected scattering paths. The output signal of the $k^{(\mathrm{r})}$-th RF-chain is represented by

$$\mathbf{z}(k^{(\mathrm{r})}) = \boldsymbol{\tau}_{\mathrm{r},k^{(\mathrm{r})}} \mathbf{y} = \sqrt{\frac{\rho}{K_\mathrm{c}}} \sum_{k_\mathrm{c}=1}^{K_\mathrm{c}} \boldsymbol{\tau}_{\mathrm{r},k^{(\mathrm{r})}} \mathbf{H} \boldsymbol{\tau}_{\mathrm{t},k(k_\mathrm{c})} s_{m_{k_\mathrm{c}}} + \boldsymbol{\tau}_{\mathrm{r},k^{(\mathrm{r})}} \mathbf{n}_\mathrm{a}, \tag{4.8}$$

where $\boldsymbol{\tau}_{\mathrm{r},k^{(r)}}$ is the beam-steering vector at the receiver for the $k^{(r)}$-th scattering path and can be computed by (3.14). Following the method in Section 3.1.4, the effective MIMO matrix

$\ddot{\mathbf{H}}$ and the effective additive Gaussian noise $\widetilde{\mathbf{n}}(k^{(\mathrm{r})})$ can be represented by

$$\ddot{\mathbf{H}}_{n_s}(k^{(\mathrm{r})},k) = \boldsymbol{\tau}_{\mathrm{r},k^{(\mathrm{r})}}\tilde{\mathbf{H}}_{n_\mathrm{s}}\boldsymbol{\tau}_{\mathrm{t},k(k_\mathrm{c})}, \tag{4.9}$$

$$\widetilde{\mathbf{n}}(k^{(\mathrm{r})}) = \boldsymbol{\tau}_{\mathrm{r},k^{(\mathrm{r})}}\mathbf{n}_\mathrm{a}. \tag{4.10}$$

By substituting the effective MIMO matrix and the effective additive Gaussian noise into (4.6) and (4.8), the received signal from specific scattering paths can be computed by

$$\begin{aligned}\mathbf{z} &= \sqrt{\frac{\rho}{K_\mathrm{c}N_\mathrm{t}}}\sum_{n_\mathrm{s}=1}^{N_\mathrm{ts}}\sum_{k_\mathrm{c}=1}^{K_\mathrm{c}}\boldsymbol{\tau}_{\mathrm{r},k^{(\mathrm{r})}}\beta_{n_\mathrm{s}}\tilde{\mathbf{H}}_{n_\mathrm{s}}\boldsymbol{\tau}_{\mathrm{t},k(k_\mathrm{c})}s_{m_{k_c}} + \boldsymbol{\tau}_{\mathrm{r},k^{(\mathrm{r})}}\mathbf{n}_\mathrm{a}\\ &= \sqrt{\frac{\rho}{K_\mathrm{c}N_\mathrm{t}}}\sum_{n_\mathrm{s}=1}^{N_\mathrm{ts}}\beta_{n_\mathrm{s}}\sum_{k_\mathrm{c}=1}^{K_\mathrm{c}}\ddot{\mathbf{H}}_{n_s}(:,k(k_\mathrm{c}))s_{m_{k_c}} + \boldsymbol{\tau}_{\mathrm{r},k^{(\mathrm{r})}}\mathbf{n}_\mathrm{a}\\ &= \sqrt{\frac{\rho}{K_\mathrm{c}N_\mathrm{t}}}\sum_{n_\mathrm{s}=1}^{N_\mathrm{ts}}\beta_{n_\mathrm{s}}\ddot{\mathbf{H}}_{n_s}\mathbf{w}_{l,m_{k_c}} + \widetilde{\mathbf{n}},\end{aligned} \tag{4.11}$$

where $\mathbf{w}_{l,m_{k_c}}$ is a $K \times 1$ vector with K_c non-zero elements, and can be calculated by

$$\mathbf{w}_{l,m_{k_c}}(k) = \begin{cases} s_{m_{k_c}}, & k(k_\mathrm{c}) \in \Phi_{\mathrm{c},l} \\ 0, & \text{else.} \end{cases} \tag{4.12}$$

Following the derivations in Lemma 1, with equation (3.18), the optimal detection algorithm of the generalised 3-D SSM system is obtained in the following Theorem 4.1.

Theorem 4.1 (Optimum detection algorithm for the generalised 3-D SSM system)**.** *The optimum detection algorithm for the proposed generalised 3-D SSM is given by*

$$[\hat{l},\hat{m}_{k_\mathrm{c}}] = \arg\min_{l,m_{k_\mathrm{c}}}\left\|\left(\mathbf{B}^\mathrm{H}\right)^{-1}\mathbf{z} - \sqrt{\frac{\rho}{K_\mathrm{c}N_\mathrm{t}}}\sum_{n_\mathrm{s}=1}^{N_\mathrm{ts}}\beta_{n_\mathrm{s}}\left(\mathbf{B}^\mathrm{H}\right)^{-1}\ddot{\mathbf{H}}_{n_s}\mathbf{w}_{l,m_{k_c}}\right\|, \tag{4.13}$$

where matrix $\mathbf{B}$ *satisfies that* $\mathbf{C}_\mathrm{noise} = \mathbf{B}\mathbf{B}^\mathrm{H}$*, and can be computed by Cholesky factorization.*

The proof of Theorem 4.1 is similar to Theorem 3.1, and its derivation is not repeated here.

4.3 ABEP Performance Analysis

To analyse the performance of generalised 3-D SSM system, the union upper bound on the ABEP is derived in this section. Since the scatterer in the propagation environment is not always static, in this section, the union upper bound on ABEP will be discussed based on the statically and randomly distributed scatterers, respectively.

4.3.1 The ABEP Union Upper Bound with Statical Propagation Environment

For the generalised 3-D SSM system with the hybrid beamforming technique, the ABEP union bound expression can be computed as

$$\begin{aligned}\text{ABEP} \leq & \sum_{l=1}^{L}\sum_{\hat{l}=1}^{L}\underbrace{\sum_{m_1=1}^{M}\cdots\sum_{m_{K_c}=1}^{M}}_{K_c}\underbrace{\sum_{\hat{m}_1=1}^{M}\cdots\sum_{\hat{m}_{K_c}=1}^{M}}_{K_c}\frac{1}{LM^{K_\mathrm{C}}} \\ & \times\frac{N(l,m_1,...,m_{K_\mathrm{c}}\to\hat{l},\hat{m}_1,...,\hat{m}_{K_\mathrm{c}})}{\log_2(LM^{K_\mathrm{C}})}\mathrm{P}\big(l,m_1,...,m_{K_\mathrm{c}}\to\hat{l},\hat{m}_1,...,\hat{m}_{K_\mathrm{c}}\big),\end{aligned} \tag{4.14}$$

where $N(l,m_1,...,m_{K_\mathrm{c}}\to\hat{l},\hat{m}_1,...,\hat{m}_{K_\mathrm{c}}) = N_\mathrm{l}(l\to\hat{l}) + N_\mathrm{m}(m_1,...,m_{K_\mathrm{c}}\to\hat{m}_1,...,\hat{m}_{K_\mathrm{c}})$ denotes the number of erroneous bits when $l,m_1,...,m_{K_\mathrm{c}}$ are transmitted but $\hat{l},\hat{m}_1,...,\hat{m}_{K_\mathrm{c}}$ are received. $N_\mathrm{l}(l\to\hat{l})$ is the number of wrong bits caused by $l\neq\hat{l}$, and $N_\mathrm{m}(m_1,...,m_{K_\mathrm{c}}\to\hat{m}_1,...,\hat{m}_{K_\mathrm{c}})$ is the number of wrong bits caused by $m_1,...,m_{K_\mathrm{c}}\neq\hat{m}_1,...,\hat{m}_{K_\mathrm{c}}$.

In order to explain how to get $N(l,m_1,...,m_{K_\mathrm{c}}\to\hat{l},\hat{m}_1,...,\hat{m}_{K_\mathrm{c}})$, an example is given in below. Following the equation (4.3), with the index of scattering path $K=5$, $K_\mathrm{c}=2$ and QPSK are used for baseband modulation. If the transmitted symbol with the index of the transmit scattering path $l=6$ and the index of the transmitted symbols $m_1=3$ and $m_2=1$, the receiver detects the index of scattering path $\hat{l}=5$ and the index of the transmitted symbol as $\hat{m}_1=3$ and $\hat{m}_2=2$. It means that the received bits have 2 bit error after demodulation. Therefore, the $N(l,m_1,...,m_{K_\mathrm{c}}\to\hat{l},\hat{m}_1,...,\hat{m}_{K_\mathrm{c}})$ is equal to 2 in this case.

In the equation (4.14) ,$\mathrm{P}(l, m_1, ..., m_{K_\mathrm{c}} \rightarrow \hat{l}, \hat{m}_1, ..., \hat{m}_{K_\mathrm{c}})$ is the APEP of generalised 3-D SSM system, and is computed by

$$\begin{aligned} &\mathrm{P}\left(l, m_1, ..., m_{K_\mathrm{c}} \rightarrow \hat{l}, \hat{m}_{k_1}, ..., \hat{m}_{K_\mathrm{c}} | \beta_1, \beta_2, \cdots, \beta_{N_\mathrm{ts}}\right) \\ =&\mathrm{P}\left(\left\| \left(\mathbf{B}^\mathrm{H}\right)^{-1} \mathbf{z} - \sqrt{\frac{\rho}{K_\mathrm{c} N_\mathrm{t}}} \sum_{n_\mathrm{s}=1}^{N_\mathrm{ts}} \beta_{n_\mathrm{s}} \left(\mathbf{B}^\mathrm{H}\right)^{-1} \ddot{\mathbf{H}}_{n_s} \mathbf{w}_{l, m_{k_\mathrm{c}}} \right\| \right. \\ \geq& \left. \left\| \left(\mathbf{B}^\mathrm{H}\right)^{-1} \mathbf{z} - \sqrt{\frac{\rho}{K_\mathrm{c} N_\mathrm{t}}} \sum_{n_\mathrm{s}=1}^{N_\mathrm{ts}} \beta_{n_\mathrm{s}} \left(\mathbf{B}^\mathrm{H}\right)^{-1} \ddot{\mathbf{H}}_{n_s} \mathbf{w}_{\hat{l}, \hat{m}_{k_\mathrm{c}}} \right\| \right), \end{aligned} \tag{4.15}$$

when the symbols $s_{m_1}, ..., s_{m_{k_\mathrm{c}}}$ are transmitted through the l-th group of scattering paths.

To simplify the derivation, we define $\mathbf{s}_{\mathscr{M}} = \{s_{m_1}, s_{m_2}, ..., s_{m_{K_\mathrm{c}}}\}$, and $\mathscr{M} = 1, 2, ..., M^{K_\mathrm{c}}$. $\mathbf{s}_{\mathscr{M}}$ is the set of all bits transmitted through different scattering paths. $\mathbf{s}_{\mathscr{M}}$ is the effective baseband symbol with modulation order $\mathscr{M}$. Therefore, the equation (4.14) can be rewritten as

$$\mathrm{ABEP} \leq \sum_{l=1}^{L} \sum_{\hat{l}=1}^{L} \sum_{\mathscr{M}=1}^{M^{K_\mathrm{c}}} \sum_{\hat{\mathscr{M}}=1}^{M^{K_\mathrm{c}}} \frac{1}{LM^{K_\mathrm{c}}} \frac{N(l, \mathscr{M} \rightarrow \hat{l}, \hat{\mathscr{M}})}{\log_2(LM^{K_\mathrm{c}})} \mathrm{P}\left(l, \mathscr{M} \rightarrow \hat{l}, \hat{\mathscr{M}}\right). \tag{4.16}$$

Before obtaining the ABEP, the closed-form APEP expression of the generalised 3-D SSM system should be derived at first.

Lemma 3 (Closed-form expressions of APEP)**.** *With* N_ts *scattering clusters, the closed-form expression of the APEP is computes as follows.*

$$\mathrm{P}\left(l, \mathscr{M} \rightarrow \hat{l}, \hat{\mathscr{M}}\right) \approx \frac{\prod_{n_s=1}^{N_\mathrm{ts}} \zeta'_{n_\mathrm{s}}}{12} + \frac{\prod_{n_s=1}^{N_\mathrm{ts}} \upsilon'_{n_\mathrm{s}}}{4}, \tag{4.17}$$

where $\zeta'_{n_\mathrm{s}} = \left(1 + \frac{\rho}{4N_\mathrm{ts}N_\mathrm{t}K_c} \omega'_{n_\mathrm{s}}\right)^{-1}$, $\upsilon'_{n_\mathrm{s}} = \left(1 + \frac{\rho}{3N_\mathrm{ts}N_\mathrm{t}K_c} \omega'_{n_\mathrm{s}}\right)^{-1}$, ω'_{n_s} *represents the* n_s*-th eigenvalue of* $\mathbf{W}'^\mathrm{H} \mathbf{C}_\mathrm{noise}^{-1} \mathbf{W}'$*, and*

$$\mathbf{W}'(:, n_\mathrm{s}) = \ddot{\mathbf{H}}_{n_s} \mathbf{w}_{l, m_{k_c}} - \ddot{\mathbf{H}}_{n_s} \mathbf{w}_{\hat{l}, \hat{m}_{k_c}}. \tag{4.18}$$

Proof:

Following the equation (4.15), the APEP $\mathrm{P}(l,\mathscr{M} \rightarrow l,\hat{\mathscr{M}})$ can be calculated based on the Q function.

$$\mathrm{P}\left(l,\mathscr{M} \rightarrow l,\hat{\mathscr{M}}\right) = \mathrm{E}_{\beta_{n_\mathrm{s}}}\left[Q\left(\sqrt{\frac{\rho}{2K_\mathrm{c}N_\mathrm{t}}\sum_{n_s=1}^{N_\mathrm{ts}}\left\|\beta_{n_\mathrm{s}}(\mathbf{B}^\mathrm{H})^{-1}\left(\ddot{\mathbf{H}}_{n_s}\mathbf{w}_{l,m_{kc}}-\ddot{\mathbf{H}}_{n_s}\mathbf{w}_{\hat{l},\hat{m}_{k_\mathrm{c}}}\right)\right\|}\right)\right]. \tag{4.19}$$

The variables in the Q function can be simplified as

$$(\mathbf{B}^\mathrm{H})^{-1}\left(\ddot{\mathbf{H}}_{n_s}\mathbf{w}_{l,m_{kc}}-\ddot{\mathbf{H}}_{n_s}\mathbf{w}_{\hat{l},\hat{m}_{k_\mathrm{c}}}\right) = (\mathbf{B}^\mathrm{H})^{-1}\mathbf{W}'(:,n_\mathrm{s}), \tag{4.20}$$

where $\mathbf{W}'$ is defined in (4.18). Following the equation (4.19), the variables can be derived as

$$\sum_{n_s=1}^{N_\mathrm{ts}}\left\|\beta_{n_\mathrm{s}}(\mathbf{B}^\mathrm{H})^{-1}\mathbf{W}'(:,n_\mathrm{s})\right\| = \boldsymbol{\beta}^\mathrm{H}\mathbf{W}'^\mathrm{H}\mathbf{B}^{-1}(\mathbf{B}^\mathrm{H})^{-1}\mathbf{W}'\boldsymbol{\beta} = \boldsymbol{\beta}^\mathrm{H}\mathbf{W}'^\mathrm{H}\mathbf{C}_\mathrm{noise}^{-1}\mathbf{W}'\boldsymbol{\beta}, \tag{4.21}$$

where $\boldsymbol{\beta}$ is the channel gain vector, and defined in (3.49). Utilising the eigenvalue decomposition on $\mathbf{W}'^\mathrm{H}\mathbf{C}_\mathrm{noise}^{-1}\mathbf{W}'$, the equation can be transformed as

$$\boldsymbol{\beta}^\mathrm{H}\mathbf{W}'^\mathrm{H}\mathbf{C}_\mathrm{noise}^{-1}\mathbf{W}'\boldsymbol{\beta} = \boldsymbol{\beta}^\mathrm{H}\mathbf{U}\boldsymbol{\Lambda}\mathbf{U}^\mathrm{H}\boldsymbol{\beta}. \tag{4.22}$$

Since $\boldsymbol{\beta}$ follows i.i.d. complex Gaussian distribution, and $\mathbf{U}$ is the unitary matrix. Let $\boldsymbol{\xi}^\mathrm{H}$=$\boldsymbol{\beta}^\mathrm{H}\mathbf{U}$ and $\boldsymbol{\xi}$=$\boldsymbol{\beta}\mathbf{U}^\mathrm{H}$, which still follows i.i.d. complex Gaussian distribution. The singular value matrix $\boldsymbol{\Lambda}$ can be represented as

$$\boldsymbol{\Lambda} = \mathrm{diag}\{\omega_1', \omega_2', ..., \omega_{N_\mathrm{ts}}''\}. \tag{4.23}$$

Combining (4.22) with (4.19), the APEP expression can be further simplified as

$$\mathrm{P}\left(l,\mathscr{M} \rightarrow \hat{l},\hat{\mathscr{M}}\right) = \mathrm{E}_\xi\left[Q\left(\sqrt{\frac{\rho}{2K_\mathrm{c}N_\mathrm{t}}\sum_{n_s=1}^{N_\mathrm{ts}}\|\xi_{n_s}\|\,\omega_{n_s}'}\right)\right], \tag{4.24}$$

where ξ_{n_s} are elements of matrix $\boldsymbol{\xi}$.

Applying the pure exponential approximation of Q function [107], the equation (4.24) is derived as follows.

$$\mathrm{P}\left(l,\mathscr{M}\rightarrow\hat{l},\hat{\mathscr{M}}\right)=\mathrm{E}_{\xi}\left[\frac{1}{12}e^{-\frac{\rho}{4N_{\mathrm{t}}K_{\mathrm{c}}}\sum\limits_{n_s=1}^{N_{\mathrm{ts}}}\|\xi_{n_s}\|\omega'_{n_s}}\right]+\mathrm{E}_{\xi}\left[\frac{1}{4}e^{-\frac{\rho}{3N_{\mathrm{t}}K_{\mathrm{c}}}\sum\limits_{n_s=1}^{N_{\mathrm{ts}}}\|\xi_{n_s}\|\omega'_{n_s}}\right]. \tag{4.25}$$

With the Gaussian variable ξ_{n_s}, the first part of equation (4.25) can be derived as

$$\begin{aligned}\mathrm{E}_{\xi}\left[\frac{1}{12}e^{-\frac{\rho}{4N_{\mathrm{t}}K_{\mathrm{c}}}\sum\limits_{n_s=1}^{N_{\mathrm{ts}}}\|\xi_{n_s}\|\omega'_{n_s}}\right]&=\frac{1}{12}\int\limits_{0}^{+\infty}\int\limits_{0}^{\|\xi_1\|}\cdots\int\limits_{0}^{\left\|\xi_{N_{\mathrm{ts}}-1}\right\|}\\&\times e^{-\frac{\rho\sum\limits_{n_s=1}^{N_{\mathrm{ts}}}\|\xi_{n_s}\|\omega'_{n_s}}{4N_{\mathrm{t}}K_{\mathrm{c}}}}e^{-\sum\limits_{n_s=1}^{N_{\mathrm{ts}}}\|\xi_{n_s}\|}\mathrm{d}\left\|\xi_{N_{\mathrm{ts}}}\right\|\cdots d\left\|\xi_2\right\|d\left\|\xi_1\right\|\\&=\frac{1}{12}\int\limits_{0}^{+\infty}\int\limits_{0}^{\|\xi_1\|}\cdots\int\limits_{0}^{\left\|\xi_{N_{\mathrm{ts}}-1}\right\|}e^{-\sum\limits_{n_s=1}^{N_{\mathrm{ts}}}\|\xi_{n_s}\|\left(1+\frac{\frac{\rho}{N_{\mathrm{t}}}\sum\limits_{n_s=1}^{N_{\mathrm{ts}}}\omega'_{n_s}}{4}\right)}\mathrm{d}\left\|\xi_{n_{\mathrm{ts}}}\right\|\cdots d\left\|\xi_2\right\|d\left\|\xi_1\right\|\\&=\frac{\prod\limits_{n_s=1}^{N_{\mathrm{ts}}}\left(1+\frac{\rho}{4N_{\mathrm{ts}}N_{\mathrm{t}}K_{\mathrm{c}}}\omega'_{n_{\mathrm{s}}}\right)^{-1}}{12}.\end{aligned} \tag{4.26}$$

$$\mathrm{E}_{\xi}\left[\frac{1}{4}e^{-\frac{\rho}{3N_{\mathrm{t}}K_{\mathrm{c}}}\sum\limits_{n_s=1}^{N_{\mathrm{ts}}}\|\xi_{n_s}\|\omega'_{n_s}}\right]=\frac{\prod\limits_{n_s=1}^{N_{\mathrm{ts}}}\left(1+\frac{\rho}{3N_{\mathrm{ts}}N_{\mathrm{t}}K_{\mathrm{c}}}\omega'_{n_s}\right)^{-1}}{4}. \tag{4.27}$$

By substituting (4.26), (4.27) into (4.25), the closed-form expression of $\mathrm{P}(l,\mathscr{M}\rightarrow\hat{l},\hat{\mathscr{M}})$ can be obtained as shown in (4.17). ■

4.3.2 The ABEP Union Upper Bound with Stochastic Propagation Environment

In the previous subsection, the ABEP expression with specific signal scattering paths is obtained. However, in the stochastic propagation environment, it is not guaranteed that the scatterer is in a specific position. To analyse the performance of the generalised 3-D SSM systems under the general propagation environment with NLOS paths, the positions of scatterers can be described by a specific randomly distribution in 3-D space. With the randomly distributed scatterers, the beam direction angles of scattering paths, i.e., AoA/AoD, can be formed. In this subsection, the ABEP expression of the generalised 3-D SSM system is derived for the scatterers located following a certain randomly distribution.

When the positions of scatterers follow a specific distribution, combining (3.7) and (4.14), the union upper bound of ABEP can be represented as

$$\begin{aligned}\mathrm{ABEP} &\leq \sum_{l=1}^{L}\sum_{\hat{l}=1}^{L}\sum_{\mathscr{M}=1}^{M^{K_\mathrm{C}}}\sum_{\hat{\mathscr{M}}=1}^{M^{K_\mathrm{C}}} \mathrm{E}_{\varphi_\mathrm{r},\theta_\mathrm{r}''}\mathrm{E}_{\varphi_\mathrm{t},\theta_\mathrm{t}''}\left[\frac{N\left(l,\mathscr{M}\to\hat{l},\hat{\mathscr{M}}\right)\mathrm{P}\left(l,\mathscr{M}\to\hat{l},\hat{\mathscr{M}}\right)}{LM^{K_\mathrm{C}}\log_2(LM^{K_\mathrm{C}})}\right] \\ &= \sum_{l=1}^{L}\sum_{\hat{l}=1}^{L}\sum_{\mathscr{M}=1}^{M^{K_\mathrm{C}}}\sum_{\hat{\mathscr{M}}=1}^{M^{K_\mathrm{C}}} \underbrace{\int_0^{\pi}\cdots\int_0^{\pi}}_{\varphi_\mathrm{r},\theta_\mathrm{r}'',\varphi_\mathrm{t},\theta_\mathrm{t}''}\frac{N\left(l,\mathscr{M}\to\hat{l},\hat{\mathscr{M}}\right)\mathrm{P}\left(l,\mathscr{M}\to\hat{l},\hat{\mathscr{M}}\right)}{LM^{K_\mathrm{C}}\log_2(LM^{K_\mathrm{C}})} \\ &\quad\times f\left(\varphi_\mathrm{r},\theta_\mathrm{r}''\right)f\left(\varphi_\mathrm{t},\theta_\mathrm{t}''\right)\mathrm{d}\varphi_\mathrm{r}\mathrm{d}\theta_\mathrm{r}''\mathrm{d}\varphi_\mathrm{t}\mathrm{d}\theta_\mathrm{t}'',\end{aligned} \tag{4.28}$$

where $f\left(\varphi_\mathrm{r},\theta_\mathrm{r}''\right)$ and $f\left(\varphi_\mathrm{t},\theta_\mathrm{t}''\right)$ are the PDF of φ and θ'' in 3-D channel model. Since we assume that the ranges of φ and θ'' are 0 to π, the corresponding integral ranges are 0 to π. Combining (4.28) with (4.17), the union upper bound of ABEP with randomly distributed scatterers can be calculated.

By substituting the PDF of the specific randomly distribution in (4.28), the system ABEP performance with a stochastic propagation environment can be obtained. In the next section, the system performance with the scatterer's AoA/AoD following uniform and Gaussian distributions is analysed. Meanwhile, the ABEP performance is also analysed under the COST2100 channel model.

4.4 Numerical Results and Discussions

In this section, we first validate the numerical results of ABEP in the generalised 3-D SSM system under a statical propagation environment. Then, for the stochastic propagation

Table 4.2 Channel parameters

	W_{i}	L_{i}	H_{i}	BS (x_{B}, y_{B}, h_{B})	UE (x_{U}, y_{U}, h_{U})
Case 1	6 m	6 m	3 m	(5, 6, 1.2)	(1, 1, 1.2)
Case 2	10 m	10 m	3 m	(4, 2, 1.2)	(6, 8, 1.2)

environment, three channel models are utilised to analyse the performance of the generalised 3-D SSM system. For the performance analysis, the planar array antennas are considered at both transmitter and receiver. The distance between each antenna element is a half wavelength. M-PSK is adopted as the baseband modulation scheme.

4.4.1 The System Performance under the Statical Propagation Environment

Following the propagation environment illustrated in Section 3.3, two cases are set to evaluate the generalised 3-D SSM system. The parameters for the two cases are shown in Table 4.2. With statical scatterers, the channel impulse responses are generated by ray-tracing [109] in this subsection.

The ABEP union upper bound of generalised 3-D SSM system is validated with the indoor propagation environment case 1 and case 2 at first. The 4×4 antenna arrays are adopted. $K = 5$ scattering paths and $k_{\mathrm{c}} = 2$ RF-chains are generated in each time slot to convey the information bits.

As shown in Fig. 4.3, the numerical results are matched with the simulation results. For the generalised 3-D SSM system, the ABEP performance is degraded with the modulation order M increase. Meanwhile, compared the system performance in different indoor propagation environment, the large size of the room in case 2 can benefit the ABEP performance. For the generalised 3-D SSM system, a part of information bits are conveyed by the selection of scattering paths, which is determined by the specific array vectors. With the large size room, the relatively big differences of scattering path characteristics reduce the difficulty of array vectors identification, which results in the better ABEP performance.

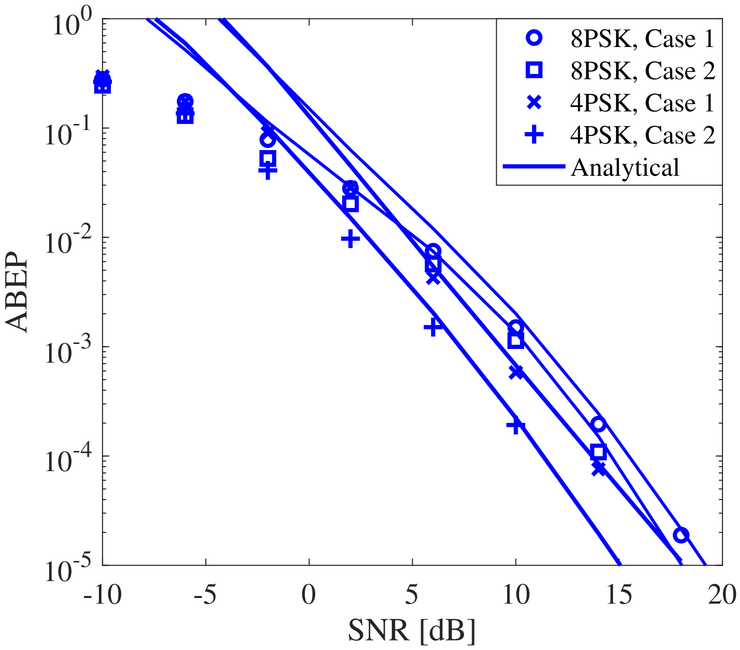

Fig. 4.3 The ABEP performance under different modulation orders. The analytical and simulation results are represented by solid lines and markers, respectively.

With different sizes of antenna arrays, i.e.,4×4, 6×6 and 8×8, applying for the transceivers, the numerical and simulation results are shown in Fig. 4.4 and 4.5 with the indoor environments case 1 and case 2, respectively. It can be seen from Fig. 4.4 and 4.5 that the system performance is improved with the increase of the antenna array size.

As shown in Fig. 4.4 and Fig. 4.5, it can be seen that the SNR gaps between 16×1 and 4×4 antenna arrays are above 5 dB for the multiple-RF-chain systems when the ABEP reaches 10^{-3}. This indicates that the ABEP performance of 2-D generalised SSM system is significantly degraded by the indiscernible scattering paths. It is worth noting that the ABEP performance of 3-D SSM did not fluctuate significantly due to the change of propagation environment, compared with the 2-D SSM system. Due to the extension of DoF in the horizontal direction, the system can identify beams by the direction information in both horizontal and vertical dimensions. Therefore, generalised 3-D SSM has more stable ABEP performance than generalised 2-D SSM when the propagation environment changes.

After applying hybrid beamforming, the ABEP performance may be affected due to the more complex scattering path combinations. Therefore, the system ABEP performance

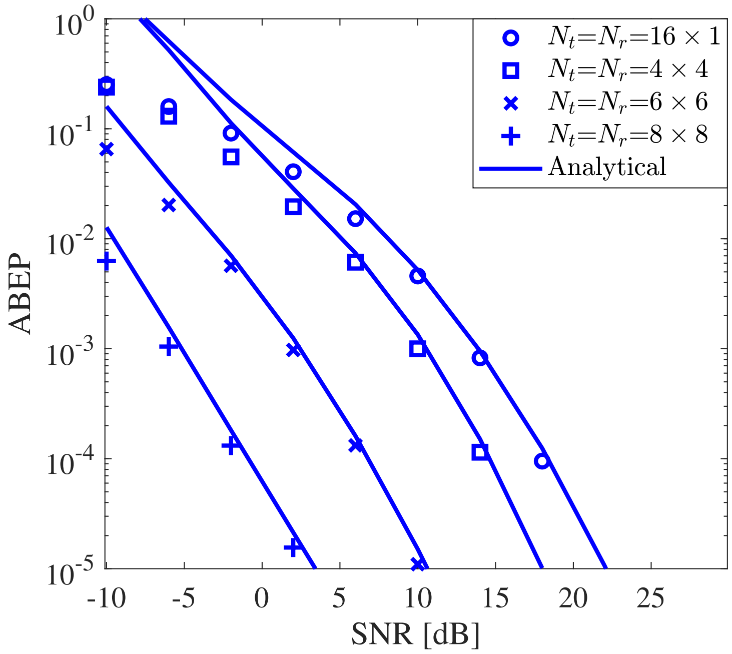

Fig. 4.4 The ABEP of generalised 3-D SSM system under statical indoor environment case 1. The analytical and simulation results are represented by solid lines and markers, respectively.

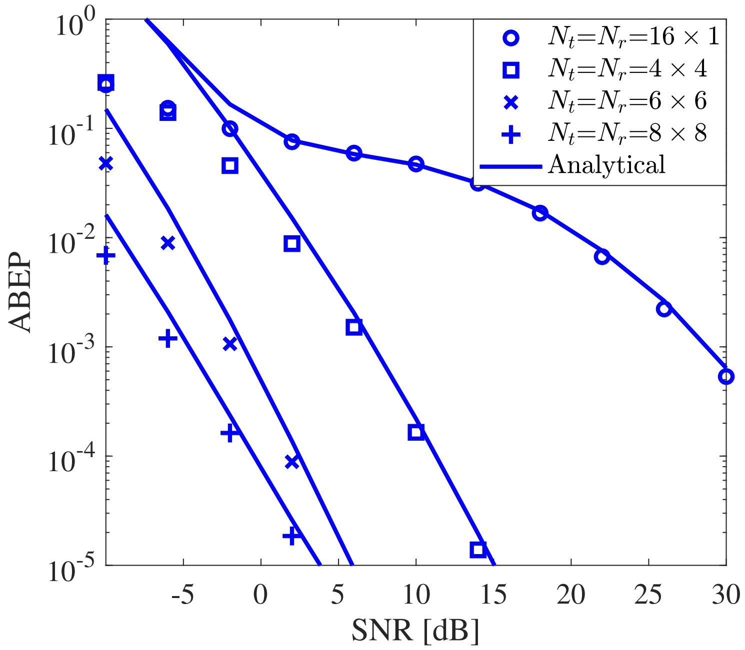

Fig. 4.5 The ABEP of generalised 3-D SSM systems under statical indoor environment case 2. The analytical and simulation results are represented by solid lines and markers, respectively.

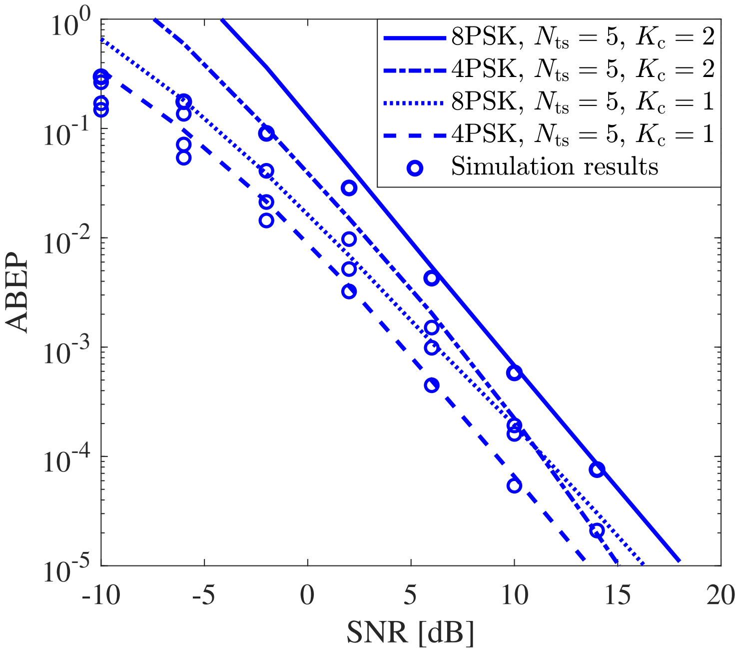

Fig. 4.6 The ABEP of generalised 3-D SSM systems under statical indoor environment case 2 with 4×4 antenna arrays. The analytical and simulation results are represented by solid lines and markers, respectively.

should be compared between the single RF-chain and multiple RF-chains systems. The simulation and analytical results are shown in Fig. 4.6 and Fig. 4.7 with 4×4 and 6×6 antenna arrays, respectively. $N_{\rm ts}=5$, $K=5$ and $K_{\rm c}=2$ are set for the multiple RF-chains system, $N_{\rm ts}=5$, $K=4$ and $K_{\rm c}=1$ for the single-RF-chain system. Compared with the system adopting 8PSK, it can be seen that the system adopted 4PSK has better ABEP performance under the same $N_{\rm ts}$ and $K_{\rm c}$. For statical environment case 2 with 4×4 antenna arrays, the SNR difference are about 3.2 dB and 4.9 dB with $K_c=2$ and $K_c=1$, respectively. As shown in Fig. 4.6 and Fig. 4.7, the multiple RF-chains system with $M=4$ outperform the single RF-chain system with $M=8$, when the received SNR is more than 10.6 dB and -2.7 dB, respectively. It should be noticed that when $M=4$ the data rate for the multiple RF-chains system is 7 bits/symbol and the data rate for the single RF-chain system is 5 bits/symbol. Therefore, the multiple-RF-chain system with a large number of candidate scattering paths is conducive to reducing the ABEP and improving the symbol rate, especially when the

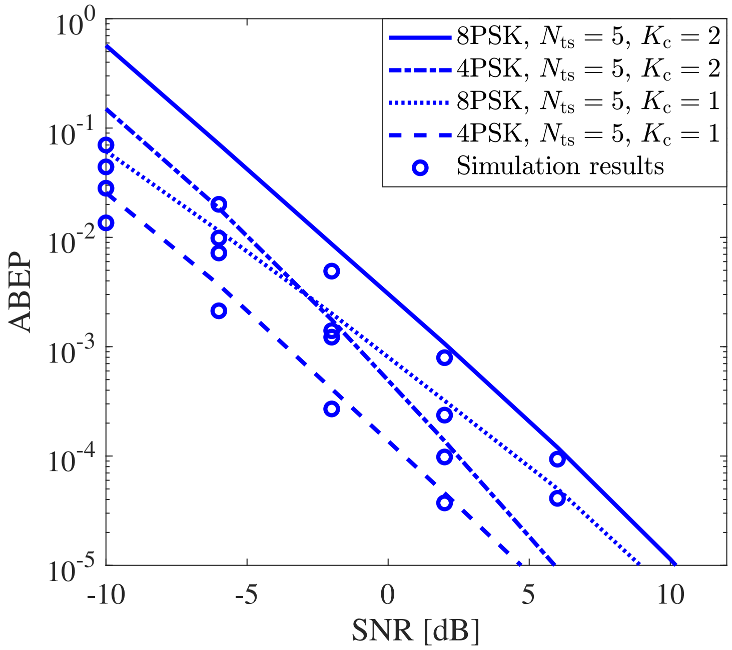

Fig. 4.7 The ABEP of generalised 3-D SSM systems under statical indoor environment case 2 with 6×6 antenna arrays. The analytical and simulation results are represented by solid lines and markers, respectively.

received SNR is high. Meanwhile, the performance improvement is more pronounced when the size of the antenna array is large.

4.4.2 The generalised 3-D SSM Performance with Stochastic Propagation Environment

In this subsection, the generalised 3-D SSM system performance is analysed under three stochastic propagation environments, which are listed as follows.

- Environment 1: AoAs/AoDs of scatterers follow uniform distribution on a spherical surface [112].
- Environment 2: AoAs/AoDs of scatterers follow 2-D Gaussian distributions [113].
- Environment 3: The COST 2100 channel model [114].

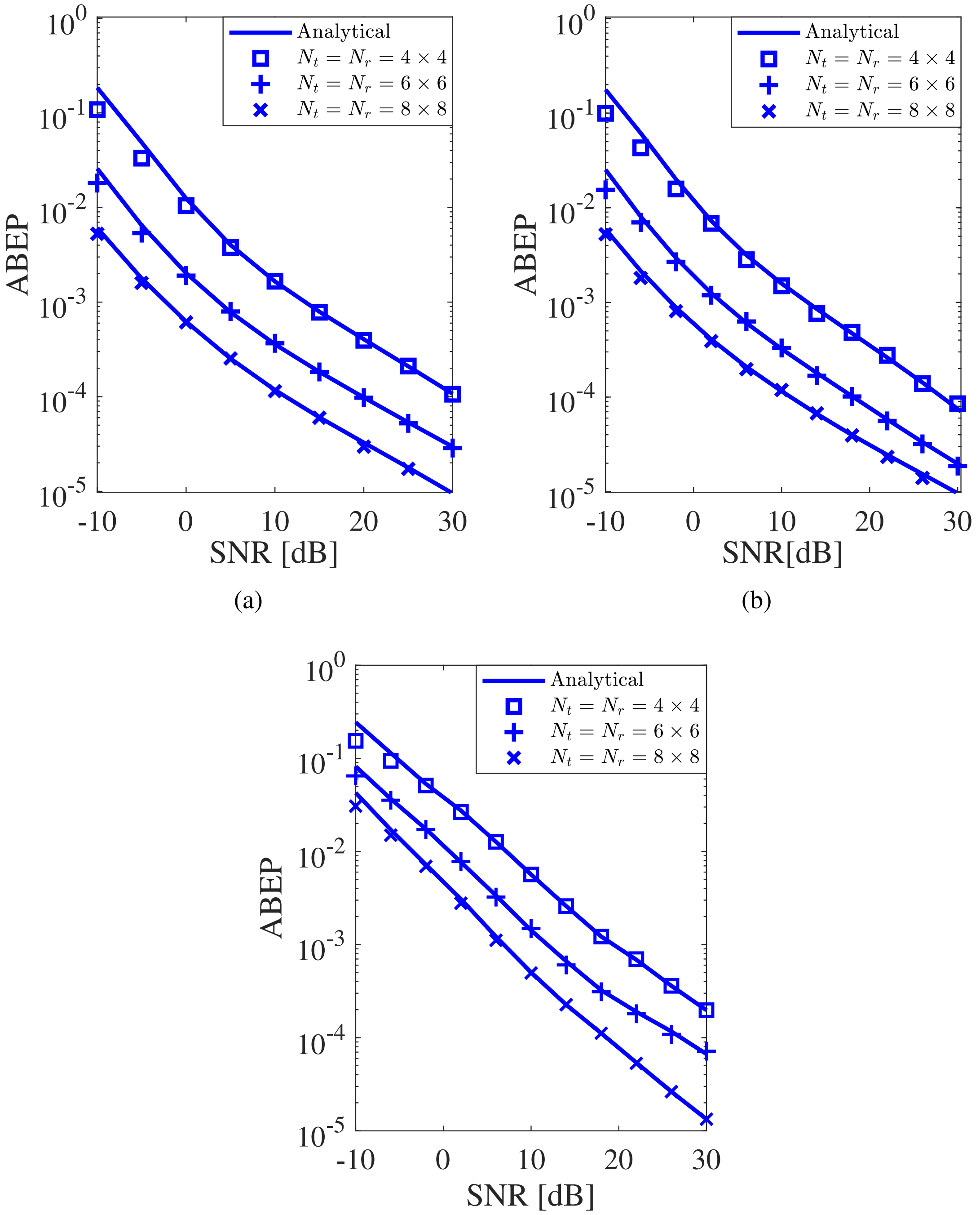

(a)

(b)

(c)

Fig. 4.8 The ABEP performance of generalised 3-D SSM system under three stochastic propagation environment with random distributed scatterers. $M = 4$, $K = 2$, $K_{\mathrm{c}} = 1$ are adopted for the analysis. The analytical and simulation results are represented by solid lines and markers, respectively. (a) uniformly distributed scatterers. (b) 2-D Gaussian distributed scatterers with $\psi = 9$. (c) the COST 2100 channel model.

Environment 1

According to the characteristics of electromagnetic wave propagation, random angles that describe the direction of scatterers are defined on a spherical surface. For spherical coordinates, the PDF of φ and θ'' in uniform distribution is shown in below [112]

$$f(\varphi_{\mathrm{t}}) = \frac{1}{\pi}, \quad f\left(\theta_{\mathrm{t}}''\right) = \frac{1}{4\pi}\sin(\theta_{\mathrm{t}}''), \tag{4.29}$$

where $\theta_{\mathrm{t}}'', \varphi_{\mathrm{t}} \in (0, \pi)$ since a planar antenna array is considered. $\theta_{\mathrm{r}}'', \varphi_{\mathrm{r}}$ follows the same distribution as $\theta_{\mathrm{t}}'', \varphi_{\mathrm{t}}$. With (4.28), the numerical results can be obtained, which are verified by the simulation results in Fig. 4.8 (a).

Comparing with the fixed scatterers paths, ABEP performance for random distributed scatterers direction angles in Fig. 4.8 (a) is worse because the aliasing scatterers are more likely to appear. Taking 8×8 antenna array as an example, when ABEP reaches 10^{-5}, the SNR increases by about 20 dB compared with the situations in Fig. 4.4 (a).

Environment 2

The von Mises-Fisher distribution is the equivalent of Gaussian distribution in 3-D space [115]. The PDF for the random 3-D unit vector $\boldsymbol{\eta}$ following von Mises-Fisher distribution can be expressed as [113]

$$f(\boldsymbol{\eta}; \mathbf{o}, \psi) = \frac{\psi}{4\pi \sinh(\psi)} \exp\left(\psi \mathbf{o}^{\mathrm{T}} \boldsymbol{\eta}\right), \tag{4.30}$$

where $\mathbf{o}$ is the mean direction of von Mises-Fisher distribution, and $\|\mathbf{o}\| = 1$. $\psi > 0$ is the concentration parameter, $\boldsymbol{\eta}$ is an unit vector for a general point of the 3-D space. The higher the spread of the point generating the PDF, the lower ψ is. According to [116], the von Mises-Fisher distribution can be transformed to spherical polar coordinates. If $\boldsymbol{\eta}$ following $f(\boldsymbol{\eta}; \mathbf{o}, \psi)$, we denote $\mathbf{g} = [\theta_{\mathrm{t}}'', \varphi_{\mathrm{t}}]$ for the corresponding angular version. And the density function of $(\theta_{\mathrm{t}}'', \varphi_{\mathrm{t}})$ is

$$f(\varphi_{\mathrm{t}}, \theta_{\mathrm{t}}'') = \frac{\psi}{4\pi \sinh(\psi)} \exp\left(\psi \vartheta(\mathbf{o}'') \vartheta(\mathbf{g})^{\mathrm{T}}\right) \sin\theta'', \tag{4.31}$$

where $\mathbf{o}''$ is the spherical polar coordinates vector of $\mathbf{o}$, and $\vartheta(\cdot)$ is a computational method. For a vector $\boldsymbol{\gamma}$, we denote $\vartheta(\boldsymbol{\gamma}) = [\cos\gamma_1, \cos\gamma_1 \sin\gamma_2]$, as long as $\boldsymbol{\gamma} = [\gamma_1, \gamma_2]$ [115]. The distribution of θ_{r}'' and φ_{r} can be obtained by the same method.

With the (4.31) and (4.28), the numerical results of the generalised 3-D SSM system with Gaussian distribution of scatterers is plotted in Fig. 4.8 (b). Due to the concentration of scattering paths, it is more challenging for the receiver to distinguish different scattering paths, resulting in the degradation of ABEP performance.

Environment 3

The COST 2100 is a geometry-based stochastic channel model, which is proposed to simulating the MIMO channel between the static BS and mobile devices [114]. The COST 2100 channel model is established according to the measurement of static propagation environments in 3-D space with corresponding scatterers, which considers the delay, AoAs, AoDs. The clusters in the COST 2100 channel model are formed by grouping scatterers. Since the COST 2100 channel model has a detailed description of the scattering path characteristic, it is suitable for modelling the scattering channel of generalised 3-D SSM systems. Therefore, in this subsection, the COST 2100 channel model will be adopted to construct a stochastic propagation environment for evaluating the performance of generalised 3-D SSM systems.

With MATLAB implementation of the COST 2100 model [117], an indoor channel environment is applied to evaluate the generalised 3-D SSM system performance, which considers one local cluster and multiple single-bounce clusters in the indoor scenario. The parameters of the indoor propagation environment are set according to the second measurement in [118]. The positions of BS and UE adopt the same parameters as shown in Table 4.2 case 2. For further details about the COST 2100 channel model, the reader may refer to

[119, 120]. Furthermore, the analytical results for the system with the COST 2100 channel model are also obtained based on the Q function [107].

The simulation and analytical results in Fig. 4.8 (c) show that the generalised 3-D SSM system can still work normally with the COST 2100 channel model. Compared with other stochastic channel models shown in Fig. 4.8, the system performance is slightly reduced. For 8×8 antenna arrays, when the ABEP reaches 10^{-4}, the SNR difference between the system applying the COST 2100 channel model and the system considering 2-D Gaussian distributed scatterers is nearly 6.6 dB.

Comparing with the typical indoor propagation environment shown in Fig. 4.4, the ABEP performance is degraded with the stochastic propagation environment, because the scattering paths cannot be perfectly separated. According to (4.11), with the possible small angles between scatterers, the received signal transmitted through different scattering paths may not be perfectly separated due to the similar AoAs/AoDs, the various channel gains and the interference among beams. If the receiver cannot perfectly separate the signal from different scattering paths, which may cause an error in the scattering paths detection and increase the ABEP. In other words, when multiple scattering paths cannot be separated, the system will recognize them as one path. Therefore, the total number of the scattering paths N_{ts} existing between the transmitter and receiver will be reduced. The decrease of N_{ts} will lead to the reduction of the diversity gain, thus increasing the ABEP. The diversity gain of 3-D SSM systems will be derived and discussed in the next section.

In the practical network planning and modulation mode selection, the method in this section can be applied to different scatterer distribution models, which can predict the ABEP performance under various scatterer distribution models for the generalised 3-D SSM system.

4.5 Conclusion

In this chapter, we have proposed a novel generalised 3-D SSM system with planar arrays. To facilitate the optimum demodulation of the generalised 3-D SSM system, the whitening-filter-based optimum detection algorithm has been derived. To efficiently evaluate the system performance, the expression of the ABEP union upper bound has been provided. For the performance analysis, ABEPs are analysed under the statical and the stochastic propagation environments, respectively. Compared with the statical propagation environment, the ABEP performance of generalised 3-D SSM system is degraded under the stochastic propagation environment.

Chapter 5

Optimisation schemes of Generalised 3-D SSM Systems

Overview

In the previous chapters, the system model of 3-D SSM was designed and the performance was evaluated. However, as a modulation system applying a large antenna array and a complex phase shifter network, its hardware friendliness and detection algorithm complexity need to be considered. In this chapter, a hardware-friendly design is proposed to reduce the hardware complexity of the generalised 3-D SSM system. On the other hand, to reduce the computational complexity of the detector, a low-complexity linear detection algorithm is designed. Furthermore, for the fast evaluation, the diversity gain and the asymptotic performance are also derived.

5.1 Introduction

In the previous chapter, the generalised 3-D SSM system has been introduced. To reduce the hardware complexity and the computational complexity of detection algorithm, two optimisation schemes are proposed for the generalised 3-D SSM system in this chapter. Meanwhile, for the quick evaluation, the asymptotic performance is also derived based on the diversity gain and the coding gain of the generalised 3-D SSM system.

For the system deployment, a large number of antenna elements are configured on the transceivers. Each of the antenna elements requires a corresponding RF-link. For the conventional modulation system, a huge analogue phase shifter network should be designed to support the beamforming process. Regardless of the transmitter or receiver, such a large phase shifter network will undoubtedly increase the equipment cost and power consumption. Therefore, a hardware friendliness design is introduced to reduce the complexity of transceivers in this chapter. The analogue phase shifter network is replaced by a multi-bit phase shifter network with limited quantification [121], which applies a 2-D FFT based transceiver approach.

For the demodulation process, the optimum detection algorithms introduced in the previous chapters are designed based on ML detection. The computational complexity of the optimum detector is increased exponentially with the number of candidate scattering paths, especially for the multiple RF-chains systems. If a large number of scattering paths or a high modulation order is adopted, the computational complexity is great. Many existing works have devised the low-complexity detection algorithms for IM systems [45–47, 53, 54, 61, 92, 93], which have been introduced in chapter 2. However, the low-complexity detection algorithm for generalised 3-D SSM systems is missing in the literature. Therefore, an MMSE based low-complexity detection algorithm is designed and analysed in this chapter. Moreover, the asymptotic performance of the generalised 3-D SSM system is derived with the coding gain and the diversity gain for a quick assessment.

5.2 The Hardware Friendliness Design for Modulator and Demodulator

5.2.1 The Structure of Hardware Friendliness Transceivers

In section 4.1.1 and section 4.1.2, the analogue phase shifter networks are applied in the modulator and the demodulator. For a practical transceiver design, the application of multi-bit phase shifter networks with limited quantification can further reduce the cost of hardware

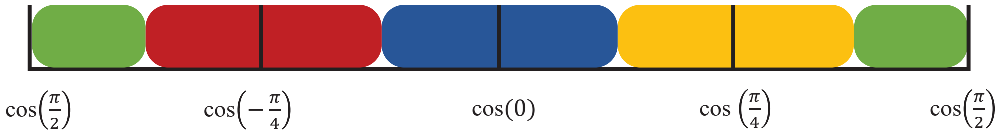

Fig. 5.1 The 2-D FFT rounding example. Four ranges of values are represented by four different colours. All angle values in this range are allocated at the medians $\cos\left(\frac{\pi}{2}\right)$, $\cos\left(-\frac{\pi}{4}\right)$, $\cos(0)$ and $\cos\left(\frac{\pi}{4}\right)$ after applying FFT.

deployment [121]. In this subsection, the 2-D FFT-based transceiver is designed to reduce the hardware cost [122].

Recalling the array vector for transmitter, which uses the analogue phase shifter network to obtain the continuous phase and can be represented as

$$\mathbf{a}_{\mathrm{t,v},n_\mathrm{s}} = [1, e^{j2\pi d_{\mathrm{t,v}}\cos\varphi_{\mathrm{t},n_\mathrm{s}}}, e^{j4\pi d_{\mathrm{t,v}}\cos\varphi_{\mathrm{t},n_\mathrm{s}}}, \ldots, e^{j2(N_{\mathrm{t,v}}-1)\pi d_{\mathrm{t,v}}\cos\varphi_{\mathrm{t},n_\mathrm{s}}}], \tag{5.1}$$

$$\mathbf{a}_{\mathrm{t,h},n_\mathrm{s}} = [1, e^{j2\pi d_{\mathrm{t,h}}\cos\theta_{\mathrm{t},n_\mathrm{s}}}, e^{j4\pi d_{\mathrm{t,h}}\cos\theta_{\mathrm{t},n_\mathrm{s}}}, \ldots, e^{j2(N_{\mathrm{t,h}}-1)\pi d_{\mathrm{t,h}}\cos\theta_{\mathrm{t},n_\mathrm{s}}}], \tag{5.2}$$

Applying the FFT matrix on $\mathbf{a}_{\mathrm{t,v},n_\mathrm{s}}$ and $\mathbf{a}_{\mathrm{t,h},n_\mathrm{s}}$, the transmission directions $\mathbf{a}'_{\mathrm{t,v},n_\mathrm{s}}$ and $\mathbf{a}'_{\mathrm{t,h},n_\mathrm{s}}$ are formed. The 2-D FFT algorithm results on each column and row of transmission antenna array can be represented as

$$\mathbf{a}'_{\mathrm{t,v},n_\mathrm{s}} = [1, e^{j2\pi d_{\mathrm{t,v}} q_{\mathrm{t,v},n_\mathrm{s}}}, \ldots, e^{j2(N_{\mathrm{t,v}}-1)\pi d_{\mathrm{t,v}} q_{\mathrm{t,v},n_\mathrm{s}}}], \tag{5.3}$$

$$\mathbf{a}'_{\mathrm{t,h},n_\mathrm{s}} = [1, e^{j2\pi d_{\mathrm{t,h}} q_{\mathrm{t,h},n_\mathrm{s}}}, \ldots, e^{j2(N_{\mathrm{t,h}}-1)\pi d_{\mathrm{t,h}} q_{\mathrm{t,h},n_\mathrm{s}}}], \tag{5.4}$$

where

$$q_{\mathrm{t,v},n_\mathrm{s}} = \frac{\mathrm{mod}\left(\lceil \cos\left(\varphi_{\mathrm{t},n_s}\right) N_{\mathrm{t,v}} d_{\mathrm{t,v}} \rfloor, N_{\mathrm{t,v}}\right)}{N_{\mathrm{t,v}} d_{\mathrm{t,v}}}, \tag{5.5}$$

$$q_{\mathrm{t,h},n_\mathrm{s}} = \frac{\mathrm{mod}\left(\lceil \cos\left(\theta_{\mathrm{t},n_s}\right) N_{\mathrm{t,h}} d_{\mathrm{t,h}} \rfloor, N_{\mathrm{t,h}}\right)}{N_{\mathrm{t,h}} d_{\mathrm{t,h}}}. \tag{5.6}$$

After applying 2-D FFT, the values of $\cos\left(\varphi_{\mathrm{t},n_s}\right)$ and $\cos\left(\theta_{\mathrm{t},n_s}\right)$ are aligned to $q_{\mathrm{t,v},n_\mathrm{s}}$ and $q_{\mathrm{t,h},n_\mathrm{s}}$ on vertical and horizontal directions, respectively. Taking a 4×4 planar array as an example, according to (5.5) and (5.6), $q_{\mathrm{t,v},n_\mathrm{s}}$ and $q_{\mathrm{t,h},n_\mathrm{s}}$ each have only 4 optional values, $\cos\left(\frac{\pi}{2}\right)$, $\cos\left(-\frac{\pi}{4}\right)$, $\cos(0)$ and $\cos\left(\frac{\pi}{4}\right)$, as shown in Fig. 5.1. For example, all value of angles in the

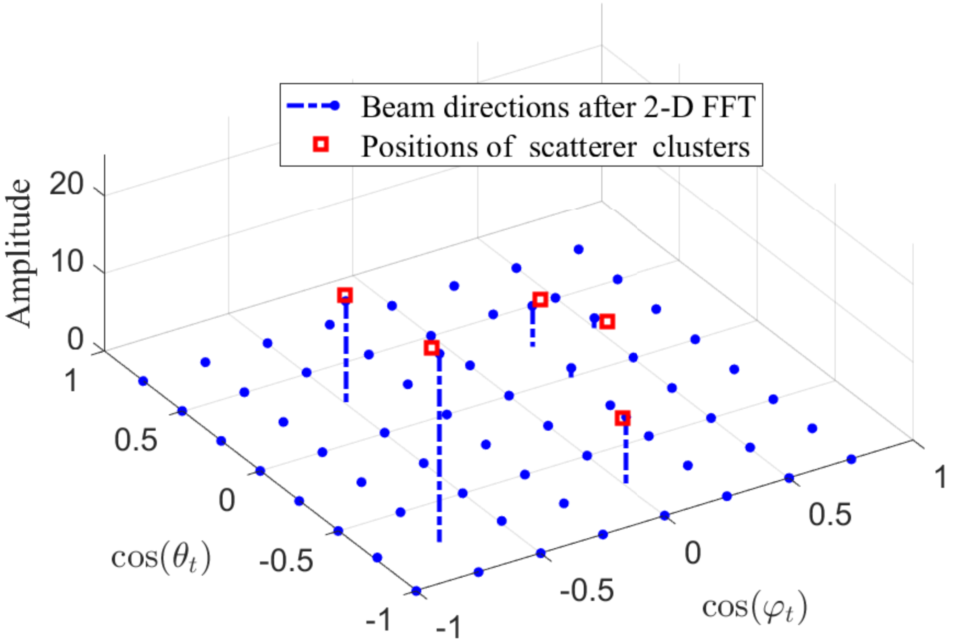

Fig. 5.2 The channel response amplitude after applying 2-D FFT algorithm.

red area should be aligned to $\cos\left(-\frac{\pi}{4}\right)$ after applying 2-D FFT. For the generalised 3-D SSM transmitter with 2-D FFT, the matrix $\boldsymbol{\tau}_{\mathrm{t},k(k_\mathrm{c})}$ can be rewritten as

$$\boldsymbol{\tau}'_{\mathrm{t},k(k_\mathrm{c})} = (\mathbf{a}'_{\mathrm{t,v},k(k_\mathrm{c})} \otimes \mathbf{a}'_{\mathrm{t,h},k(k_\mathrm{c})})^{\mathrm{H}}. \tag{5.7}$$

The 2-D FFT can also be applied at receiver. The $\boldsymbol{\tau}'_{\mathrm{r},k^{(r)}}$ can be obtained as

$$\boldsymbol{\tau}'_{\mathrm{r},k^{(r)}} = (\mathbf{a}'_{\mathrm{t,v,},k^{(r)}} \otimes \mathbf{a}'_{\mathrm{t,h},k^{(r)}})^{\mathrm{H}}. \tag{5.8}$$

Combining $\boldsymbol{\tau}'_{\mathrm{t},k(k_\mathrm{c})}$ and $\boldsymbol{\tau}'_{\mathrm{r},k^{(r)}}$ with formula (4.8), and repeating the previous derivation steps, we can get the received signal expressions of the SSM system after applying 2-D FFT. Then the optimum detection algorithm for the hardware-friendly demodulator can be derived. Fig. 5.2 shows the amplitude of the channel response with 5 candidate scattering paths using 8 × 8 transmitting antenna array. The red boxes in Fig. 5.2 represent beam scattering direction angles in the wireless channel, which are modulated by the analogue phase shifter

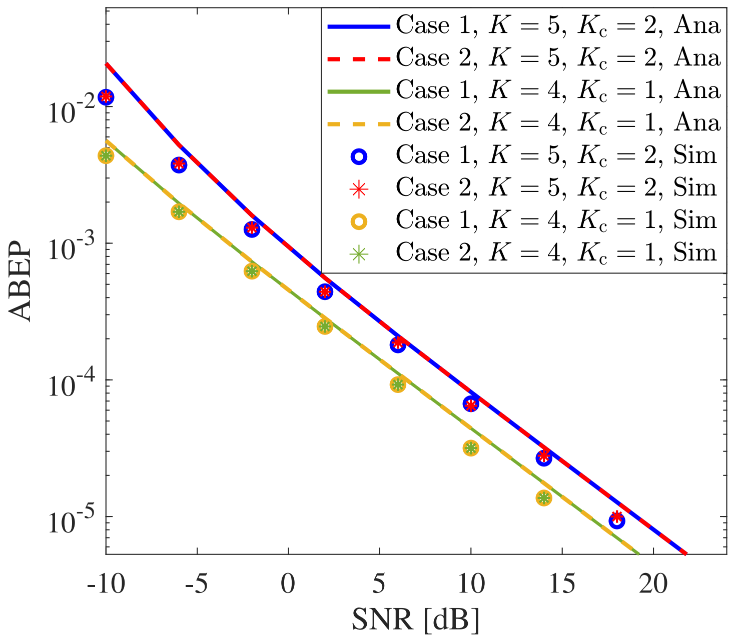

Fig. 5.3 The simulation and analytical results for the 2-D FFT based SSM system.

network at the transceiver. While blue points represent the predetermined beam directions generating by 2-D FFT algorithm. If the 2-D FFT algorithm is applied, the continuous phase of the signal will be modulated to the predetermined discrete directions as blue dots with non-zero amplitudes shown in Fig. 5.2. However, if applying the 2-D FFT algorithm on two beams with similar directions, their beam directions may be aliased, and such aliasing may cause system performance degradation, where the 2-D FFT transceiving approach provides a trade-off between ABEP performance and hardware complexity.

5.2.2 The Performance Evaluations and Discussions

To evaluate the performance of the 2-D FFT algorithm, the indoor propagation environments case 1 and case 2 in Table 4.2 are adopted. For the simulation and analytical results, the 8×8 antenna arrays and the 4PSK baseband modulation scheme are adopted. As shown in Fig. 5.3, the simulation results are matched with the analytical results.

It can be seen that in the two different propagation environments, there is no significant difference between the system ABEP performance after applying the 2-D FFT algorithm.

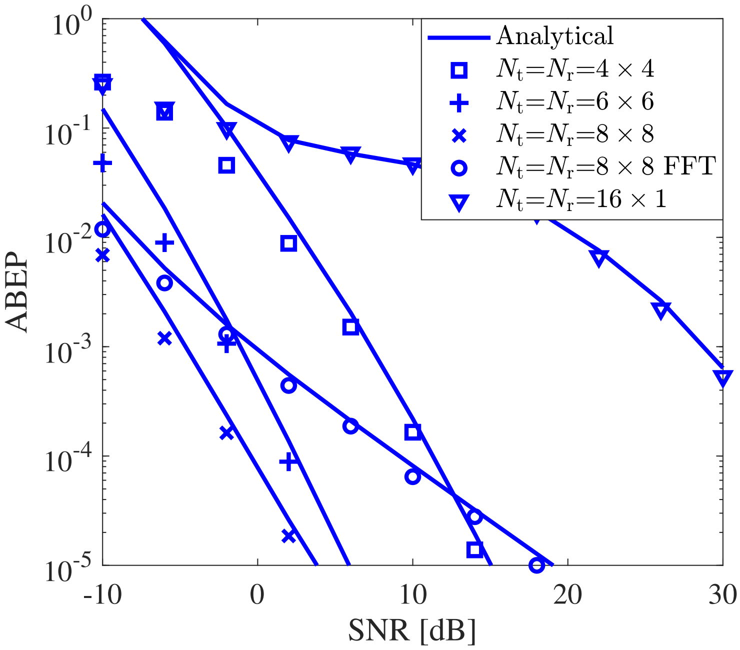

Fig. 5.4 The comparison between the generalised 3-D SSM system and the system with 2-D FFT algorithm. The indoor environment case 2 and 4PSK modulation scheme are adopted.

The reasons for its consistent ABEP performance are explained as follows. Although the room size and the position of transceivers are different, the scattering directions are aligned to the same pre-set AoAs and AoDs after applying the 2-D FFT algorithm, which leads to the similar ABEP performance.

Comparing with the system without 2-D FFT algorithm, the ABEP performance are shown in Fig. 5.4. The generalised 3-D SSM system with $K = 5$, $K_c = 2$ is applied. As mentioned above, the application of 2-D FFT algorithm significantly simplifies the transceiver's circuit complexity. However, due to the 2-D FFT algorithm, the transmission direction of the signal is not fully aligned with the direction angles of scatterers in the propagation environment, which in turn leads to an increase in ABEP. When the ABEP reaches 10^{-5}, the SNR differs from the system without 2-D FFT algorithm by nearly 14.6 dB for the multiple RF-chains system with 8×8 antenna arrays.

5.3 The Low-complexity Detection Algorithm

5.3.1 The Design of Linear MMSE Detection Algorithm

In the previous chapter, the optimum detection algorithm is designed for the generalised 3-D SSM system. If a generalised 3-D SSM system equips a large number of antenna elements, the optimum detection algorithm has a high computational complexity, which brings challenge to receiver design. Therefore, a linear MMSE detection algorithm is provided to reduce the computational complexity by avoiding the process of global search in the optimum detection algorithm [123, 124].

The incoming receive information bits can be divided into two parts R_K and R_M, which are conveyed by the selection of scattering paths and the conventional modulated symbols, respectively. With the received signal in (4.8), the proposed low-complexity detection algorithm is elaborated as follows. The first part of R_K bits can be detected according to the received energy on each scattering path. Then the rest of R_M bits are checked by the conventional ML detection algorithm for QAM/PSK signals.

Theorem 5.1 (The linear MMSE detection algorithm for the generalised 3-D SSM system)**.** *The first part of R_K bits can be detected according to the received energy on each scattering path. The linear MMSE detection algorithm for the selected scattering paths is given by*

$$[\hat{l}] = \arg\min_{l}\{\|\mathbf{G}\left(\mathbf{B}^{\mathrm{H}}\right)^{-1}\mathbf{z} - \bar{\mathbf{w}}_l\|\}, \tag{5.9}$$

where

$$\begin{aligned}\mathbf{G} = & \left[\left(\sqrt{\frac{\rho}{K_{\mathrm{c}}N_{\mathrm{t}}}}\sum_{n_{\mathrm{s}}=1}^{N_{\mathrm{ts}}}\beta_{n_{\mathrm{s}}}\left(\mathbf{B}^{\mathrm{H}}\right)^{-1}\ddot{\mathbf{H}}_{n_s}\right)^{\mathrm{H}}\left(\sqrt{\frac{\rho}{K_{\mathrm{c}}N_{\mathrm{t}}}}\sum_{n_{\mathrm{s}}=1}^{N_{\mathrm{ts}}}\beta_{n_{\mathrm{s}}}\left(\mathbf{B}^{\mathrm{H}}\right)^{-1}\ddot{\mathbf{H}}_{n_s}\right)+\mathbf{I}\right]^{-1} \\ & \times\left(\sqrt{\frac{\rho}{K_{\mathrm{c}}N_{\mathrm{t}}}}\sum_{n_{\mathrm{s}}=1}^{N_{\mathrm{ts}}}\beta_{n_{\mathrm{s}}}\left(\mathbf{B}^{\mathrm{H}}\right)^{-1}\ddot{\mathbf{H}}_{n_s}\right)^{\mathrm{H}},\end{aligned} \tag{5.10}$$

$\bar{\mathbf{w}}_l$ *is a* $K\times 1$ *vector with* K_c *non-zero elements, and can be computed by*

$$\bar{\mathbf{w}}_l=\begin{cases}1, & k(k_\mathrm{c})\in\Phi_{\mathrm{c},l},\\ 0, & \text{else},\end{cases}\tag{5.11}$$

and $\mathbf{I}$ *is a* $N_\mathrm{ts}\times N_\mathrm{ts}$ *identity matrix.*

Proof: From (3.17), the output signal passing through the whitening filter can be expressed as

$$\left(\mathbf{B}^\mathrm{H}\right)^{-1}\mathbf{z}=\sqrt{\frac{\rho}{K_\mathrm{c}N_\mathrm{t}}}\sum_{n_\mathrm{s}=1}^{N_\mathrm{ts}}\beta_{n_\mathrm{s}}\left(\mathbf{B}^\mathrm{H}\right)^{-1}\ddot{\mathbf{H}}_{n_s}\mathbf{w}_{l,m_{k_c}}+\mathbf{n}'_\mathrm{a}.\tag{5.12}$$

According to [123], the MMSE detection of l is

$$[\hat{l}]=\arg\min_{l}\{\|\mathbf{G}\left(\mathbf{B}^\mathrm{H}\right)^{-1}\mathbf{z}-\bar{\mathbf{w}}_l\|\},\tag{5.13}$$

where $\bar{\mathbf{w}}_l$ is defined in (5.11). The coefficient matrix $\mathbf{G}$ needs to be designed for the MMSE detection algorithm. According to the MMSE detection algorithm in [123]

$$\mathrm{E}\left[\left(\mathbf{G}\left(\mathbf{B}^\mathrm{H}\right)^{-1}\mathbf{z}-\mathbf{w}_{l,m_{k_c}}\right)\left(\left(\mathbf{B}^\mathrm{H}\right)^{-1}\mathbf{z}\right)^H\right]=0.\tag{5.14}$$

With the similar steps in [124], performing a simple transformation on the matrix, the matrix $\mathbf{G}$ can be represented as

$$\begin{aligned}\mathbf{G}&=\mathrm{E}\left[\mathbf{w}_{l,m_{k_c}}\left(\left(\mathbf{B}^\mathrm{H}\right)^{-1}\mathbf{z}\right)^H\right]\mathrm{E}\left[\left(\mathbf{B}^\mathrm{H}\right)^{-1}\mathbf{z}\left(\left(\mathbf{B}^\mathrm{H}\right)^{-1}\mathbf{z}\right)^H\right]^{-1}\\&=\left[\left(\sum_{n_\mathrm{s}=1}^{N_\mathrm{ts}}\beta_{n_\mathrm{s}}\left(\mathbf{B}^\mathrm{H}\right)^{-1}\sqrt{\frac{\rho}{K_\mathrm{c}N_\mathrm{t}}}\ddot{\mathbf{H}}_{n_s}\right)^\mathrm{H}\sum_{n_\mathrm{s}=1}^{N_\mathrm{ts}}\beta_{n_\mathrm{s}}\left(\mathbf{B}^\mathrm{H}\right)^{-1}\sqrt{\frac{\rho}{K_\mathrm{c}N_\mathrm{t}}}\ddot{\mathbf{H}}_{n_s}+\sigma^2\mathbf{I}\right]^{-1}\\&\quad\times\left(\sum_{n_\mathrm{s}=1}^{N_\mathrm{ts}}\beta_{n_\mathrm{s}}\left(\mathbf{B}^\mathrm{H}\right)^{-1}\sqrt{\frac{\rho}{K_\mathrm{c}N_\mathrm{t}}}\ddot{\mathbf{H}}_{n_s}\right)^\mathrm{H}.\end{aligned}\tag{5.15}$$

By substituting (5.15) into (5.13), when variance $\sigma^2=1$, the MMSE detection algorithm can be obtained as (5.9). ■

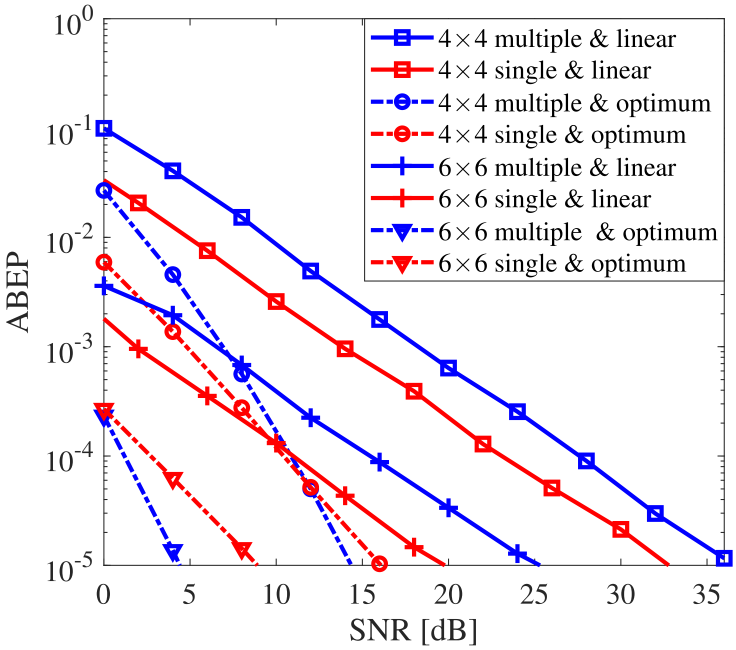

Fig. 5.5 The computational complexities of generalised 3-D SSM system detection algorithms. The computational complexities of single RF-chain systems are represented by solid lines, where $K_{\mathrm{c}} = 1$ and $K = 4$. The computational complexities of multiple RF-chains systems are represented by dotted lines, where $K_{\mathrm{c}} = 2$ and $K = 5$.

5.3.2 The Performance Evaluations and Discussions

The performance of the low-complexity detection algorithm is analysed in this subsection. Meanwhile, computational complexities of the low-complexity and the optimum detection algorithms are also compared. With the low-complexity detection algorithm, the system performance is shown in Fig. 5.5 under the typical indoor environment case 1 described in section 4.3.1. The 4PSK signal constellation is used for the baseband modulation. In Fig. 5.5, the red and blue lines represent the performance of the single RF-chain and the multiple RF-chains systems, respectively. The solid and dotted lines represent the performance of the low-complexity and the optimum detection algorithms, respectively.

For the low-complexity detection algorithm, the single RF-chain system has better ABEP performance than the multiple RF-chain system. When the ABER reaches 10^{-5}, the SNR gaps between two systems are 5.5 dB and 5.8 dB for 4×4 and 6×6 antenna arrays, respectively.

Comparing with the optimum detection algorithm, the simulation results illustrate that the low-complexity detection algorithm will cause a decrease in the ABEP performance. The reason for ABEP performance degradation is explained as follows. When the linear MMSE detection algorithm demodulates the first R_K bits incorrectly, the $\hat{l}$ does not equal to the l in (5.9). Due to $l \neq \hat{l}$ (the scattering paths recognition error), all remaining bits, which are conveyed by the conventional modulation symbol with index $\hat{l}, m_{k_c}$, cannot be detected correctly through the conventional single-input-single-output (SISO) ML detection algorithm. It results in a substantial increase in the ABEP. Nevertheless, for the optimum detection algorithm, even if the first R_K bits are detected incorrectly, the remaining bits conveyed by conventional modulation symbols may still be demodulated correctly with the global search.

In other words, the conventional modulation symbol is selected from a constraint set. The optimum detection algorithm considers the symbol selection constraints in the global search, e.g., the conventional modulation symbol is selected from 1 and -1 in the BPSK constellation. However, the constraint of conventional modulation symbol selection is not utilized by the linear MMSE detection algorithm. Therefore, the incomplete utilization of the symbol selection constraint leads to a decrease in the detection accuracy of l, which in turn leads to an increase in the ABEP for the low-complexity detection algorithm.

In general, even if the linear detection algorithm sacrifices part of the system performance, it is widely used in various modulation systems to reduce detection complexity. The detection complexity of the linear MMSE detection algorithm and the optimum detection algorithm are analysed as follows.

Based on floating operations (flops), the average computational complexities of the low-complexity detection algorithm and the optimum detection algorithm are evaluated. For both detection algorithms, if it is a real number, it assumes that every addition, subtraction, multiplication or division operation costs 1 flop. If it is a complex number, it assumes that every addition or subtraction operation costs 2 flops, and multiplication or division operation costs 6 flops. Computing the product between a real number and a complex number costs 2 flops. Moreover, it assumes that computations of some basic functions, including $\angle(\cdot)$, $\exp(\cdot)$, trigonometric function and square root, cost ρ flops. The Cholesky factorization

Table 5.1 Computational Complexity of Applied Operations

Index	Operation	Complexity
1	$\ddot{\mathbf{H}}_{n_s}(k^{(\mathrm{r})},k) = \boldsymbol{\tau}_{\mathrm{r},k^{(\mathrm{r})}}\tilde{\mathbf{H}}_{n_\mathrm{s}}\boldsymbol{\tau}_{\mathrm{t},k(k_\mathrm{c})}$	$K^2(8N_\mathrm{T}N_\mathrm{R}+6N_\mathrm{T} -2)+24N_\mathrm{T}N_\mathrm{R}$
2	$\frac{1-\exp\left(jN_{\mathrm{r,v}}2\pi d_{\mathrm{r,v}}\left(\cos\varphi_{\mathrm{r},k^{(\mathrm{r})}}-\cos\varphi_{\mathrm{r},k^{(\mathrm{r})'}}\right)\right)}{1-\exp\left(j2\pi d_{\mathrm{r,v}}\left(\cos\varphi_{\mathrm{r},k^{(\mathrm{r})}}-\cos\varphi_{\mathrm{r},k^{(\mathrm{r})'}}\right)\right)} \times\frac{1-\exp\left(jN_{\mathrm{r,h}}2\pi d_{\mathrm{r,h}}\left(\cos\theta_{\mathrm{r},k^{(\mathrm{r})}}-\cos\theta_{\mathrm{r},k^{(\mathrm{r})'}}\right)\right)}{1-\exp\left(j2\pi d_{\mathrm{r,h}}\left(\cos\theta_{\mathrm{r},k^{(\mathrm{r})}}-\cos\theta_{\mathrm{r},k^{(\mathrm{r})'}}\right)\right)}$	$K^2\left(48+12\rho\right)$
3	$\left(\mathbf{B}^\mathrm{H}\right)^{-1}$	$\frac{K^3}{2}+2K^2+\frac{3}{2}K-1+\varkappa$
4	$\sqrt{\frac{\rho}{K_\mathrm{c}N_\mathrm{t}}}\sum_{n_\mathrm{s}=1}^{N_\mathrm{ts}}\beta_{n_\mathrm{s}}\left(\mathbf{B}^\mathrm{H}\right)^{-1}\ddot{\mathbf{H}}_{n_s}$	$N_\mathrm{ts}\left(4K^3+K^2\right)$
5	$\left[\left(\sqrt{\frac{\rho}{K_\mathrm{c}N_\mathrm{t}}}\sum_{n_\mathrm{s}=1}^{N_\mathrm{ts}}\beta_{n_\mathrm{s}}\left(\mathbf{B}^\mathrm{H}\right)^{-1}\ddot{\mathbf{H}}_{n_s}\right)^\mathrm{H} \left(\sqrt{\frac{\rho}{K_\mathrm{c}N_\mathrm{t}}}\sum_{n_\mathrm{s}=1}^{N_\mathrm{ts}}\beta_{n_\mathrm{s}}\left(\mathbf{B}^\mathrm{H}\right)^{-1}\ddot{\mathbf{H}}_{n_s}\right)+\mathbf{I}\right]^{-1} \times\left(\sqrt{\frac{\rho}{K_\mathrm{c}N_\mathrm{t}}}\sum_{n_\mathrm{s}=1}^{N_\mathrm{ts}}\beta_{n_\mathrm{s}}\left(\mathbf{B}^\mathrm{H}\right)^{-1}\ddot{\mathbf{H}}_{n_s}\right)^\mathrm{H}$	$16K^3+K^2\left(3+3K!\right)+K\left(1+4K!\right) +N_\mathrm{ts}\left(4K^3+K^2\right)-9K!-1$
6	$\lVert\mathbf{G}\left(\mathbf{B}^\mathrm{H}\right)^{-1}\mathbf{z}-\bar{\mathbf{w}}_l\rVert$	$4K^3+6K^2+K\left(3+\rho\right)$
7	$\left\lVert\left(\mathbf{B}^\mathrm{H}\right)^{-1}\mathbf{z}-\sqrt{\frac{\rho}{K_\mathrm{c}N_\mathrm{t}}}\sum_{n_\mathrm{s}=1}^{N_\mathrm{ts}}\beta_{n_\mathrm{s}}\left(\mathbf{B}^\mathrm{H}\right)^{-1}\ddot{\mathbf{H}}_{n_s}\mathbf{w}_{l,m_{k_c}}\right\rVert$	$4K^2+K\left(3+\rho\right)+N_\mathrm{ts}\left(4K^3+7K^2\right)$

costs $\varkappa$ flops. For the $K \times K$ matrix $\mathbf{B}$, $\mathbf{B}^{-1} = \mathbf{B}^{\dagger}/\det(\mathbf{B})$, where $\mathbf{B}^{\dagger}$ denotes the adjugate matrix of $\mathbf{B}$ [125]. Because $\mathbf{B}$ is a real upper triangular matrix, it only needs to compute the elements that are on the diagonal of $\mathbf{B}$. Therefore, the computation of $\mathbf{B}^{\dagger}$ and $\det(\mathbf{B})$ cost $\frac{K}{2}(K+1)^2$ and $K-1$ flops, respectively. According to (3.23) and (5.9), key operations and their computational complexities used in the above two algorithms are stated in Table 5.1.

Defining the computational complexity of operation 6 and 7 as $\mathcal{O}_l$ and $\mathcal{O}_o$, respectively, the optimum detection algorithm and the low-complexity detection algorithm computational complexities $\mathcal{O}_{Op}$ and $\mathcal{O}_{Lo}$ can be represented as

$$\mathcal{O}_{Op} = LM^{K_c}\mathcal{O}_o, \qquad \mathcal{O}_{Lo} = L\mathcal{O}_l + M^{K_c}\mathcal{O}_o. \tag{5.16}$$

It can be seen from (5.16) that the low-complexity detection algorithm has fewer iterations comparing with the optimum detection algorithm, thereby leading to the reduction of computational complexity.

Furthermore, assuming $\rho = 10$ and $\varkappa = 20$, the computational complexities of the low-complexity detection algorithm and optimum detection algorithm are shown in Fig. 5.6. The results indicate that the low-complexity detection algorithm can reduce the computational complexity for the generalised 3-D SSM system, and the effect is more obvious with the higher modulation order M. Meanwhile, compared to single RF-chain 3-D SSM systems, the low-complexity detection method has a more remarkable reduction in the computational complexity for multiple RF-chains generalised 3-D SSM systems.

5.4 The Asymptotic Performance and Diversity Gain

In this section, the asymptotic performance of the generalised 3-D SSM system is derived based on the analytical ABEP. Then the diversity gain and the coding gain of the system are also derived.

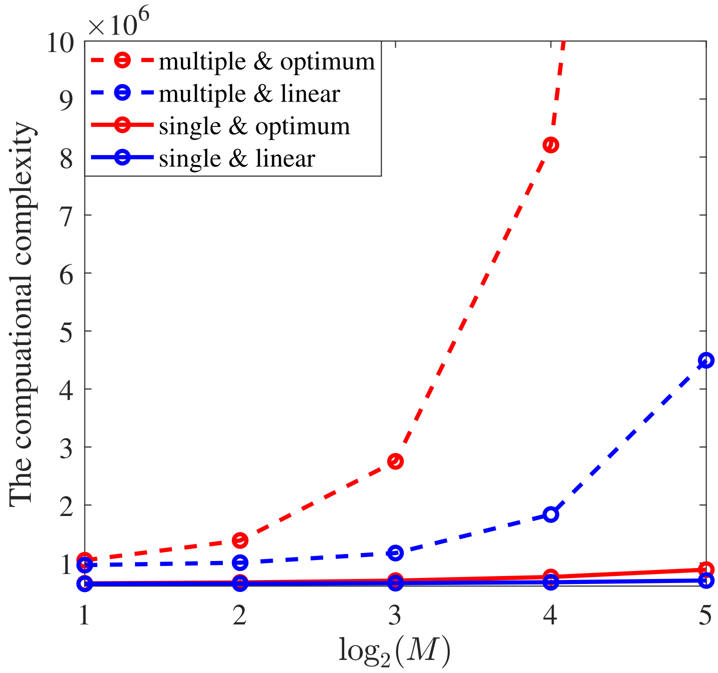

Fig. 5.6 The detection computational complexities for generalised 3-D SSM systems with 8×8 antenna arrays. The indoor environment described by Table 4.2 case 2 is adopted. $K = 5$ and $K_c = 2$ are applied for the multiple-RF-chain system. $K = 4$ and $K_c = 1$ are applied for the single-RF-chain system.

5.4.1 The Diversity Gain Analysis

Recalling the closed-form PEP expression shown in (4.17).

$$\mathrm{P}\left(l,\mathscr{M}\rightarrow\hat{l},\hat{\mathscr{M}}\right)\approx\frac{\prod_{n_s=1}^{N_{\mathrm{ts}}}\zeta'_{n_{\mathrm{s}}}}{12}+\frac{\prod_{n_s=1}^{N_{\mathrm{ts}}}\upsilon'_{n_{\mathrm{s}}}}{4},\tag{5.17}$$

Following the results in Lemma 3, the PEP expression can be rewritten as

$$\mathrm{P}\left(l,\mathscr{M}\rightarrow\hat{l},\hat{\mathscr{M}}\right)\approx\frac{\prod_{n_s=1}^{N_{\mathrm{ts}}}\left(1+\frac{\rho}{4N_{\mathrm{ts}}N_{\mathrm{t}}K_{\mathrm{c}}}\omega'_{n_{\mathrm{s}}}\right)^{-1}}{12}+\frac{\prod_{n_s=1}^{N_{\mathrm{ts}}}\left(1+\frac{\rho}{3N_{\mathrm{ts}}N_{\mathrm{t}}K_{\mathrm{c}}}\omega'_{n_{\mathrm{s}}}\right)^{-1}}{4}.\tag{5.18}$$

To derive the asymptotic expression of ABEP, the PEP expression needs to be simplified, the asymptotic expression of PEP can be represented as

$$\mathrm{P}\left(l,\mathscr{M}\rightarrow\hat{l},\hat{\mathscr{M}}\right)\approx\frac{\prod_{n_s=1}^{N_{\mathrm{ts}}}\left(\frac{\rho}{4N_{\mathrm{ts}}N_{\mathrm{t}}K_{\mathrm{c}}}\omega'_{n_{\mathrm{s}}}\right)^{-1}}{12}+\frac{\prod_{n_s=1}^{N_{\mathrm{ts}}}\left(\frac{\rho}{3N_{\mathrm{ts}}N_{\mathrm{t}}K_{\mathrm{c}}}\omega'_{n_{\mathrm{s}}}\right)^{-1}}{4}.\tag{5.19}$$

In the simplified PEP expression, the PEP under different SNR is determined by the channel gain and the number of scattering paths N_{ts}. Therefore, $\omega'_{n_{\mathrm{s}}}$ are sorted with descending order as $\bar{\omega}'_{\tilde{n}_{\mathrm{s}}}\in\{\bar{\omega}'_1,\bar{\omega}'_2,...,\bar{\omega}'_{N_{\mathrm{ts}}}\}$ following the steps in Lemma 3, where $\tilde{n}_{\mathrm{s}}$ is the index of $\bar{\omega}'_{\tilde{n}_{\mathrm{s}}}$. The selection of $\omega'_{n_{\mathrm{s}}}$ and N_{ts} will be described as follows. Based on (4.17), the asymptotic expression of PEP is

$$\begin{aligned}\mathrm{P}\left(l,\mathscr{M}\rightarrow\hat{l},\hat{\mathscr{M}}\right)&\approx\frac{\prod_{\tilde{n}_s=1}^{N_{\mathrm{g}}}\left(\frac{\rho}{4N_{\mathrm{g}}N_{\mathrm{t}}K_{\mathrm{c}}}\bar{\omega}'_{\tilde{n}_{\mathrm{s}}}\right)^{-1}}{12}+\frac{\prod_{\tilde{n}_s=1}^{N_{\mathrm{g}}}\left(\frac{\rho}{3N_{\mathrm{g}}N_{\mathrm{t}}K_{\mathrm{c}}}\bar{\omega}'_{\tilde{n}_{\mathrm{s}}}\right)^{-1}}{4}\\&=\rho^{-N_{\mathrm{g}}}\mathscr{G}\left(\bar{\omega}'_{\tilde{n}_{\mathrm{s}}},N_{\mathrm{g}},N_{\mathrm{t}},K_{\mathrm{c}}\right),\end{aligned}\tag{5.20}$$

and

$$\mathscr{G}\left(\bar{\omega}'_{\tilde{n}_{\mathrm{s}}},N_{\mathrm{g}},N_{\mathrm{t}},K_{\mathrm{c}}\right)=\left[\frac{\prod_{\tilde{n}_s=1}^{N_{\mathrm{g}}}\left(\frac{\bar{\omega}'_{\tilde{n}_{\mathrm{s}}}}{4N_{\mathrm{g}}N_{\mathrm{t}}K_{\mathrm{c}}}\right)^{-1}}{12}+\frac{\prod_{\tilde{n}_s=1}^{N_{\mathrm{g}}}\left(\frac{\bar{\omega}'_{\tilde{n}_{\mathrm{s}}}}{3N_{\mathrm{g}}N_{\mathrm{t}}K_{\mathrm{c}}}\right)^{-1}}{4}\right].\tag{5.21}$$

By substituting (5.20) into (4.16), an asymptotic $\mathrm{ABEP}_{\mathrm{asym}}$ can be expressed as

$$\mathrm{ABEP}_{\mathrm{asym}} \approx \rho^{-N_{\mathrm{g}}} \sum_{l=1}^{L} \sum_{\hat{l}=1}^{L} \sum_{\mathscr{M}=1}^{M^{K_{\mathrm{c}}}} \sum_{\hat{\mathscr{M}}=1}^{M^{K_{\mathrm{c}}}} \frac{1}{LM^{K_{\mathrm{C}}}} \frac{N(l,\mathscr{M} \to \hat{l},\hat{\mathscr{M}})}{\log_2(LM^{K_{\mathrm{C}}})} \mathscr{G}\left(\bar{\omega}'_{\tilde{n}_{\mathrm{s}}}, N_{\mathrm{g}}, N_{\mathrm{t}}, K_{\mathrm{c}}\right), \tag{5.22}$$

where $N_{\mathrm{g}} \in \{1,2,...,N_{\mathrm{ts}}\}$ dominates the slope of the $\mathrm{ABEP}_{\mathrm{asym}}$. For $\mathrm{ABEP}_{\mathrm{asym}}$, the SNR threshold corresponding to N_{g} selections can be calculated by

$$T_{\mathrm{SNR}}(N_{\mathrm{g}}) = \frac{\left(4N_{\mathrm{g}}N_{\mathrm{t}}K_{\mathrm{c}}\right)^{N_{\mathrm{g}}+1} + 3\left(3N_{\mathrm{g}}N_{\mathrm{t}}K_{\mathrm{c}}\right)^{N_{\mathrm{g}}+1}}{\bar{\omega}'_{N_{\mathrm{g}}}\left[\left(4(N_{\mathrm{g}}-1)N_{\mathrm{t}}K_{\mathrm{c}}\right)^{N_{\mathrm{g}}} + 3\left(3(N_{\mathrm{g}}-1)N_{\mathrm{t}}K_{\mathrm{c}}\right)^{N_{\mathrm{g}}}\right]}. \tag{5.23}$$

If $T_{\mathrm{SNR}}(N_{\mathrm{g}}) < \rho \leq T_{\mathrm{SNR}}(N_{\mathrm{g}}+1)$, N_{g} is selected to calculated the asymptotic performance in this region. Especially, when $-\infty < \rho \leq T_{\mathrm{SNR}}(1)$, $N_{\mathrm{g}} = 1$. According to (5.22), when the $\rho \to \infty$, $N_{\mathrm{g}} = N_{\mathrm{ts}}$. Therefore, the diversity gain $\mathscr{D}$ and coding gain $\mathscr{C}$ are given by

$$\mathscr{D} = N_{\mathrm{ts}}, \tag{5.24}$$

$$\mathscr{C} = \left[\sum_{\hat{l}=1}^{L} \sum_{\mathscr{M}=1}^{M^{K_{\mathrm{c}}}} \sum_{\hat{\mathscr{M}}=1}^{M^{K_{\mathrm{c}}}} \frac{1}{LM^{K_{\mathrm{C}}}} \frac{N(1,\mathscr{M} \to \hat{l},\hat{\mathscr{M}})}{\log_2(LM^{K_{\mathrm{C}}})} \mathscr{G}\left(\bar{\omega}'_{\tilde{n}_{\mathrm{s}}}, N_{\mathrm{g}}, N_{\mathrm{t}}, K_{\mathrm{c}}\right)\right]^{-\frac{1}{\mathscr{D}}}. \tag{5.25}$$

It should be noted that the asymptotic ABEP with $N_{\mathrm{g}} = N_{\mathrm{ts}}$ approaches the union upper bound slowly with an increasing SNR. As such, the asymptotic ABEP with $N_{\mathrm{g}} = N_{\mathrm{ts}}$ is not tight with a reasonable value of ρ. Therefore, N_{g} has to be selected according to (5.23).

5.4.2 The Asymptotic Performance and Discussions

Following (5.22), the asymptotic performance of generalised 3-D SSM system is shown as Fig. 5.7. 4×4, 6×6 and 10×10 three different sizes of antenna arrays are adopted for the transmitter and receiver. The M-PSK signal constellation is used for the baseband modulation. It can be seen from Fig. 5.7 that the asymptotic performance fits the numerical results well in different SNR regions with $N_{\mathrm{g}} = 2,3,4$, and the N_{g} is determined by (5.23). Taking the generalised SSM system with 6×6 antenna arrays as an example, when $T_{\mathrm{SNR}}(2) < \rho \leq T_{\mathrm{SNR}}(3)$, the green line is matched with the ABEP performance. When the $T_{\mathrm{SNR}}(3) <$

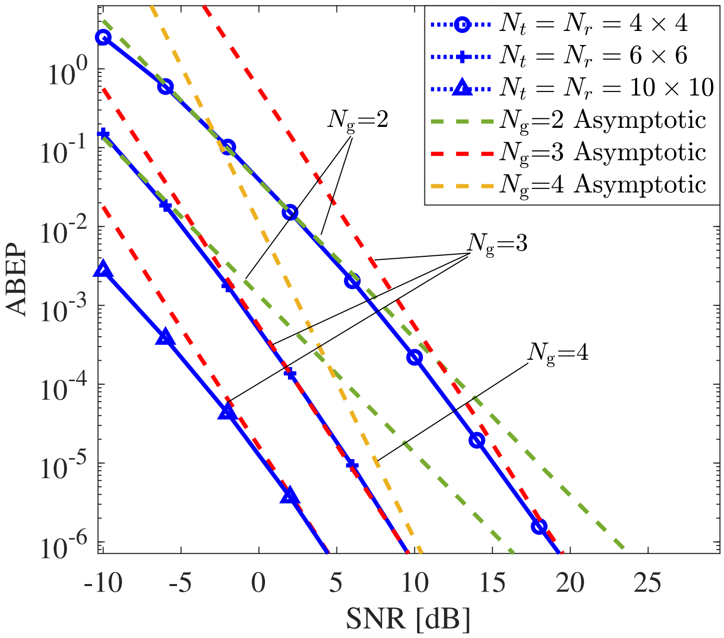

Fig. 5.7 The asymptotic performance of generalised 3-D SSM systems under the propagation environment described by Table 4.2 Case 2. The multiple RF-chains systems with $K = 5$, $K_c = 2$ and $M = 4$ is adopted.

$\rho \leq T_{\mathrm{SNR}}(4)$ and $T_{\mathrm{SNR}}(4) < \rho \leq T_{\mathrm{SNR}}(5)$, the red and yellow lines are be used to describe the asymptotic ABEP performance, respectively. Generally, the ABEP performance under different SNR region can be estimated accurately and quickly using the method provided in this section.

5.5 Conclusion

In this chapter, a hardware friendliness design has been introduced, which replaces the analogue phase shifter network with the multi-bit phase shifter network with limited quantification. The application of a multi-bit phase shifter network significantly simplifies the transceiver's circuit complexity. However, after applying the 2-D FFT algorithm, the AoAs/AoDs at the transceivers are not fully aligned with the scatterers' direction angles in the 3-D space, which leads to ABEP performance degradations. Furthermore, the low-complexity detection algorithm has been proposed, which significantly reduces the computational complexity, especially for the system adopting multiple RF-chains. Moreover, the asymptotic performance has been derived under different SNR regions. The results show that the asymptotic performance fits the numerical results well.

Chapter 6

Conclusions and Future Work

6.1 Conclusions

In this dissertation, a novel 3-D SSM system has been proposed for the mm-wave transmission to provide guidelines for the system deployment in reality. The 3-D SSM system has applied phase shifter networks to allocate the beam in the specified scattering path. Therefore, different scattering paths in 3-D space offer the multipath gain and set indices to carry extra information bits.

In the first-stage work as represented in Chapter 3, the 3-D SSM system with the large-scale planar array has been designed, which considers the azimuth and elevation angle of AoA and AoD in 3-D space. Due to the linear combination operated by the phase shifter network, the correlation noise is generated at the receiver, which leads to the additional received power. Besides, our system model also takes the mutual inference into account, which is generated side beams among RF-chains. Considering the correlation noise and mutual interference, we have designed the optimum detection algorithm for the 3-D SSM system. To obtain the analytical results, the closed-form expression of the union upper bound on the ABEP has been derived and verified via comparison with simulations. To evaluate the system performance, a typical indoor transmission environment has been investigated to obtain the channel impulse response by ray-tracing. According to the results, it is indicated that the 3-D SSM outperforms the 2-D SSM system, which is caused by the lack of DoF in the 2-D SSM system. Meanwhile, the results indicate that the larger size of the antenna array is a benefit to reduce the ABEP. Since SSM utilises scattering paths to convey information bit, the abundance of scattering paths in the transmission environment can also have an impact on the ABEP performance. As the results in Chapter 3, if the number of bits modulated in each time slot is constant, the more optional scattering paths in the transmission environment, the better the ABEP performance of the SSM system.

In the second-stage of this work, the generalised 3-D SSM with hybrid beamforming technology has been investigated. Specifically, the multiple RF-chains are generated in each time slot, and the conventional modulated symbols are transmitted by several RF-chains. Meanwhile, the generalised 3-D SSM system utilised the combinations of scattering paths to convey information bits. The system model and modulation scheme have been proposed at first. Then the optimum detector has been designed. To analyse the system performance, the PEP of SSM symbols has been obtained at first. Based on the PEP, the closed-form ABEP expression has been derived and validated by Monte-Carlo simulations. For the performance evaluation, we first utilised an indoor environment to analyse the ABEP performance. The results indicate that the generalised 3-D SSM system can significantly improve the system throughput, compared with the SSM system with a single RF-chain. However, the scatterers in the transmission environment are not always static, and the scattering path changes accordingly. Therefore, to evaluate the performance of the SSM system under the transmission environment with randomly distributed scatterers, we have defined three stochastic channel models. Compared with the typical indoor propagation environment, the ABEP performance is degraded with randomly distributed scatterers, because the scattering paths cannot be perfectly separated and distinguished by the receiver. In the practical network planning and modulation mode selection, the stochastic channel models can be applied to different application scenarios, which can predict the ABEP performance under various scatterer distribution models for the generalised 3-D SSM system. When channel conditions are unstable, i.e., the scatterers are randomly distributed, it is more reasonable to combine weak channels with the other one to transmit the same modulated symbol, which may be effective in reducing BER. However, the above method is not discussed in this thesis, which can be investigated in our future work.

In the third-stage of this work, several optimisation schemes for generalised 3-D SSM systems have been investigated in terms of hardware and software. Firstly, a hardware-friendly design for the generalised 3-D SSM system has been proposed. The analogue phase shifters at the transceivers are replaced by the multi-bit phase shifter with limited quantification, which utilises 2-D FFT algorithm for the beamforming process. Although the multi-bit phase shift sacrifices part of the ABEP performance, it can greatly reduce the hardware cost. With 8×8 antenna arrays, the system can achieve 10^{-5} ABEP, when the SNR reaches 18 dB. Secondly, the low-complexity detection algorithm has been designed to reduce the computational complexity of the generalised 3-D SSM system. Due to the global search in the optimum detection algorithm, the detection computational complexity exponentially increase with the number of generated RF-chains. Therefore, a MMSE based detection algorithm is proposed to reduce the computational complexity. The results show that when $K_\mathrm{c} = 2$, K=5 and M=4, the low-complexity algorithm can reduce the computational complexity by about 75%. Thirdly, the diversity gain and asymptotic performance of the generalised 3-D SSM system have been derived for the fast evaluation. With a specific SNR region, asymptotic results can quickly and accurately describe the system ABEP performance.

6.2 Future Work

- **(a) The adaptive modulation algorithm of the 3-D SSM system**

  In the conventional modulation system, adaptive modulation algorithms have been widely discussed. For SSM systems, the ABEP performance and throughput are effect by the selection of scattering path and the values of modulation order. Therefore, it is necessary to develop an adaptive modulation scheme that achieves a higher data rate and better ABEP performance for the 3-D SSM system. Accordingly, the optimal number of scattering paths and the optimal values of modulation order need to be considered jointly. For different scattering paths, a corresponding modulation order needs to be selected based on the CSI to pursue a better trade-off between the ABEP and SE.

- **(b) The scattering path optimisation scheme of the generalised 3-D SSM system**

  The CSI of scattering paths directly affect the ABEP performance of the 3-D SSM system. With several optional scattering paths, the CSI of scattering paths can be evaluated first, and then the path with better channel conditions is selected for data transmission. For the scattering paths with the lower channel gain, it can be combined with a robust channel to convey and transmit the same information bit. In this way, the negative impact of channel gains on the system error performance can be reduced.

- **(c) The measurement of generalised 3-D SSM system under different application scenarios**

  Most of the existing works on the SSM system are based on various ideal channel models, e.g., the i.i.d. Rayleigh channel. For the deployment, it is necessary to investigate the performance of SSM system in a realistic propagation environment. Since the SSM system performance is affected by the characteristics of scattering paths, the measurement results of scattering channel characteristics in different propagation environments, e.g., keyhole channels and vehicle channels, have important guiding significance for the system deployment.

- **(d) The generalised 3-D SSM system with imperfect CSI**

  For the 3-D SSM system, whether the scattering path can be resolved mainly depends on the AoA and AoD of beams, which requires the perfect CSI at the transceivers. Existing works of SSM assumed that the transceivers have the perfect CSI. However, in a real application, the perfect CSI is difficult to obtain. Therefore, with the imperfect CSI, a channel estimation approach needs to be designed. Meanwhile, the system performance with imperfect CSI should be reassessed.

- **(e) The combination of 3-D SSM and polarisation-space system**

The generalised polarisation-space modulation was proposed in [125], which utilises the polarisation indices of transmission antennas to convey information bits. For the 3-D SSM system with a large-scale antenna array, the dual-polarised transmission antenna can be applied, which utilises polarisation states and beam scattering paths to represent the modulated bits. The combination of the 3-D SSM and the polarisation-space modulation can further improve the SE with a limited number of RF-chains.

- **(f) The combination of 3-D SSM and OFDM-IM system**

  As a novel IM technology, the OFDM-IM system applies the indices of orthogonal subcarriers to convey extra information bits. For the SSM system with large-scale antenna arrays, it is suitable to be combined with OFDM-IM, which can further improve the SE. However, the combination of OFDM-IM and SSM will further increase the complexity of modulation schemes and detection algorithms. Predictably, the performance of the system will be affected by scattering path conditions, subcarrier characteristics, and modulation orders. In this case, whether the system can achieve a considerable ABEP performance under a reasonable SNR region is worth studying.

References

[1] J. Zhang, C. Pan, F. Pei, G. Liu, and X. Cheng, “Three-dimensional fading channel models: A survey of elevation angle research,” *IEEE Communications Magazine*, vol. 52, no. 6, pp. 218–226, Jun. 2014.

[2] “Cisco visual networking index: Forecast and trends, 2017–2022,” Cisco, USA, White Paper, May 2018.

[3] W. Roh, J. Seol *et al.*, “Millimeter-wave beamforming as an enabling technology for 5G cellular communications: theoretical feasibility and prototype results,” *IEEE Communications Magazine*, vol. 52, no. 2, pp. 106–113, Feb. 2014.

[4] J. G. Andrews, S. Buzzi, W. Choi, S. V. Hanly, A. Lozano, A. C. K. Soong, and J. C. Zhang, “What will 5G be?” *IEEE Journal on Selected Areas in Communications*, vol. 32, no. 6, pp. 1065–1082, Jun. 2014.

[5] L. Zheng and D. Tse, “Diversity and multiplexing: a fundamental tradeoff in multiple-antenna channels,” *IEEE Transactions on Information Theory*, vol. 49, no. 5, pp. 1073–1096, May 2003.

[6] X. Cheng, B. Yu, L. Yang, J. Zhang, G. Liu, Y. Wu, and L. Wan, “Communicating in the real world: 3D MIMO,” *IEEE Wireless Communications*, vol. 21, no. 4, pp. 136–144, Aug. 2014.

[7] Y. Zhang, L. Pang, G. Ren, F. Gong, X. Liang, J. Dou, and J. Li, “3-D MIMO parametric stochastic channel model for urban macrocell scenario,” *IEEE Transactions on Wireless Communications*, vol. 16, no. 7, pp. 4246–4260, Sep. 2017.

[8] G. Liu, X. Hou, J. Jin, F. Wang, Q. Wang, Y. Hao, Y. Huang, X. Wang, X. Xiao, and A. Deng, “3-D MIMO with massive antennas paves the way to 5G enhanced mobile broadband: From system design to field trials,” *IEEE Journal on Selected Areas in Communications*, vol. 35, no. 6, pp. 1222–1233, Dec. 2017.

[9] Y. Liu, Y. Shen, Z. Lyu, Y. Liang, W. He, Y. Gao, H. Yang, and L. Yu, “Real-time 3-D MIMO antenna tuning with deep reinforcement learning,” *IEEE Transactions on Cognitive Communications and Networking*, vol. 8, no. 2, pp. 1202–1215, Jul. 2022.

[10] Q. Zhu, Y. Yang, C.-X. Wang, Y. Tan, J. Sun, X. Chen, and W. Zhong, “Spatial correlations of a 3-D non-stationary mimo channel model with 3-D antenna arrays and 3-D arbitrary trajectories,” *IEEE Wireless Communications Letters*, vol. 8, no. 2, pp. 512–515, Apr. 2019.

[11] X. Pu, S. Shao, K. Deng, and Y. Tang, “Analysis of the capacity statistics for 2×2 3D MIMO channels in short-range communications,” *IEEE Communications Letters*, vol. 19, no. 2, pp. 219–222, Feb. 2015.

[12] 3GPP, “5G new radio (NR) release 16 standard,” 3rd Generation Partnership Project (3GPP), Technical Specification 21.916, Jul. 2020, version 16.2.0.

[13] E. Aydın and H. Ilhan, “A novel SM-based MIMO system with index modulation,” *IEEE Communications Letters*, vol. 20, no. 2, pp. 244–247, Aug. 2016.

[14] R. Y. Mesleh, H. Haas, S. Sinanovic, C. W. Ahn, and S. Yun, “Spatial modulation,” *IEEE Transactions on Vehicular Technology*, vol. 57, no. 4, pp. 2228–2241, JuL. 2008.

[15] T. Mao, Q. Wang, Z. Wang, and S. Chen, “Novel index modulation techniques: A survey,” *IEEE Communications Surveys and Tutorials*, vol. 21, no. 1, pp. 315–348, Firstquarter 2019.

[16] Y. Ding, K. J. Kim, T. Koike-Akino, M. Pajovic, P. Wang, and P. Orlik, “Spatial scattering modulation for uplink millimeter-wave systems,” *IEEE Communications Letters*, vol. 21, no. 7, pp. 1493–1496, 2017.

[17] G. Foschini and M. Gans, “On limits of wireless communications in a fading environment when using multiple antennas,” *Wireless Personal Communications*, vol. 6, pp. 311–335, Mar. 1998.

[18] T. L. Marzetta, “Noncooperative cellular wireless with unlimited numbers of base station antennas,” *IEEE Transactions on Wireless Communications*, vol. 9, no. 11, pp. 3590–3600, Nov. 2010.

[19] L. Liu, R. Chen, S. Geirhofer, K. Sayana, Z. Shi, and Y. Zhou, “Downlink MIMO in LTE-advanced: SU-MIMO vs. MU-MIMO,” *IEEE Communications Magazine*, vol. 50, no. 2, pp. 140–147, Aug. 2012.

[20] V. Kristem, S. Sangodoyin, C. U. Bas, M. Käske, J. Lee, C. Schneider, G. Sommerkorn, C. J. Zhang, R. S. Thomä, and A. F. Molisch, “3D MIMO outdoor-to-indoor propagation channel measurement,” *IEEE Transactions on Wireless Communications*, Jul. 2017.

[21] Q. Luo, F. Pei, J. Zhang, and M. Zhang, “3D MIMO channel model based on field measurement campaign for UMa scenario,” in *2014 IEEE Wireless Communications and Networking Conference (WCNC)*, Aug. 2014, pp. 171–176.

[22] J. Zhang, Y. Zhang, Y. Yu, R. Xu, Q. Zheng, and P. Zhang, “3-D MIMO: How much does it meet our expectations observed from channel measurements?” *IEEE Journal on Selected Areas in Communications*, vol. 35, no. 8, pp. 1887–1903, Aug. 2017.

[23] J. Zhou, H. Jiang, and H. Kikuchi, “Generalized 3D scattering channel model with MIMO antenna systems,” *China Communications*, vol. 13, no. 5, pp. 66–81, May. 2016.

[24] R. Dong, W. Hardjawana, A. Li, Y. Li, and B. Vucetic, “Cooperative beamforming for multi-cell full dimensional massive MIMO networks,” in *IEEE International Conference on Communications (ICC)*, Oct. 2019, pp. 1–6.

[25] S. Rangan and R. Madan, "Belief propagation methods for intercell interference coordination in femtocell networks," *IEEE Journal on Selected Areas in Communications*, vol. 30, no. 3, pp. 631–640, Apr. 2012.

[26] R. Dong, W. Hardjawana, Y. Li, and B. Vucetic, "Dynamic sectoring with elevation optimization technique in 5G cellular networks," in *IEEE International Conference on Communications Workshops (ICC Workshops)*, Jul. 2018, pp. 1–5.

[27] S. Hu, C. Xu, X. Wang, Y. Huang, and S. Zhang, "A stochastic ADMM approach to distributed coordinated multicell beamforming for renewables powered wireless cellular networks," *IEEE Transactions on Vehicular Technology*, vol. 67, no. 9, pp. 8595–8607, Sep. 2018.

[28] X. Li, S. Jin, X. Gao, and R. W. Heath, "Three-dimensional beamforming for large-scale FD-MIMO systems exploiting statistical channel state information," *IEEE Transactions on Vehicular Technology*, vol. 65, no. 11, pp. 8992–9005, Nov. 2016.

[29] X. Li, C. Li, S. Jin, and X. Gao, "Interference coordination for 3-D beamforming-based hetnet exploiting statistical channel-state information," *IEEE Transactions on Wireless Communications*, vol. 17, no. 10, pp. 6887–6900, Oct. 2018.

[30] X. Li, Z. Liu, N. Qin, and S. Jin, "FFR based joint 3D beamforming interference coordination for multi-cell FD-MIMO downlink transmission systems," *IEEE Transactions on Vehicular Technology*, vol. 69, no. 3, pp. 3105–3118, Mar. 2020.

[31] W. Lee, S.-R. Lee, H.-B. Kong, and I. Lee, "3D beamforming designs for single user MISO systems," in *IEEE Global Communications Conference (GLOBECOM)*, Sep. 2013, pp. 3914–3919.

[32] Z. Zhang, K. C. Teh, and K. H. Li, "Study of three-dimensional beamforming strategies in cellular networks with clustered user distribution," *IEEE Transactions on Vehicular Technology*, vol. 65, no. 12, pp. 10 208–10 213, Dec. 2016.

[33] Y. Chau and S.-H. Yu, “Space modulation on wireless fading channels,” in *IEEE 54th Vehicular Technology Conference. VTC Fall 2001. Proceedings*, vol. 3, 2001, pp. 1668–1671 vol.3.

[34] J. Jeganathan, A. Ghrayeb, and L. Szczecinski, “Generalized space shift keying modulation for MIMO channels,” in *IEEE 19th International Symposium on Personal, Indoor and Mobile Radio Communications*, Jun. 2008, pp. 1–5.

[35] R. Mesleh, O. S. Badarneh, A. Younis, and H. Haas, “Performance analysis of spatial modulation and space-shift keying with imperfect channel estimation over generalized fading channels,” *IEEE Transactions on Vehicular Technology*, vol. 64, no. 1, pp. 88–96, Jan. 2015.

[36] J. Wang, S. Jia, and J. Song, “Generalised spatial modulation system with multiple active transmit antennas and low complexity detection scheme,” *IEEE Transactions on Wireless Communications*, vol. 11, no. 4, pp. 1605–1615, Apr. 2012.

[37] E. Başar, U. Aygölü, E. Panayirci, and H. V. Poor, “Space-time block coded spatial modulation,” *IEEE Transactions on Communications*, Mar. 2011.

[38] H. Haas, E. Costa, and E. Schulz, “Increasing spectral efficiency by data multiplexing using antenna arrays,” in *The 13th IEEE International Symposium on Personal, Indoor and Mobile Radio Communications*, vol. 2, 2002, pp. 610–613 vol.2.

[39] J. Jeganathan, A. Ghrayeb, L. Szczecinski, and A. Ceron, “Space shift keying modulation for MIMO channels,” *IEEE Transactions on Wireless Communications*, vol. 8, no. 7, pp. 3692–3703, Jul. 2009.

[40] J. Fu, C. Hou, W. Xiang, L. Yan, and Y. Hou, “Generalised spatial modulation with multiple active transmit antennas,” in *IEEE Globecom Workshops*, 2010, pp. 839–844.

[41] A. Younis, N. Serafimovski, R. Mesleh, and H. Haas, “Generalised spatial modulation,” in *Conference Record of the Forty Fourth Asilomar Conference on Signals, Systems and Computers*, 2010, pp. 1498–1502.

[42] J. Jeganathan, A. Ghrayeb, and L. Szczecinski, “Spatial modulation: optimal detection and performance analysis,” *IEEE Communications Letters*, vol. 12, no. 8, pp. 545–547, Aug. 2008.

[43] S. U. Hwang, S. Jeon, S. Lee, and J. Seo, “Soft-output ml detector for spatial modulation OFDM systems,” *IEICE Electronics Express*, vol. 6, no. 19, pp. 1426–1431, Jul. 2009.

[44] S. Chen, S. Sugiura, and L. Hanzo, “Semi-blind joint channel estimation and data detection for space-time shift keying systems,” *IEEE Signal Processing Letters*, vol. 17, no. 12, pp. 993–996, Dec. 2010.

[45] B. Tarika and X. Hongjun, “Low-complexity EDAS and low-complexity detection scheme for MPSK spatial modulation,” *IET Communications*, vol. 10, no. 14, pp. 1752–1757, Sep. 2016.

[46] J. Zheng, X. Yang, and Z. Li, “Low-complexity detection method for spatial modulation based on M-algorithm,” *Electronics Letters*, vol. 50, no. 21, pp. 1552–1554, Oct. 2014.

[47] Z. Yigit and E. Basar, “Low-complexity detection of quadrature spatial modulation,” *Electronics Letters*, vol. 52, no. 20, pp. 1729–1731, Sep. 2016.

[48] G. Mingxi, J. Chong, and S. Yuehong, “Detection algorithm for spatial modulation system under unconstrained channel,” in *IEEE 12th International Conference on Communication Technology*, 2010, pp. 458–461.

[49] S. Sugiura, C. Xu, S. X. Ng, and L. Hanzo, “Reduced-complexity coherent versus non-coherent QAM-aided space-time shift keying,” *IEEE Transactions on Communications*, vol. 59, no. 11, pp. 3090–3101, Nov. 2011.

[50] C. Xu, S. Sugiura, S. X. Ng, and L. Hanzo, “Spatial modulation and space-time shift keying: Optimal performance at a reduced detection complexity,” *IEEE Transactions on Communications*, vol. 61, no. 1, pp. 206–216, Jan. 2013.

[51] Q. Tang, Y. Xiao, P. Yang, Q. Yu, and S. Li, “A new low-complexity near-ml detection algorithm for spatial modulation,” *IEEE Wireless Communications Letters*, vol. 2, no. 1, pp. 90–93, Feb. 2013.

[52] P. Yang, M. Di Renzo, Y. Xiao, S. Li, and L. Hanzo, “Design guidelines for spatial modulation,” *IEEE Communications Surveys Tutorials*, vol. 17, no. 1, pp. 6–26, Firstquarter 2015.

[53] A. Younis, R. Mesleh, H. Haas, and P. M. Grant, “Reduced complexity sphere decoder for spatial modulation detection receivers,” in *IEEE Global Telecommunications Conference GLOBECOM*, Sep. 2010, pp. 1–5.

[54] A. Younis, S. Sinanovic, M. Di Renzo, R. Mesleh, and H. Haas, “Generalised sphere decoding for spatial modulation,” *IEEE Transactions on Communications*, vol. 61, no. 7, pp. 2805–2815, 2013.

[55] M. Wen, Q. Li *et al.*, “Generalized multiple-mode OFDM with index modulation,” *IEEE Transactions on Wireless Communications*, vol. 17, no. 10, pp. 6531–6543, Oct. 2018.

[56] E. Basar, M. Wen *et al.*, “Index modulation techniques for next-generation wireless networks,” *IEEE Access*, vol. 5, pp. 16 693–16 746, Mar. 2017.

[57] E. Basar, H. V. Poor *et al.*, “Orthogonal frequency division multiplexing with index modulation,” *IEEE Trans. Signal Process.*, vol. 61, no. 22, pp. 5536–5549, Nov. 2013.

[58] J. Li, S. Dang *et al.*, “Layered orthogonal frequency division multiplexing with index modulation,” *IEEE Systems Journal*, vol. 13, no. 4, pp. 3793–3802, Dec. 2019.

[59] T. Mao, Q. Wang, J. Quan, and Z. Wang, “Zero-padded tri-mode index modulation aided OFDM,” in *IEEE Global Communications Conference (GLOBECOM)*, 2017, pp. 1–5.

[60] R. Fan, Y. J. Yu, and Y. L. Guan, “Generalization of orthogonal frequency division multiplexing with index modulation,” *IEEE Transactions on Wireless Communications*, vol. 14, no. 10, pp. 5350–5359, Oct. 2015.

[61] T. Mao, Z. Wang, Q. Wang, S. Chen, and L. Hanzo, “Dual-mode index modulation aided OFDM,” *IEEE Access*, vol. 5, pp. 50–60, 2017.

[62] T. Mao, Q. Wang, and Z. Wang, “Generalized dual-mode index modulation aided OFDM,” *IEEE Communications Letters*, Apr. 2017.

[63] E. Başar, “Multiple-input multiple-output OFDM with index modulation,” *IEEE Signal Processing Letters*, vol. 22, no. 12, pp. 2259–2263, Dec. 2015.

[64] E. Basar, “On multiple-input multiple-output OFDM with index modulation for next generation wireless networks,” *IEEE Transactions on Signal Processing*, Aug. 2016.

[65] S. Sugiura, T. Ishihara, and M. Nakao, “State-of-the-art design of index modulation in the space, time, and frequency domains: Benefits and fundamental limitations,” *IEEE Access*, vol. 5, pp. 21 774–21 790, 2017.

[66] M. Nakao, T. Ishihara, and S. Sugiura, “Single-carrier frequency-domain equalization with index modulation,” *IEEE Communications Letters*, vol. 21, no. 2, pp. 298–301, Feb. 2017.

[67] M. Nakao and S. Sugiura, “Dual-mode time-domain single-carrier index modulation with frequency-domain equalization,” in *IEEE 86th Vehicular Technology Conference (VTC-Fall)*, 2017, pp. 1–5.

[68] S. Jacob, T. L. Narasimhan, and A. Chockalingam, “Space-time index modulation,” in *IEEE Wireless Communications and Networking Conference (WCNC)*, 2017, pp. 1–6.

[69] S. Sugiura, S. Chen, and L. Hanzo, “Coherent and differential space-time shift keying: A dispersion matrix approach,” *IEEE Transactions on Communications*, vol. 58, no. 11, pp. 3219–3230, Nov. 2010.

[70] S. Sugiura, S. Chen, and L. Hanzo, “Generalized space-time shift keying designed for flexible diversity-, multiplexing- and complexity-tradeoffs,” *IEEE Transactions on Wireless Communications*, vol. 10, no. 4, pp. 1144–1153, Apr. 2011.

[71] B. Shamasundar, S. Bhat, S. Jacob, and A. Chockalingam, “Multidimensional index modulation in wireless communications,” *IEEE Access*, vol. 6, pp. 589–604, 2018.

[72] F. John B. Anderson, Rusek and V. Öwall, “Faster-than-nyquist signaling,” *Proceedings of the IEEE*, vol. 101, no. 8, pp. 1817–1830, Aug. 2013.

[73] T. Ishihara and S. Sugiura, “Faster-than-nyquist signaling with index modulation,” *IEEE Wireless Communications Letters*, vol. 6, no. 5, pp. 630–633, Oct. 2017.

[74] S. Ruan, B. Hu *et al.*, “Diversity analysis for spatial scattering modulation in millimeter wave MIMO system,” in *Proc. 11th International Conference on Wireless Communications and Signal Processing*, Oct. 2019, pp. 1–5.

[75] Q. Li, K. J. Kim *et al.*, “Polarized spatial scattering modulation,” *IEEE Communication Letter*, vol. 23, no. 12, pp. 2252–2256, Dec. 2019.

[76] X. Zhu, L. Yuan, K. J. Kim, Q. Li, and J. Zhang, “Reconfigurable intelligent surface-assisted spatial scattering modulation,” *IEEE Communications Letters*, Dec. 2022.

[77] O. E. Ayach, S. Rajagopal, S. Abu-Surra, Z. Pi, and R. W. Heath, “Spatially sparse precoding in millimeter wave MIMO systems,” *IEEE Transactions on Wireless Communications*, vol. 13, no. 3, pp. 1499–1513, Mar. 2014.

[78] T. Handte, A. Muller, and J. Speidel, “BER analysis and optimization of generalized spatial modulation in correlated fading channels,” in *IEEE 70th Vehicular Technology Conference Fall*, 2009, pp. 1–5.

[79] M. M. U. Faiz, S. Al-Ghadhban, and A. Zerguine, “Recursive least-squares adaptive channel estimation for spatial modulation systems,” in *IEEE 9th Malaysia International Conference on Communications (MICC)*, 2009, pp. 785–788.

[80] A. B. Saleem and S. A. Hassan, “On the performance of spatial modulation schemes in large-scale MIMO under correlated nakagami fading,” in *IEEE 91st Vehicular Technology Conference (VTC2020-Spring)*, Aug. 2020, pp. 1–5.

[81] Y. Yang and B. Jiao, “Information-guided channel-hopping for high data rate wireless communication,” *IEEE Communications Letters*, vol. 12, no. 4, pp. 225–227, Apr. 2008.

[82] S. X. Ng and L. Hanzo, “On the MIMO channel capacity of multidimensional signal sets,” *IEEE Transactions on Vehicular Technology*, vol. 55, no. 2, pp. 528–536, Mar. 2006.

[83] Y. Yang, “Spatial modulation exploited in non-reciprocal two-way relay channels: Efficient protocols and capacity analysis,” *IEEE Transactions on Communications*, vol. 64, no. 7, pp. 2821–2834, Jul. 2016.

[84] S. Sugiura, S. Chen, and L. Hanzo, “MIMO-aided near-capacity turbo transceivers: Taxonomy and performance versus complexity,” *IEEE Communications Surveys and Tutorials*, vol. 14, no. 2, pp. 421–442, Secondquarter 2012.

[85] X. Guan, Y. Cai, and W. Yang, “On the mutual information and precoding for spatial modulation with finite alphabet,” *IEEE Wireless Communications Letters*, vol. 2, no. 4, pp. 383–386, Aug. 2013.

[86] S. Wang, Y. Li, M. Zhao, and J. Wang, “Energy-efficient and low-complexity uplink transceiver for massive spatial modulation MIMO,” *IEEE Transactions on Vehicular Technology*, vol. 64, no. 10, pp. 4617–4632, Oct. 2015.

[87] S. Wang, Y. Li, J. Wang, and M. Zhao, “Low-complexity multiuser detection in massive spatial modulation MIMO,” in *IEEE Globecom Workshops (GC Wkshps)*, 2014, pp. 784–789.

[88] M. Di Renzo and H. Haas, “Bit error probability of SM-MIMO over generalized fading channels,” *IEEE Transactions on Vehicular Technology*, vol. 61, no. 3, pp. 1124–1144, Mar. 2012.

[89] P. Yang, Y. Xiao, Y. Yu, and S. Li, “Adaptive spatial modulation for wireless MIMO transmission systems,” *IEEE Communications Letters*, vol. 15, no. 6, pp. 602–604, Jun. 2011.

[90] C. Cheng, H. Sari *et al.*, “Enhanced spatial modulation with multiple signal constellations,” *IEEE Transactions on Communications*, vol. 63, no. 6, pp. 2237–2248, Jun. 2015.

[91] C.-C. Cheng, H. Sari, S. Sezginer, and Y. T. Su, “New signal designs for enhanced spatial modulation,” *IEEE Transactions on Wireless Communications*, vol. 15, no. 11, pp. 7766–7777, Nov. 2016.

[92] R. Mesleh, S. S. Ikki, and H. M. Aggoune, “Quadrature spatial modulation,” *IEEE Transactions on Vehicular Technology*, vol. 64, no. 6, pp. 2738–2742, Jun. 2015.

[93] A. M. Abu-Hudrouss, A. H. Al Habbash, and S. Aïssa, “Signed quadrature spatial modulation for MIMO systems,” *IEEE Transactions on Vehicular Technology*, vol. 69, no. 3, pp. 2740–2746, Oct. 2020.

[94] R. Mesleh, S. S. Ikki, and F. S. Almehmadi, “Impact of IQ imbalance on the performance of QSM multiple-input–multiple-output system,” *IET Communications*, vol. 10, no. 17, pp. 2391–2395, 2016.

[95] M. D. Renzo and H. Haas, “Improving the performance of space shift keying (SSK) modulation via opportunistic power allocation,” *IEEE Communications Letters*, vol. 14, no. 6, pp. 500–502, Jun. 2010.

[96] ——, “Space shift keying (SSK—) MIMO over correlated rician fading channels: Performance analysis and a new method for transmit-diversity,” *IEEE Transactions on Communications*, Jan. 2011.

[97] M. Di Renzo and H. Haas, “Bit error probability of space-shift keying MIMO over multiple-access independent fading channels,” *IEEE Transactions on Vehicular Technology*, vol. 60, no. 8, pp. 3694–3711, Oct. 2011.

[98] R. Fan, Y. J. Yu, and Y. L. Guan, “Orthogonal frequency division multiplexing with generalized index modulation,” in *IEEE Global Communications Conference*, 2014, pp. 3880–3885.

[99] S. Gao, X. Cheng, and L. Yang, “Spatial multiplexing with limited RF chains: Generalized beamspace modulation (GBM) for mmwave massive MIMO,” *IEEE J. Sel. Areas Commun.*, vol. 37, no. 9, pp. 2029–2039, Sep. 2019.

[100] X. Yu, J. Shen *et al.*, “Alternating minimization algorithms for hybrid precoding in millimeter wave MIMO systems,” *IEEE Journal on Selected Topics in Signal Processing*, vol. 10, no. 3, pp. 485–500, Apr. 2016.

[101] S. Guo, H. Zhang *et al.*, “Generalized beamspace modulation using multiplexing: A breakthrough in mmwave MIMO,” *IEEE Journal on Selected Areas in Communications*, vol. 37, no. 9, pp. 2014–2028, Sep. 2019.

[102] P. Yang, Y. Xiao *et al.*, “Multidomain index modulation for vehicular and railway communications: a survey of novel techniques,” *IEEE Veh. Technol. Mag.*, Sep. 2018.

[103] A. Goldsmith, *Wireless Communications.* Cambridge, UK: Cambridge University Press, 2005.

[104] Y. Ding, V. Fusco *et al.*, “Beam index modulation wireless communication with analog beamforming,” *IEEE Transactions on Vehicular Technology*, vol. 67, no. 7, pp. 6340–6354, Jul. 2018.

[105] M. K. Simon and M. Alouini, *Digital Communication Over Fading Channels.* Hoboken, NJ, USA: Wiley, 2005.

[106] J. Lu, K. B. Letaief *et al.*, “M-PSK and M-QAM BER computation using signal-space concepts,” *IEEE Transactions on Communications*, vol. 47, no. 2, pp. 181–184, Feb. 1999.

[107] M. Chiani, D. Dardari, and M. K. Simon, “New exponential bounds and approximations for the computation of error probability in fading channels,” *IEEE Transactions on Wireless Communications*, vol. 2, no. 4, pp. 840–845, Jul. 2003.

[108] C. Gustafson, K. Haneda *et al.*, “On mm-wave multipath clustering and channel modeling,” *IEEE Transactions on Antennas and Propagation*, vol. 62, no. 3, pp. 1445–1455, Mar. 2014.

[109] O. Stabler and R. Hoppe, “MIMO channel capacity computed with 3D ray tracing model,” in *Proc. 3rd European Conference on Antennas and Propagation*, Mar. 2009, pp. 2271–2275.

[110] K.-C. Ho and S.-H. Tsai, “A novel multiuser beamforming system with reduced complexity and beam optimizations,” *IEEE Transactions on Wireless Communications*, vol. 18, no. 9, pp. 4544–4557, Sep. 2019.

[111] S. A. Busari, K. M. S. Huq, S. Mumtaz, L. Dai, and J. Rodriguez, “Millimeter-wave massive MIMO communication for future wireless systems: A survey,” *IEEE Communications Surveys and Tutorials*, vol. 20, no. 2, pp. 836–869, Secondquarter 2018.

[112] G. Marsaglia, “Choosing a point from the surface of a sphere,” *The Annals of Mathematical Statistics*, vol. 43, no. 2, pp. 645–646, 1972.

[113] A. Alayón Glazunov and P. H. Lehne, “A spherical probability distribution model of the user-induced mobile phone orientation,” *IEEE Access*, vol. 6, pp. 37 185–37 194, Jun. 2018.

[114] L. Liu and O. Claude, “The COST 2100 mimo channel model,” *IEEE Communication Magazine*, Dec. 2012.

[115] S. Suvrit, “A short note on parameter approximation for von Mises-Fisher distributions: and a fast implementation of I s(x),” *Comput. Stat. Data Anal.*, vol. 27, no. 1, pp. 177–190, Mar. 2012.

[116] M. Romanazzi, “Discriminant analysis with high dimensional von Mises-Fisher distributions,” in *Proc. 8th Annual International Conference on Statistics*, Sep. 2014, pp. 1–16.

[117] M. Zhu and S. Gunnarsson, “COST 2100 channel model, implementation available in the public domain,” Oct. 2018, [Online] Available: https://github.com/cost2100.

[118] P. Juho and H. Katsuyuki, “Parameterization of the COST 2100 MIMO channel model in indoor scenarios,” in *Proc. 5th Eur. Conf. Antennas Propag. (EUCAP)*, Sep. 2011, pp. 3606–3610.

[119] F. Jose, X. Li *et al.*, “Massive MIMO extensions to the COST 2100 channel model: Modeling and validation,” *IEEE Transactions on Wireless Communications*, vol. 19, no. 1, pp. 380–394, Jan. 2020.

[120] M. Zhu, E. Gunnar *et al.*, “The COST 2100 channel model: Parameterization and validation based on outdoor MIMO measurements at 300 mhz,” *IEEE Transactions on Wireless Communications*, vol. 12, no. 2, pp. 888–897, Feb. 2013.

[121] Yu Liu, A. Borgioli *et al.*, “K-band 3-bit low-loss distributed mems phase shifter,” *IEEE Microwave and Wireless Components Letters*, vol. 10, no. 10, pp. 415–417, Oct. 2000.

[122] J. Zhang, A. A. Glazunov, J. Yang, X. Chu, and J. Zhang, “An experimental study on indoor massive 3D-MIMO channel at 30-40 ghz band,” in *Proc. International Symposium on Antennas and Propagation (ISAP)*, 2018, pp. 1–2.

[123] J. Eilert, Di Wu, and Dake Liu, “Implementation of a programmable linear MMSE detector for MIMO-OFDM,” in *IEEE International Conference on Acoustics, Speech and Signal Processing*, Jan. 2008, pp. 5396–5399.

[124] H. Sampath, P. Stoica, and A. Paulraj, “Generalized linear precoder and decoder design for MIMO channels using the weighted MMSE criterion,” *IEEE Transactions on Communications*, vol. 49, no. 12, pp. 2198–2206, Dec. 2001.

[125] J. Zhang, K. J. Kim, Y. Wang, L. Ding, and J. Zhang, “Generalized polarization-space modulation,” *IEEE Transactions on Communications*, vol. 68, no. 10, pp. 258–273, Jan. 2020.